Chapter 4

Copper(II) hydrazone complexes with different nuclearties and geometries: Synthesis, structures, spectral properties, electrochemical behaviour, density functional study and *in vitro* catalytic activity

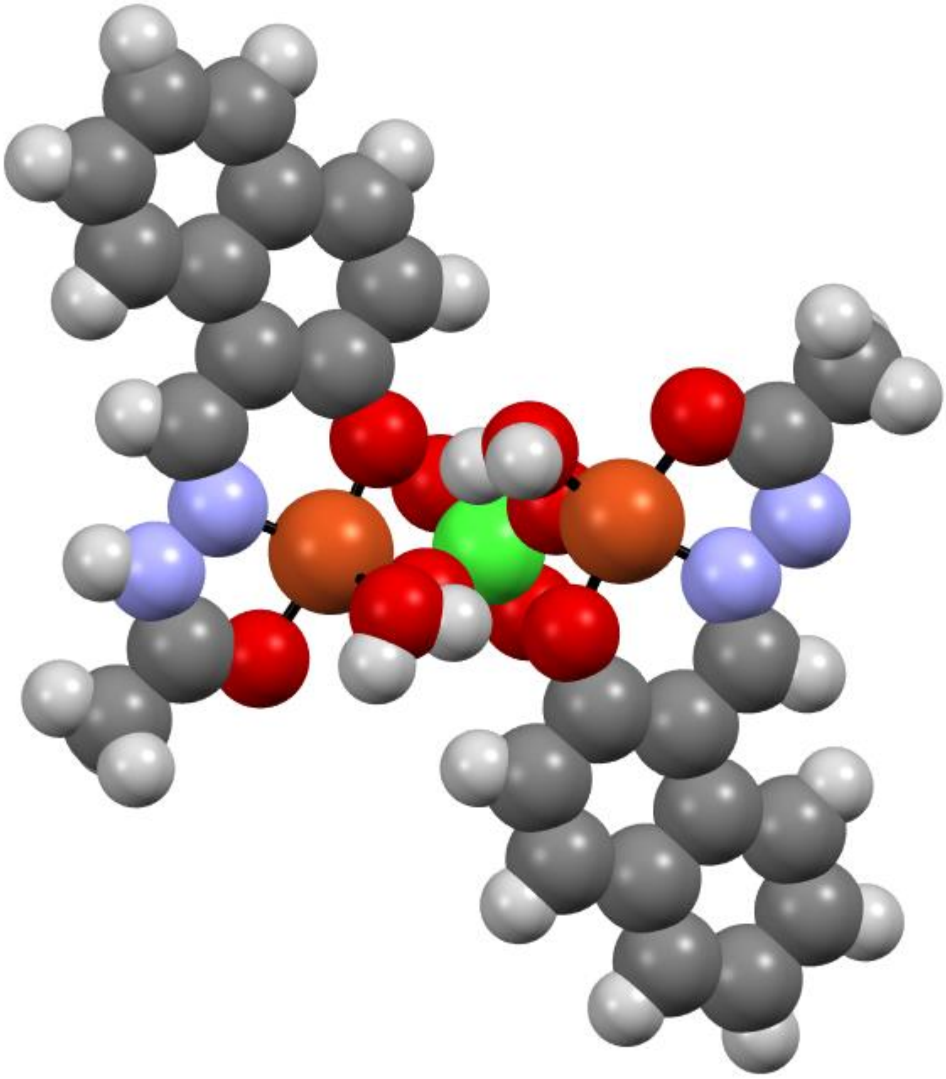

1. Introduction

Hydrazones are compounds of >CNN< group and are frequently achieved by the reaction of hydrazine and carbonyl compounds (aldehyde or ketones). Hydrazones also provide an excellent polydentate chelating ligand efficient of forming a coordination complex with a diversity of both transition and inner-transition metal ions. The chemistry of hydrazones and their metal complexes is uninterrupted to be a fascinating area of research. Hydrazones and their metal complexes show possible applications as catalysts [1, 2] molecular sensors [3], luminescent probes [4] and also as therapeutic compounds [5]. Also, transition metal hydrazone complexes have been the subject matter for many years due to their antimicrobial and antitumor activities [6-10]. Hydrazones Schiff bases also draw ongoing attention due to their structural diversity and coordination behaviour. Such ligands having ONO donor atoms can coordinate to one or more metal centres [11-14]. From the structural point of view, the selection of Schiff bases formed by the reaction between aldehyde group of napthaldehyde and acetyl hydrazide is a great selection to synthesize coordination complexes. The mode of binding of hydrazone ligands with transition metal may begin according to one of the following paths. Path (i) leads to the formation of complexes in which the hydrazone reacts with transition metal in the ketonic form (Scheme 1(i)) whereas the second one hydrazone reacts in an enolic form (Scheme 1(ii)), leading to the formation of two types of complexes. The mode of binding of hydrazones and geometry of complexes depends on the metal ion, anion of salt and alkalinity of the reaction medium [15].

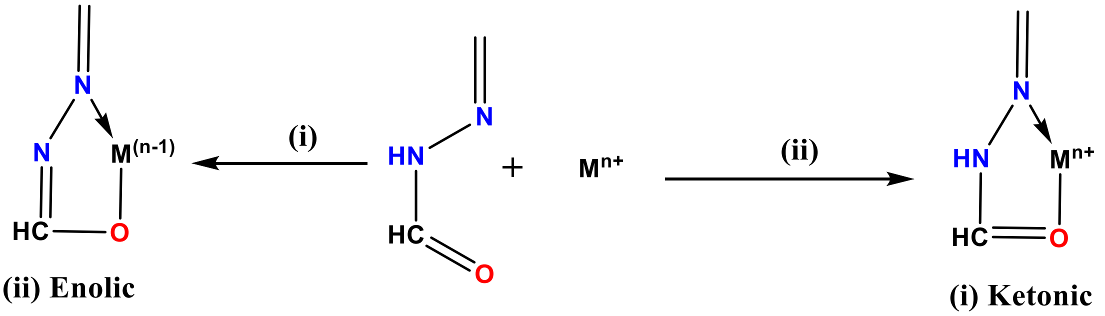

Scheme 1 Mode of binding of hydrazone.

Hydrazones-based copper(II) complexes can be revealed for their structural diversity as well as for their applications to examine the effect of structural and chemical factors that regulate the exchange coupling between paramagnetic centres [16-22]. Metal complexes with hydrazone Schiff bases from various structural motifs based on several non-covalent interactions such as CH···π, π···π, lone pair (lp)···π and M···M interactions [23, 24].

The chemistry of transition metal complexes has been established recently on the growth and development of supramolecular assemblies, ensembles and different structural aggregates [25, 26] supramolecular assemblies also called synthons [27] or motifs [28], corresponds to the regions of the supramolecular structure where molecular recognition between the constituent functional groups occur. In supramolecular chemistry, non-covalent interactions and H-bond motifs that take place frequently in crystal structures are known as supramolecular synthons. Such interactions can be utilized for designing supramolecular architectures. Solid-state chemical research has got potential applications in molecular biology [29], material science [30] and pharmaceutical science [31-33]. The architecture of metal complexes is determined by the nature of metal ions and the used ligands. The chemical design of mono and binuclear copper complexes has drawn great attention from chemists because of type II copper proteins, such as superoxide dismutase, amine oxidase, galactose oxidase and dopamine-p-monooxygenase display unique active site properties [34].

Quantum chemical parameters derived from Density functional theory (DFT) calculations were employed as a physiochemical description of the complexes. DFT has vast applications in the development of the quantitative structure-activity relationship (QSAR) for the explanation of enzymatic and superoxide dismutase activity study. The theoretical parameters utilized are composed of energies of highest occupied molecular orbital (HOMO), energies of lowest unoccupied molecular orbitals (LUMO) energy gap (ΔE), ionization potential (I), electron affinity (EA), electronegativity (χ), chemical potential (μ), global hardness (η), softness (S), electrophilicity index (ω), electron-donating capacity (ω-) and electro accepting capacity (ω+). All these electronic parameters are analyzed and discussed. To the best of our knowledge with [HL= (Z)-N´-{(2-hydroxynapthalen-1-yl}methylene)acetohydrazide] copper(II) complexes have not been reported systematically until present work. Therefore, to explore the behaviour of copper(II) complexes with naphthyl hydrazone ligand with or without co-ligands we have focused the synthetic approach which persuade binary, mixed ligands and binuclear complexes. This chapter describes syntheses and structural characterization of nine copper(II) complexes with different nuclearties and geometries using tridentate hydrazone [HL= (Z)-N´-{(2-hydroxynapthalen-1-yl}methylene)acetohydrazide] *viz.*, $[Cu(HL)(OH_2]ClO_4$ **1,** $[Cu(HL)(OH_2)]ClO_4$ **2,** $[Cu(HL)(OH_2)]NO_3$ **3,** $[Cu(HL)(Cl)]$ **4,** $[Cu(HL)(DMPHEN)]ClO_4$ **5,** $[Cu(HL)(BZI)].CH_3OH$ **6,** $[(HL)Cu(\mu\text{-}ClO_4)Cu(L)(2H_2O)]$ **7,** $[(HL)Cu(\mu\text{-}SO_4)Cu(HL)(2H_2O)]$ **8** and [(HL)Cu(μ-bpm)Cu(HL)]$(ClO_4)_2.3H_2O$ **9 (**where DMPHEN = 2, 9-dimethyl-1,10-phenanthroline, BZI = benzimidazole and bmp = 2,2-Bipyrimidine).

The molecular structures of the newly synthesized complexes were evaluated using the single-crystal X-ray diffraction technique. The crystal structures confirmed the composition and geometry as proposed by other physicochemical methods. These complexes were further analyzed by Hirshfeld surfaces and fingerprint plots to assess the intermolecular interactions in the crystalline structures of complexes. The observed interactions have been discussed in detail. All complexes were further characterized by microanalysis, ultraviolet-visible (Uv-vis), infrared (IR) and electron paramagnetic resonance (epr) spectroscopy. The complexes were also studied using electrochemical (cyclic and differential pulse voltammetry) techniques. The DFT calculations were also performed to support the experimental findings. Bioactivity (catalytic) measurements have also been done and findings discussed.

2 Experimental

2.1 Materials

Copper metal salts were purchased from Sigma-Aldrich USA. 2-hydroxy-1-napthaldehyde and acetyl hydrazide was purchased from Across chemicals. Other chemicals and solvents were used of commercially available reagent quality.

Caution! Copper perchlorate hexahydrate with organic compounds is potentially explosive. During the use of this metal, salt precautions should be exercised.

2.2 Synthesis

2.2.1 Synthesis of Ligand (HL)

Schiff base ligand HL = N’-((2-hydroxynaphthalen-1-yl) methylene) acetohydrazide was synthesized by taking a solution of 2-hydroxy-1-napthaldehyde (1.50 g, 10.00 mmol) and acetyl hydrazide (0.65 g, 10.00 mmol) in ethanol (50 mL) with few drops of glacial acetic acid as a catalyst was refluxed for 1 hrs. The Schiff base was isolated from the resulting yellow solution. The obtained solid product from the solution was washed with cold ethanol and kept in a $CaCl_2$ desiccator.

Yield: 83%. Anal. Cal. for $C_{13}H_{12}N_2O_2$ (228.25 g mol^{-1}): Calc. C, 68.41; H, 5.30; N, 12.27%; Found C, 68.42; H 5.32; N, 12.29%. FTIR (KBr, cm^{-1}) 3441 ν(OH), 3185 ν(N-H), 1672 ν(C=O), 1643 ν(C=N). ^1H NMR (DMSO-d_6) δ: 12.6 (s, 1H, OH), 11.7 (s, 1H, NH), 9.1 (s, 1H, CH=N), 7.1-8.9 (d/t, 6H, napth-H), 2 (s, 3H, CH_3) ppm. ^{13}C NMR δ: 171.5 (C-OH), 165.7 (C=O), 145.1 (-CH=N-), 108.9-132.9 (m, 9C, naphtha-C), 21.8 (-OCH_3) ppm.

2.2.2 Synthesis of the complex $[Cu(HL)(OH_2]ClO_4$ 1 and $[Cu(HL)(OH_2]ClO_4$ 2

To a 20 mL methanolic solution of $Cu(ClO_4).6H_2O$ (0.370 g, 1.00 mmol) and the HL (0.228, 1.00 mmol) was added with two to three drops of triethylamine. The reaction mixture was stirred for 3 hrs and filtered. The filtrate was divided into two equal parts. One of the parts was left at room temperature for evaporation and the other was kept in a refrigerator (~10 °C). Blue coloured single crystals of **1** were obtained after one week from the filtrate which was left at room temperature, whereas dark blue single crystals of **2** were obtained after one month from the other part of the filtrate which was kept in the refrigerator. Crystals of both parts were collected upon filtration and dried in $CaCl_2$ desiccators.

Complex **1**, Yield; ~ 83%. Anal. Calc. for $C_{13}H_{13}ClCuN_2O_7$ (408.24 g mol^{-1}): Elemental Analysis: C, 38.25; H, 3.21; N, 6.86%; Found: C, 38.27; H, 3.19; N, 6.84%. Conductance (Λ_m/s cm^2 mol^{-1}) in DMSO 120. FTIR bands (KBr, cm^{-1}): ν(C=O) 1617, ν(C=N) 1598.

Complex **2**, Yield; ~ 82%. Anal. Calc. for $C_{13}H_{13}ClCuN_2O_7$ (408.25 g mol^{-1}): Elemental Analysis: C, 38.25; H, 3.24; N, 6.86%; Found: C, 38.24; H, 3.20; N, 6.82%. Conductance (Λ_m/s cm^2 mol^{-1}) in DMSO 130. FTIR bands (KBr, cm^{-1}): ν(C=O) 1618, ν(C=N) 1597.

2.2.3 Synthesis of the complex $[Cu(HL)(OH_2)]NO_3$ 3

Complex **3** was synthesized by mixing the methanolic solution of HL (0.228, 1.00 mmol) and $CuNO_3.3H_2O$ (0.242 g, 1.00 mmol). The reaction mixture was stirred for 3 hrs and filtered. The filtrate was left to stand overnight in the air when blue-coloured X-ray quality single crystals appeared at bottom of the vessel. These crystals were washed with methanol. The crystals were stored in the $CaCl_2$ desiccator.

Yield; ~ 78%. Anal. Calc. for $C_{13}H_{13}CuN_3O_6$ (370.80 g mol^{-1}): Elemental Analysis: C, 42.09; H, 3.56; N, 11.30%; Found: C, 42.11; H, 3.53; N, 11.33%. Conductance (Λ_m/s cm^2 mol^{-1}) in DMSO 119. FTIR bands (KBr, cm^{-1}): ν(C=O) 1618, ν(C=N) 1578.

2.2.4 Synthesis of complex [Cu(HL)(Cl)] 4

This complex was synthesized by taking a methanolic solution of HL (0.228, 1.00 mmol) and cupric chloride (0.170 g, 1.00 mmol). This mixture was stirred for 3 hrs. After 3 hrs the mixture was filtered and the filtrate was left for slow evaporation at room temperature. The crystals were formed from the solution after a few days on the slow evaporation of filtrate. These crystals were washed with distilled water and then from methanol to remove impurities. The crystals were stored in the $CaCl_2$ desiccator.

Yield; ~ 80%. Anal. Calc. for $C_{26}H_{24}Cl_2Cu_2N_4O_5$ (670.49): Elemental Analysis: C, 46.58; H, 3.61; N, 8.36%; Found: C, 46.50; H, 3.58; N, 8.39%. Conductance (Λ_m/s cm^2 mol^{-1}) in DMSO 21. FTIR bands (KBr, cm^{-1}): ν(C=O) 1592, ν(C=N) 1516.

2.2.5 Synthesis of the complex [Cu(HL)(DMPHEN)]ClO_4 5

To a 20 mL methanolic solution of $Cu(ClO_4).6H_2O$ (0.370 g, 1.0 mmol) and the HL (0.228 g,1.00 mmol) was added to a methanolic solution (10 ml) of DMPHEN (DMPHEN = 2,9-dimethyl-1,10-phenanthroline) (0.208 g, 1.0 mmol). The reaction mixture was stirred for 3 hrs and filtered. The filtrate was left for slow evaporation at room temperature. The crystals were formed from the solution after a few days on the slow evaporation of filtrate. These crystals were washed with distilled water and then methanol to remove impurities. The crystals were stored in the $CaCl_2$ desiccator.

Yield; ~ 68%. Anal. Calc. for $C_{27}H_{23}ClCuN_4O_6$ (598.48 g mol^{-1}): Elemental Analysis: C, 54.19; H, 3.87; N, 9.36%; Found: C, 54.21; H, 3.83; N, 9.35%. Conductance (Λ_m/s cm^2 mol^{-1}) in DMSO 119. FTIR bands (KBr, cm^{-1}): ν(NH) 3187, ν(C=N) 1601, ν(C=O) 1616, ν(ClO_4^-) 1052.

2.2.6 Synthesis of the complex [Cu(HL)(BZI)].CH_3OH 6

The procedure adopted for the synthesis of this complex was similar to that for complex **5**. A methanolic solution of BZI (BZI = Benzimidazole) (0.118 g, 1.0 mmol) was added instead of DMPHEN. The reaction mixture was stirred for 3 hrs. and filtered. The filtrate was left to stand overnight in the air when blue-coloured X-ray quality single crystals appeared at bottom of the vessel. These crystals were washed with methanol. The crystals were stored in the $CaCl_2$ desiccator.

Yield; ~ 73%. Anal. Calc. for $C_{21}H_{20}ClCuN_4O_3$ (439.95 g mol^{-1}): Elemental Analysis: C, 57.33; H, 4.58; N, 12.70%; Found: C, 57.34; H, 4.60; N, 12.73%. Conductance (Λ_m/s cm^2 mol^{-1}) in DMSO 17. FTIR bands (KBr, cm^{-1}): ν(C=N) 1590, ν(C=O) 1622.

2.2.7 Synthesis of the complex [(HL)Cu(μ-ClO_4)Cu(L)($2H_2O$)] 7

To a 20 mL methanolic solution of $CuClO_4.6H_2O$ (0.334 g, 2.00 mmol) and the HL (0.456 g, 2.00 mmol) was added with few drops of KOH (1 mmol). The reaction mixture was stirred for 3 hrs. The resulting deep blue solution was filtered. The filtrate was left for slow evaporation at room temperature. The blue coloured crystals of **7** have appeared after few days of slow evaporation of the filtrate. These crystals were washed with hot methanol and dried in a $CaCl_2$ desiccator.

Yield; ~ 82%. Anal. Calc. for $C_{26}H_{25}Cu_2N_4O_{10}Cl$ (716.03 g mol^{-1}); Elemental Analysis: C, 43.61; H, 3.52; N, 7.82%; Found: C, 43.62; H, 3.53; N, 7.80%. Conductance (Λ_m/s cm^2 mol^{-1}) in DMSO 27. FTIR bands (KBr, cm^{-1}): ν(C=N) 1599, ν(C=O) 1617, ν(NO_3^-) 1490.

2.2.8 Synthesis of the complex [(HL)Cu(μ-SO_4)Cu(HL)($2H_2O$)] 8

The synthetic procedure of complex **8** was similar to that for **7**. A methanolic solution of $CuSO_4.5H_2O$ (0.228g, 2.00 mmol) was taken instead of $CuClO_4.6H_2O$ and HL (0.456g, 2.00 mmol). The reaction mixture was then stirred for 3 hrs. In the reaction mixture, few drops of KOH were added and then filtered after some time. The filtrate was left for slow evaporation at room temperature. Blue-coloured X-ray quality single crystals of **8** appeared at bottom of the beaker. These crystals were washed with distilled water and then ethanol to remove impurities. The crystals were stored in a $CaCl_2$ desiccator.

Yield; ~ 78%. Anal. Calc. for $C_{26}H_{26}Cu_2N_4O_{10}S$ (713.66 g mol^{-1}): Elemental Analysis: C, 43.76; H, 3.67; N, 7.85%; Found: C, 43.75; H, 3.65; N, 7.84%. Conductance (Λ_m/s cm^2 mol^{-1}) in DMSO 13. FTIR bands (KBr, cm^{-1}): ν(C=N) 1606, ν(C=O) 1618, ν(NO_3^-) 1490.

2.2.9 Synthesis of the complex [(HL)Cu(μ-bpm)Cu(HL)](ClO_4)$_2$.$3H_2O$ 9

To a methanolic solution (20 mL) of $Cu(ClO_4)_2.6H_2O$ (0.334g, 2.00 mmol), the HL (0.456g, 2.00 mmol) was added and the resulting green solution was stirred at room temperature for 1 hrs. Then 10 ml methanolic solution of 2,2-bipyrimidine (0.158, 1.00 mmol) was added dropwise and the resulting reaction mixture gradually changed to dark blue. The resulting dark blue solution was stirred for 2 hrs and then filtered. The slow evaporation of filtrate at room temperature yielded dark blue crystals suitable for single-crystal X-ray analysis. These crystals were isolated and washed with methanol and stored in a $CaCl_2$ desiccator.

Yield; ~ 80%. Anal. Calc. for $C_{17}H_{18}ClCuN_4O_8$ (892.23 g mol^{-1}); Elemental Analysis: C, 45.74; H, 3.74; N, 12.58%; Found: C, 45.77; H, 3.73; N, 12.56%. Conductance (Λ_m/s cm^2 mol^{-1}) in DMSO 127. FTIR bands (KBr, cm^{-1}): ν(C=N) 1572, ν(C=O) 1631, ν(ClO_4^-) 1490.

2.3 Physical measurements

An Elementar Vario EL III Carlo Erba 1108 analyzer was used to perform elemental tests on the ligand and complexes. A Perkin-Elmer spectrophotometer was used to record FTIR spectra in the range 4000-400 cm^{-1}. On a Bruker Advance 400 (FT-NMR) multinuclear spectrometer, NMR spectra of HL were reported in DMSO-d_6. At room temperature, the accelerating voltage was 10 kV, and the spectra were registered. In quartz cells, UV-visible spectra were measured at 298K using a Shimadzu UV-Visible recording spectrophotometer UV-160. The EPR spectra were obtained using a Varian E-line Century Series X-band Spectrometer with a dual cavity and operating at X-band (9.4 GHz) with a modulation frequency of 100 kHz. As a field marker, TCNE was used. The EPR spectra were taken with frozen solutions in 3.0 103 M DMSO solution at liquid nitrogen temperature. The EPR spectra of polycrystalline samples and frozen solutions were measured using Varian quartz tubes. TGA was carried out with a TG-DTA 6300 INCARP EXSTAR 6000 at a heating rate of 10 °C/min in the temperature range. At room temperature, magnetic susceptibility measurements were taken on a Gouy balance for mercury(II) tetrathiocynato cobaltate(II) as the calibrating agent (g = 16.44106 cgs units). Electrochemical experiments were carried in a nitrogen atmosphere on a BAS-100 Epsilon electrochemical analyser with a three-electrode system and an electrochemical cell. The reference electrode was Ag/AgCl, the working electrode was glassy carbon, and the auxiliary electrode was platinum wire; the supporting electrolyte was 0.1 M $NaClO_4$ and the solvent was DMSO. A Systronics Conductivity 308 TDS device was used to measure the molar conductivities of freshly prepared 1.0 103 M DMSO solutions.

2.4 X-ray crystallography

The analysis of single crystals of complexes **1-9** was carried out on Bruker APEX-II CCD diffractometer with graphite monochromated CuKα radiation (λ = 1.54184 Å) from a fine focus sealed tube radiation source. No significant intensity variation was observed during data collection. Multi-scan absorption corrections were applied empirically to the intensity values using SADABS [35]. Data reductions were done by using the program Bruker SAINT [36]. The structures were solved by Direct Methods using the program SHELXS-97 [37] and refined with full-matrix least-squares based on F2 using the program SHELXL-97 [37]. All non-hydrogen atoms were refined anisotropically. For both structures, hydrogen atoms were first located in the Fourier difference map, then positioned geometrically and allowed to ride on their respective parent. The molecular graphics and crystallographic illustrations for both complexes were prepared using PLATON, [38] ORTEP [39] and WinGX [40] program.

2.5 Hirshfeld Surface Analyses (HSA)

Molecular Hirshfeld surfaces [41] in the crystal structure were examined based on the electron distribution calculated as the sum of spherical atom electron densities [42, 43]. For a given crystal structure and a set of spherical atomic densities, the Hirshfeld surface is unique [44]. The normalized contact distance (d_{norm}) based on both d_e and d_i (where d_e is the distance from a point on the surface to the nearest nucleus outside the surface and d_i is the distance from a point on the surface to the nearest nucleus inside the surface) and the vdW radii of the atom, as given by equation (1) enables identification of the regions of particular importance to intermolecular interactions [41]. The combination of d_e and d_i in the form of a two-dimensional (2D) fingerprint plot [45, 46] provides a summary of intermolecular contacts in the crystal [41]. The Hirshfeld surfaces mapped with d_{norm} and 2D fingerprint plots were generated using the Crystal-Explorer 2.1 [47]. Graphical plots of the molecular Hirshfeld surfaces mapped with d_{norm} used a red-white-blue colour scheme, where red highlights shorter contacts, white represents the contact around vdW separation, and blue is for longer contact. Additionally, two further coloured plots representing shape index and curvedness based on local curvatures are also presented in this paper [48].

$$d_{\mathrm{norm}} = \frac{d_i - r_i^{\mathrm{vdW}}}{r_i^{\mathrm{vdW}}} + \frac{d_e - r_e^{\mathrm{vdW}}}{r_e^{\mathrm{vdW}}} \qquad \ldots (1)$$

2.6 Computational Study

Full geometry optimizations were carried out using the density functional theory (DFT) method at the B3LYP level for complex [49]. All elements except Cu were assigned the 6-31G(d) basis set [50]. LANL2DZ with effective core potential for Cu atom was used [51]. The vibrational frequency calculations were performed to ensure that the optimized geometries represent the local minima and that there is only a positive Eigen value. In the computational model, the cationic complex was taken into account. All calculations were performed with the GAUSSIAN09 program, [52] with the aid of the Gauss View visualization program. Vertical electronic excitations based on B3LYP optimized geometries were computed using the time-dependent density functional theory (TDDFT) formalism [53] in DMSO, using a conductor-like polarizable continuum model (CPCM) [54].

2.7 Superoxide Dismutase activity

Inhibition of superoxide anion radical ($\mathrm{O_2^{\cdot-}}$) anion formation by alkaline DMSO (NBT assay) was evaluated using the nitro blue tetrazolium reduction method [55-57]. NBT reduction to $\mathrm{MF^+}$ by $\mathrm{O_2^{\cdot-}}$ was monitored spectrophotometrically at 560 nm. A unit of antioxidant SOD-like activity is the concentration of the complex, which causes 50% ($\mathrm{IC_{50}}$) inhibition of alkaline DMSO and mediated reduction of NBT. The $\mathrm{IC_{50}}$ values were evaluated from the percentage inhibition versus concentration plot [58, 59]. The catalytic rate constants were calculated as:

$$k_{\mathrm{M_CCF}} = k_{\mathrm{NBT}}[\mathrm{NBT}]/\mathrm{IC_{50}}$$

where $k_{\mathrm{NBT}}(\mathrm{pH}\ 7.8) = 5.94 \times 10^4\ \mathrm{M^{-1}S^{-1}}$[58, 59].

3 Results and Discussion

3.1 Synthetic Strategy

The monocondensed tridentate Schiff base ligand [HL = (Z)-N´-{(2-hydroxynapthalen-1-yl}methylene) acetohydrazide] was synthesized by condensation of 2-hydroxy-1-napthaldehyde and acetyl hydrazide in a 1:1 M ratio (Scheme 2). A series of copper (II) complexes employing HL, co-ligands and copper salts was synthesized using different methods and conditions (Scheme 3-5). The melting point of the ligand is 160 °C and for complexes, it is more than 250°C. With the possibility of fabrication of more than one synthetic product, we have come upon a procedure for selective synthesis of each complex by changing the reaction conditions such as concentration, temperature, or the reaction medium. Two polymorphs of the binary complexes $\mathrm{[Cu(HL)(OH_2)]ClO_4}$ (**1** and **2**) were achieved *via* the reaction of $\mathrm{CuClO_4}$ with HL. Their formation depends on reaction temperature (Scheme 2). Conditions for the formation of other binary, mixed ligand and binuclear complexes are clearly shown in Scheme

3-5. The ligand HL and its complexes were isolated as analytically pure blue to dark blue solids of moderate stability to air and moisture.

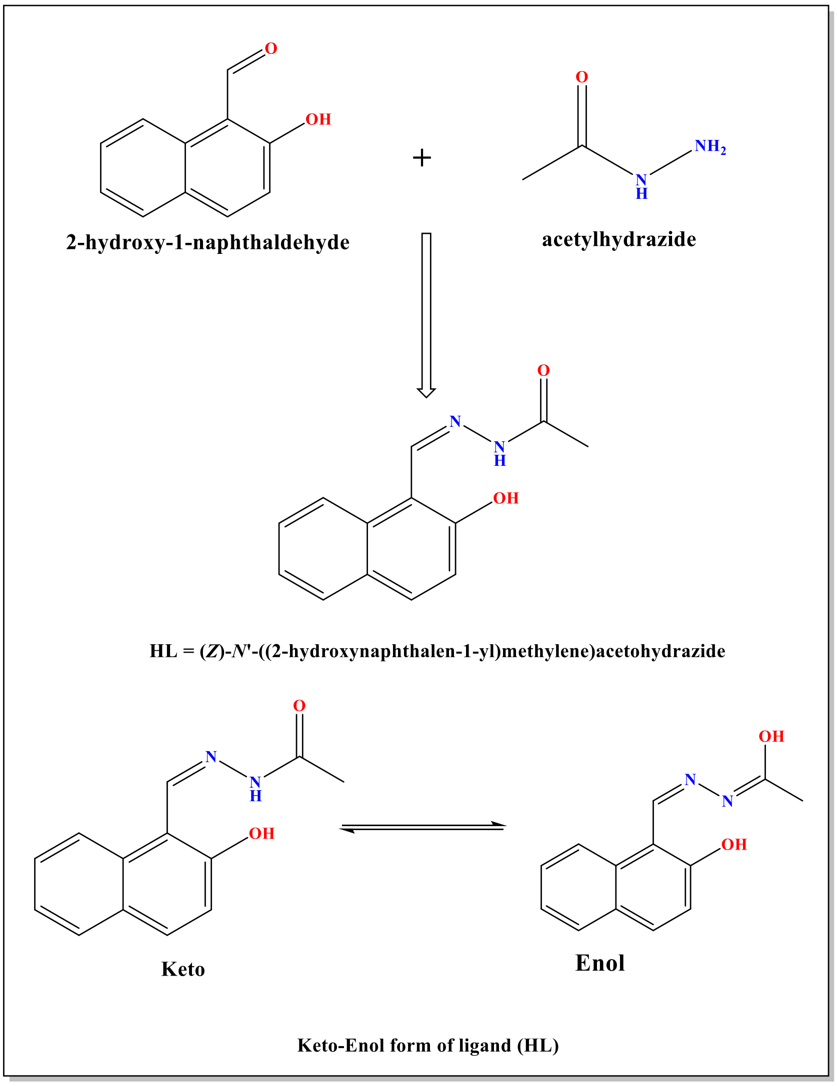

Scheme 2 Synthetic route of the ligand.

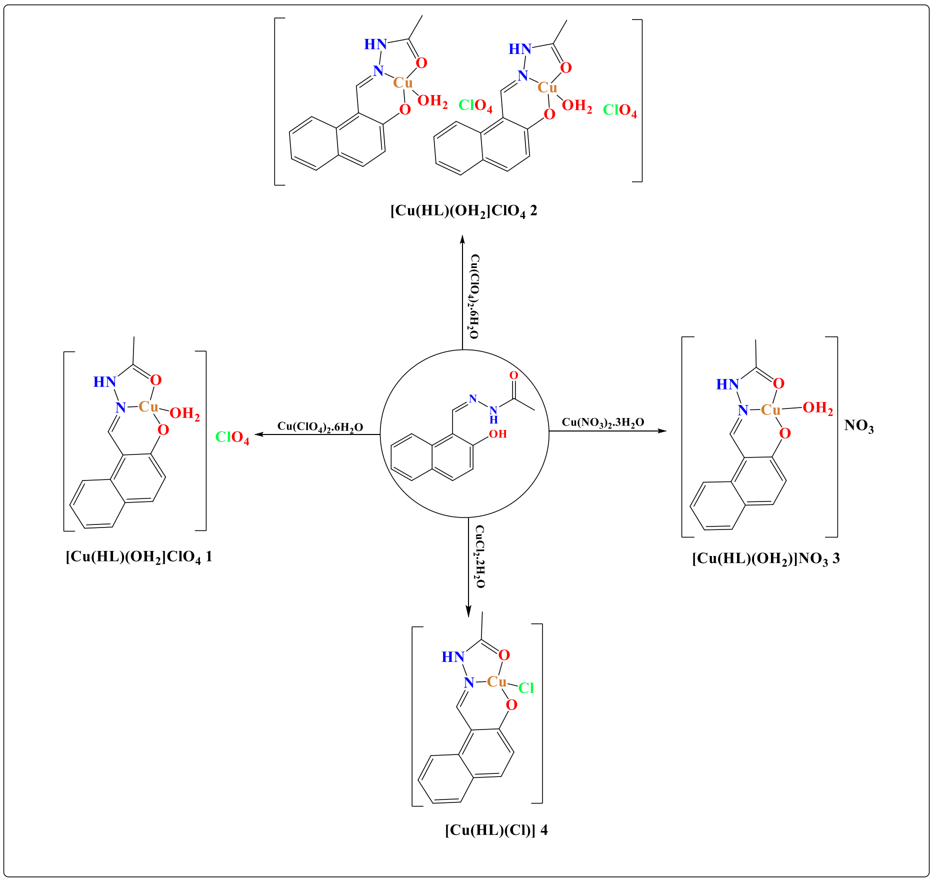

Scheme 3 Synthetic route of mononuclear complexes **1-4**.

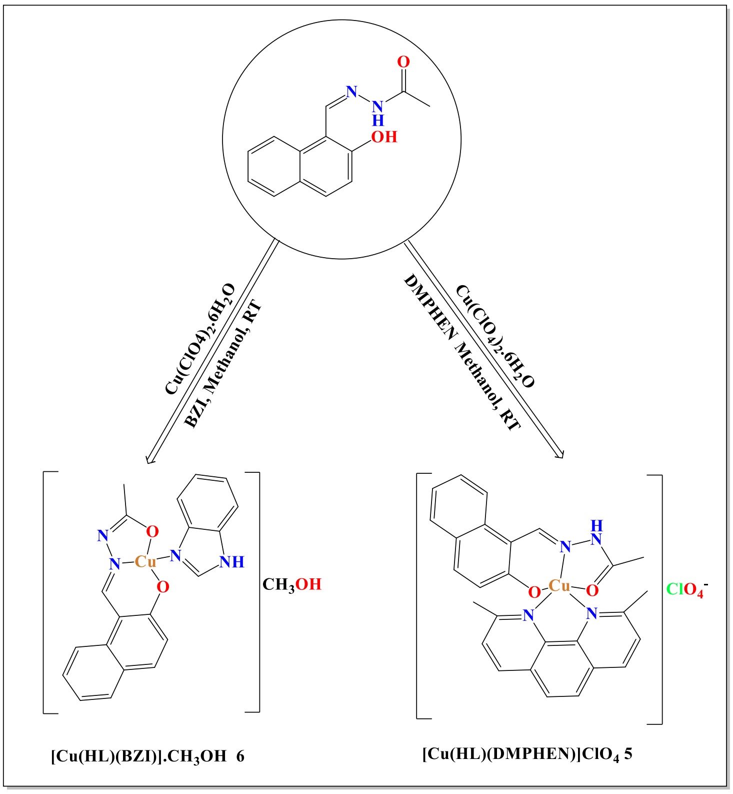

Scheme 4 Synthetic route of mixed ligand complexes **5** and **6**.

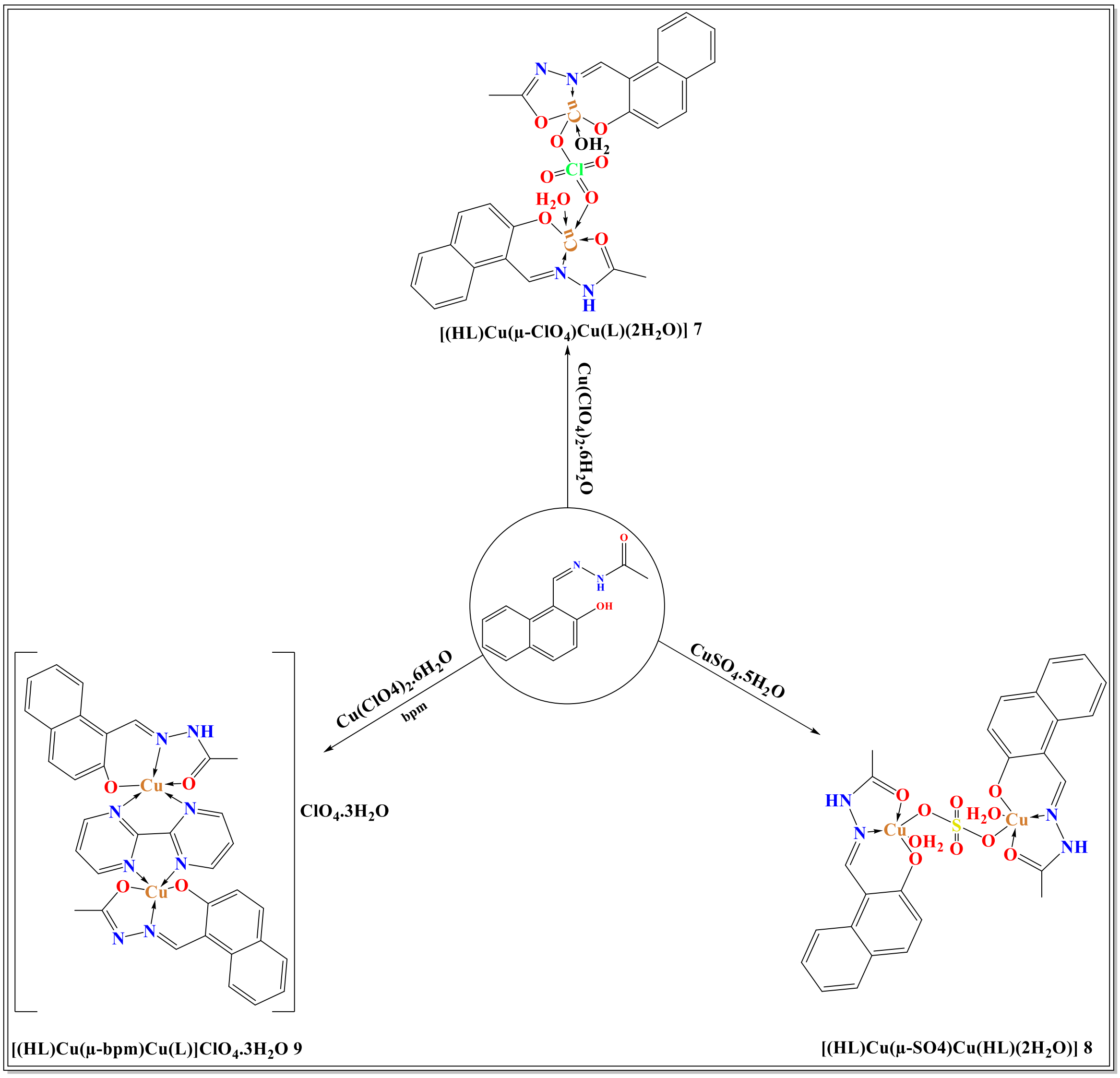

Scheme 5 Synthetic route of binuclear complexes **7-9**.

3.2 NMR studies of HL

The ^{1}H-NMR and ^{13}C-NMR spectra of HL were measured in DMSO-d_6. The NMR spectra of the ligand are shown in Fig. 1 and 2. In the ^{1}H-NMR spectrum, the peak at 12.645 ppm is due to 1H of OH of HL. Adjacent to these peaks one more peak is shown at 11.754 ppm by the proton of NH. The peak corresponding to the azo proton is observed at 9.143 ppm. The ligand HL showed multiplets in the range of 7.193-8.918 ppm corresponding to protons of napth-H. The sharp peak corresponding to CH_3 protons appeared at 2.028 ppm. [55, 60]. The ^{13}C-NMR spectrum showed characteristic peaks corresponding to C atoms of OH, C=O and C=N at 171.54, 165.70 and 145.4 ppm respectively. The 9 C atoms of naphthalene are observed in the range of 108.91-132.95 ppm [60, 61].

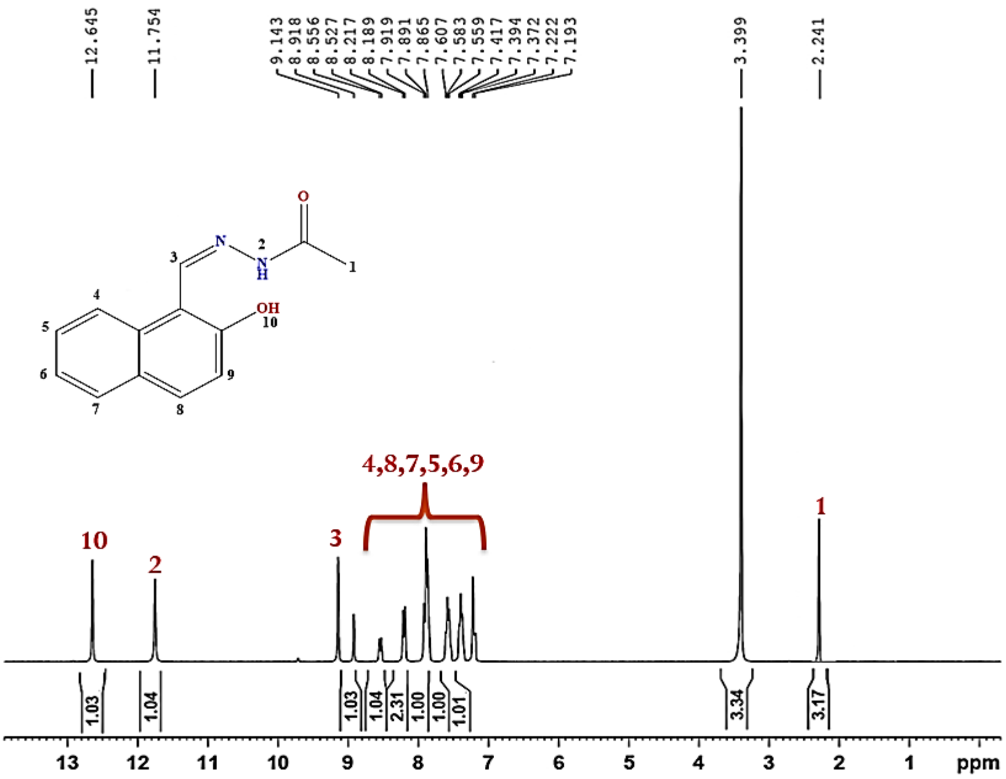

Fig. 1. ^{1}H-NMR spectrum Ligand HL in DMSO-d_6 solvent.

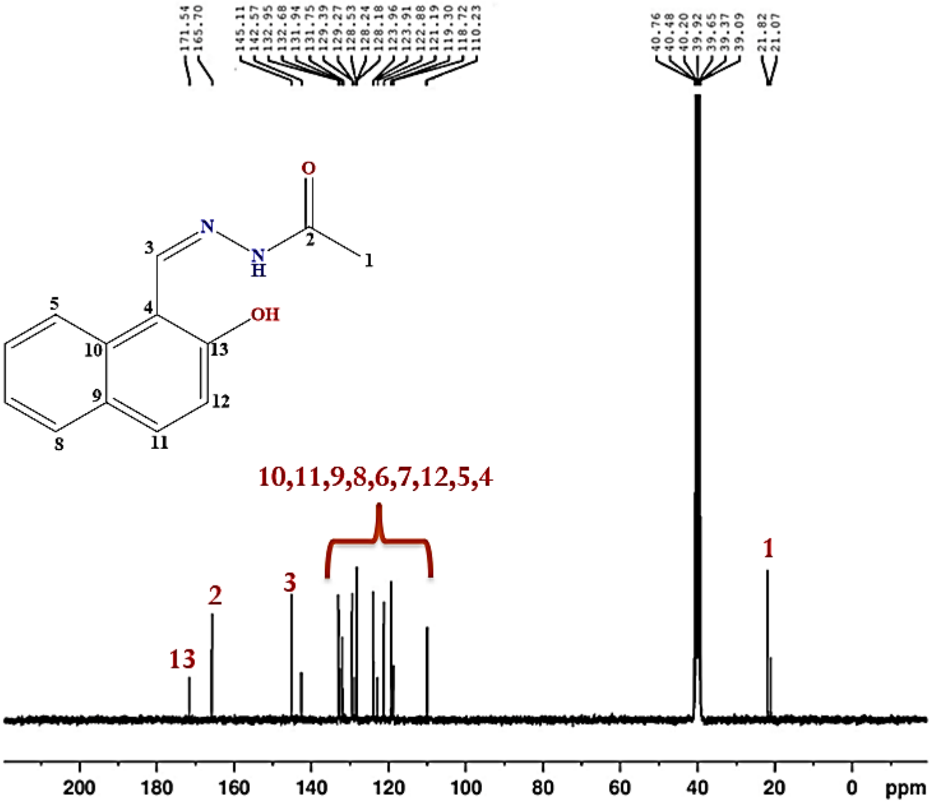

Fig. 2. ^{13}C-NMR spectrum of Ligand **HL** in DMSO-d_6 solvent.

3.3 FTIR spectroscopy

The FTIR spectra of ligand and complexes (**1-9**) were recorded in the range of 400-4000 cm^{-1}. The FTIR spectra of the free hydrazone ligand show a strong carbonyl ν(C=O) stretching frequency absorption at 1672 cm^{-1} and azomethine ν(C=N) stretching frequency at 1643 cm^{-1}. Similarly, two more stretching frequency is observed at 3441 cm^{-1} and 3185 cm^{-1} is due OH and NH group. The FTIR spectra of complexes **1-9** along with ligand are shown in Fig. 3-12.

The FTIR spectra of mononuclear complexes (**1-4**) along with ligand were recorded in the range 400-4000 cm^{-1}. Some important stretching frequencies are shown in Table 1. The absorption band of HL attributed to >C=N stretching is shifted to lower energies due to the coordination *via* the azomethine nitrogen (Table 1) [16, 62-67]. The band observed in complex **1** and **2** at around ~628 and ~1140 cm^{-1} suggest a T_d symmetry of perchlorate counterion [67-71]. The solid-state structures of both complexes were supported by single-crystal X-ray diffraction analysis [70]. The bonding of the non-ligand band to the copper ions is evidenced by the observed band in the range 437-493 cm^{-1} [72]. The FTIR spectra of the free hydrazone ligand show a strong C=O absorption band at 1672 cm^{-1} and an NH absorption band at 3185 cm^{-1}. In complexes, a shifting of the C=O band is observed towards the lower frequency region on coordination with giving strong evidence for ligand coordination [72-75] to the copper(II) ion. In complex **3**, the band around ~1384 is due to the presence of uncoordinated nitrate ions. The azomethine absorption band ν(C=N) in complexes is observed in the range of 1516-1598 cm^{-1}. Similarly, broad bands of coordinated water are observed in the range of 3050-3389 cm^{-1} in complexes **1-3**. In complex **4** a band at 3478 is due to an uncoordinated water molecule.

The FTIR spectra of complex **5** absorption band at 1052, 1002, 682 and 622 cm^{-1} suggest a T_d symmetry of perchlorate counterion [68-71]. The solid-state structures of both complexes were supported by single-crystal X-ray diffraction analysis [70]. The bonding of the non-ligand band to the copper ions is evidenced by the observed band in the range 437-476 cm^{-1} [72]. The FTIR spectra of both complexes (**5** and **6**) were recorded in the range 400-4000 cm^{-1}. Some important stretching frequencies are shown in Table 1. In the FTIR spectra absorption bands due to C=O were not observed in the FTIR spectra of both complexes and a new absorption band appears at 1388 and 1384 cm^{-1}**5** and **6** respectively, giving strong evidence for ligand coordination [73-75] to the copper(II) ion. In complex **6** observation band due to N-H was absent indicating coordination of hydrazone in the dionic (enol) form whereas in **5** it coordinates as monoionic (keto form).

In complexes **7** and **8** new broad band at 3354 and 3425 cm^{-1}which can be assigned to the ν(OH) vibration mode [76] had shown due to coordinated unidentate water molecules respectively. In complex **9** the appearance of a single strong band in the range 961-980 cm^{-1} suggests that the ClO^-_4 counter ion is present, as confirmed by the structural characterization [77]. In complex **7**, a new band at 1139, 1076 and 963cm^{-1} exhibited are due to perchlorate bridge ($M-ClO_4-M$) moiety [78-80]. The coordination of perchlorate depends to the metal atom; the local symmetry of the perchlorate group is reduced from T_d in the perchlorate ion C_{2v} or C_s in a bidentate perchlorate group. Four groups of bands are expected for the stretching vibration of bidentate perchlorate [68]. Similarly, new bands shown by complex is **8** and **9** are due to sulphate ($M-SO_4-M$) [80] in **8** and bpm (M-bpm-M) [81] bridging moieties stretching frequencies in **9** are shown in Table 1. The FTIR spectra of complexes (**7-9**) discussed here are characteristic of a compound containing bridging ($Cu-ClO_4$ –Cu, $Cu-SO_4-Cu$ and Cu-bpy-Cu) moieties. In each complex two non-ligand bands in the 423-477 cm^{-1} and 457-511 cm^{-1} regions are assigned to the ν(M-N) and ν(M-O) stretching vibrations, respectively [82].

Table 1 Important frequencies of FTIR spectral data.

Compounds	**ν(C=O)**	**ν(C=N)**	**ν(M-O)**	**ν(M-N)**
HL	1672	1643	- - -	- - -
1	1617	1598	493	441
2	1618	1597	492	439
3	1618	1578	491	447
4	1592	1516	469	434
5	1616	1601	476	459
6	1622	1590	456	437
7	1617	1599	457	423
8	1618	1606	456	427
9	1631	1572	511	477

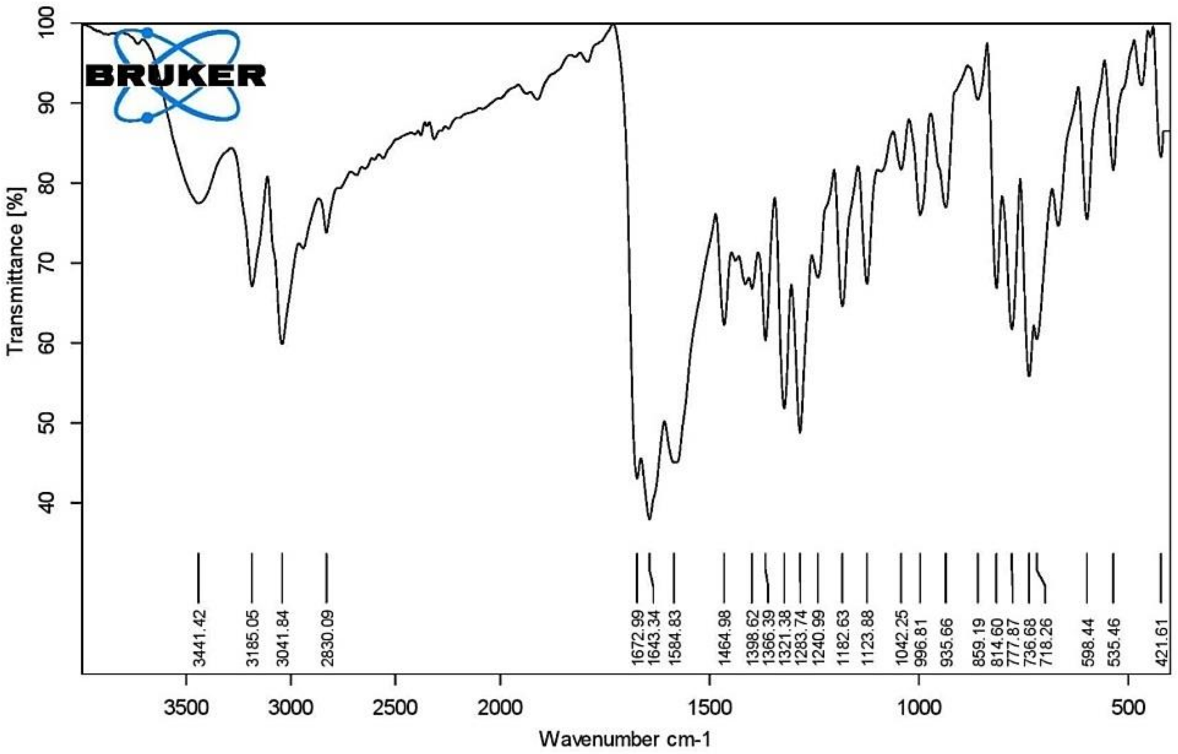

Fig. 3. FTIR spectrum of **HL**.

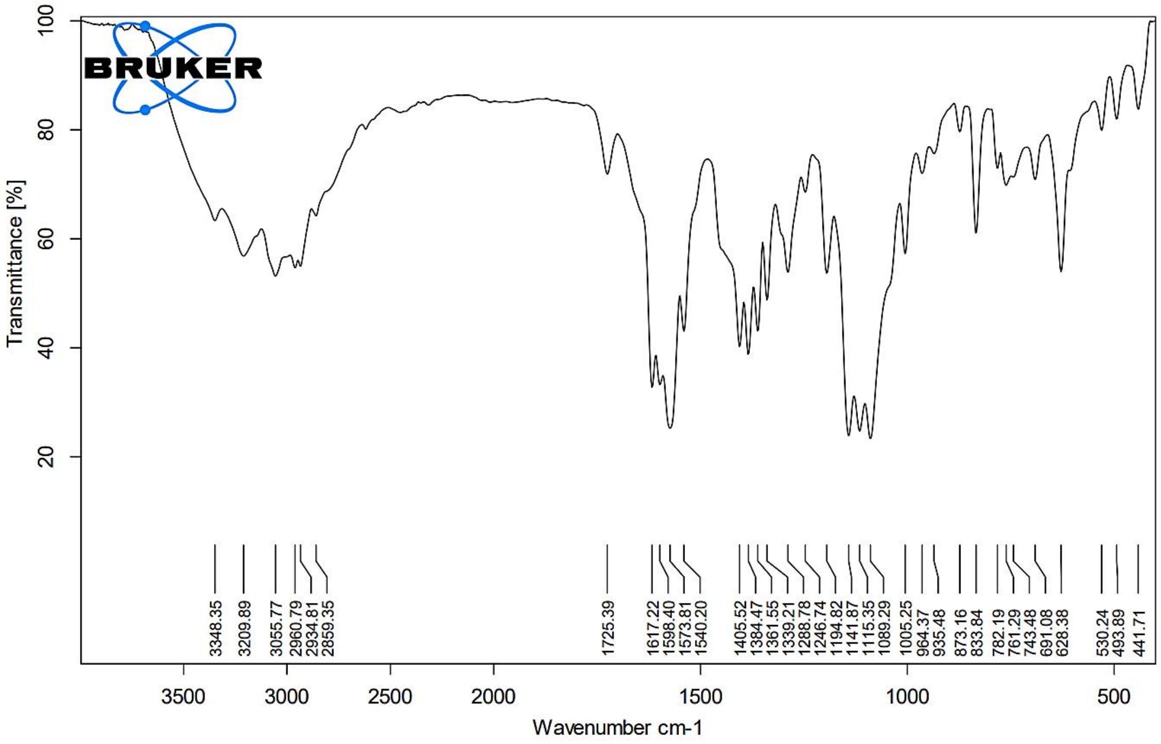

Fig. 4. FTIR spectrum of complex **1**.

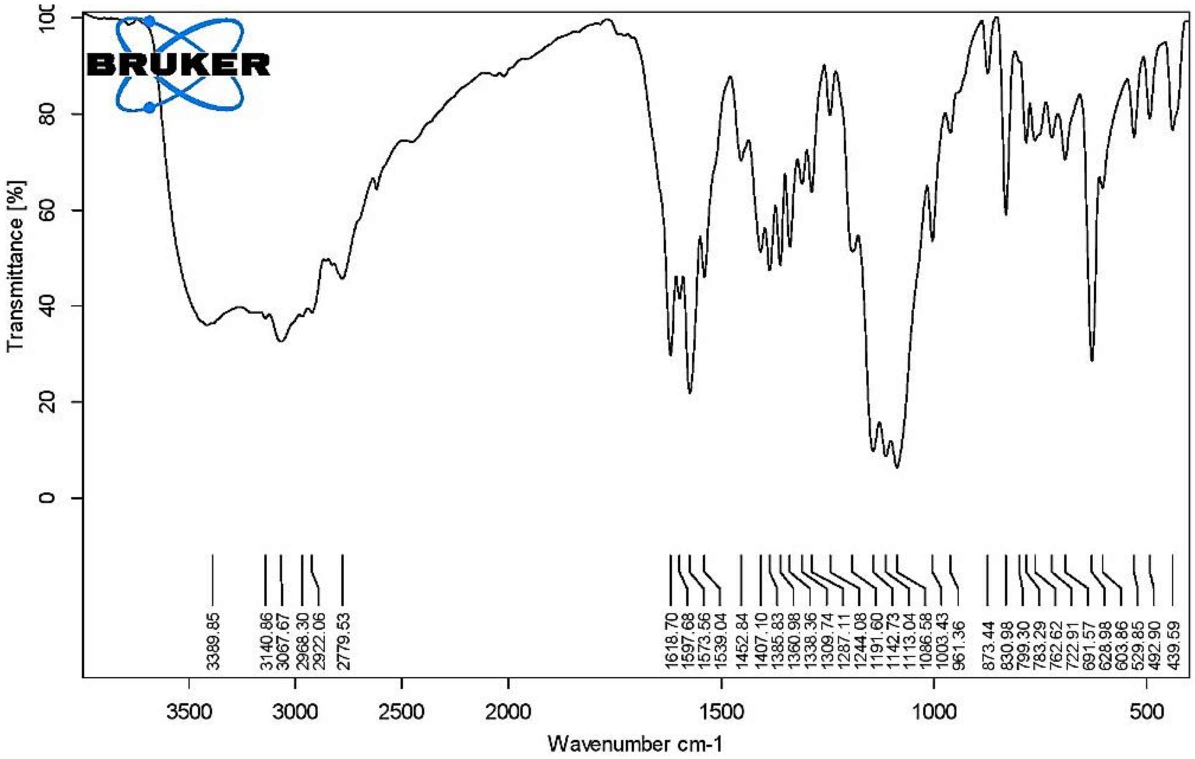

Fig. 5. FTIR spectrum of complex **2**.

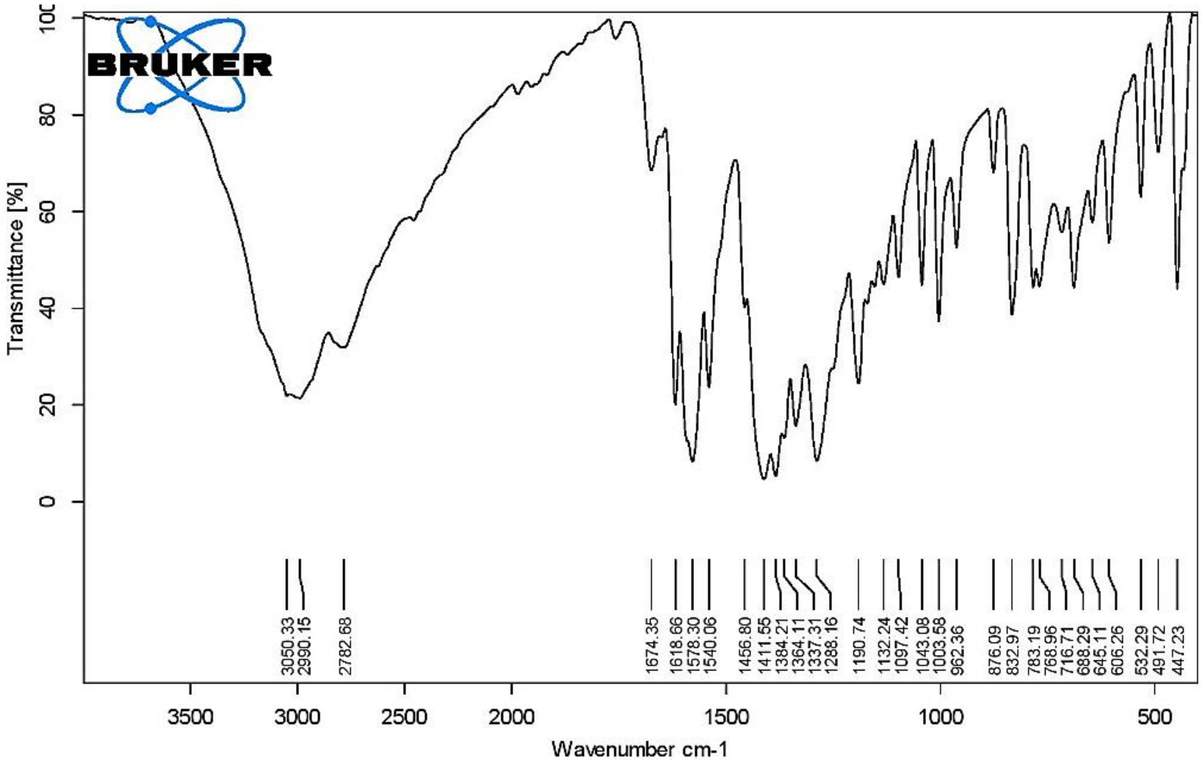

Fig. 6. FTIR spectrum of complex **3**.

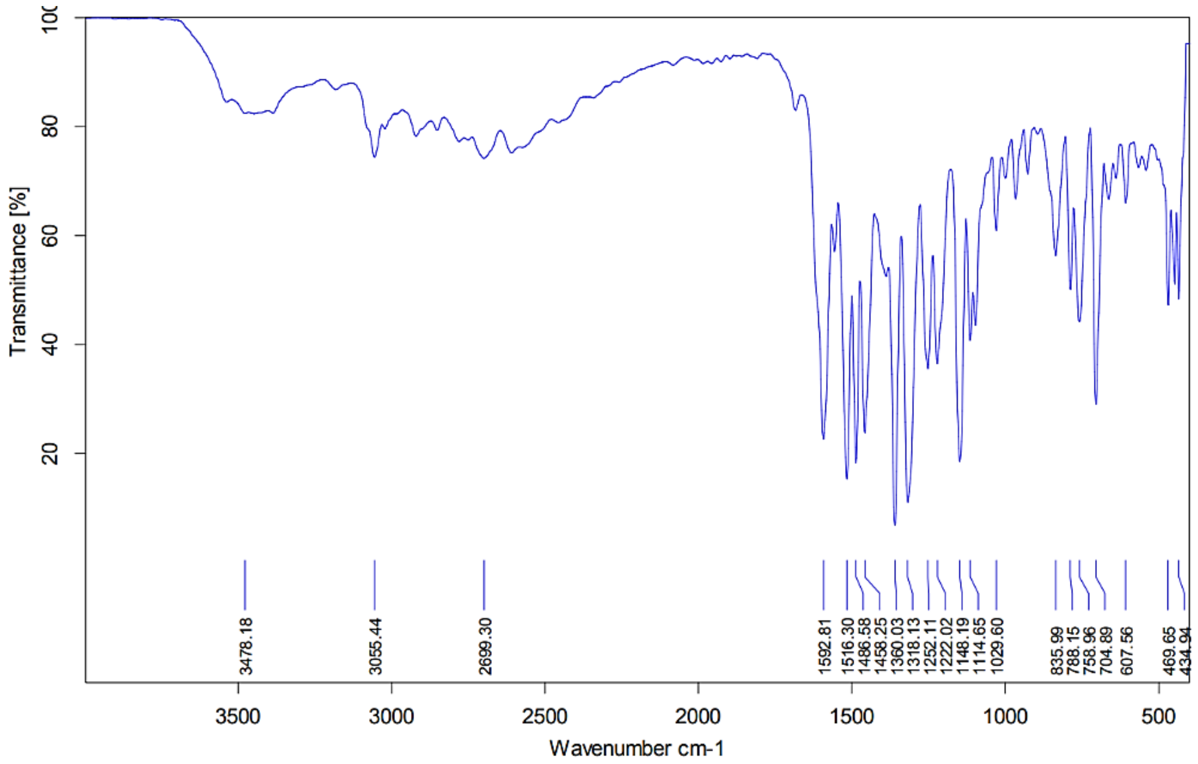

Fig. 7. FTIR spectrum of complex **4**.

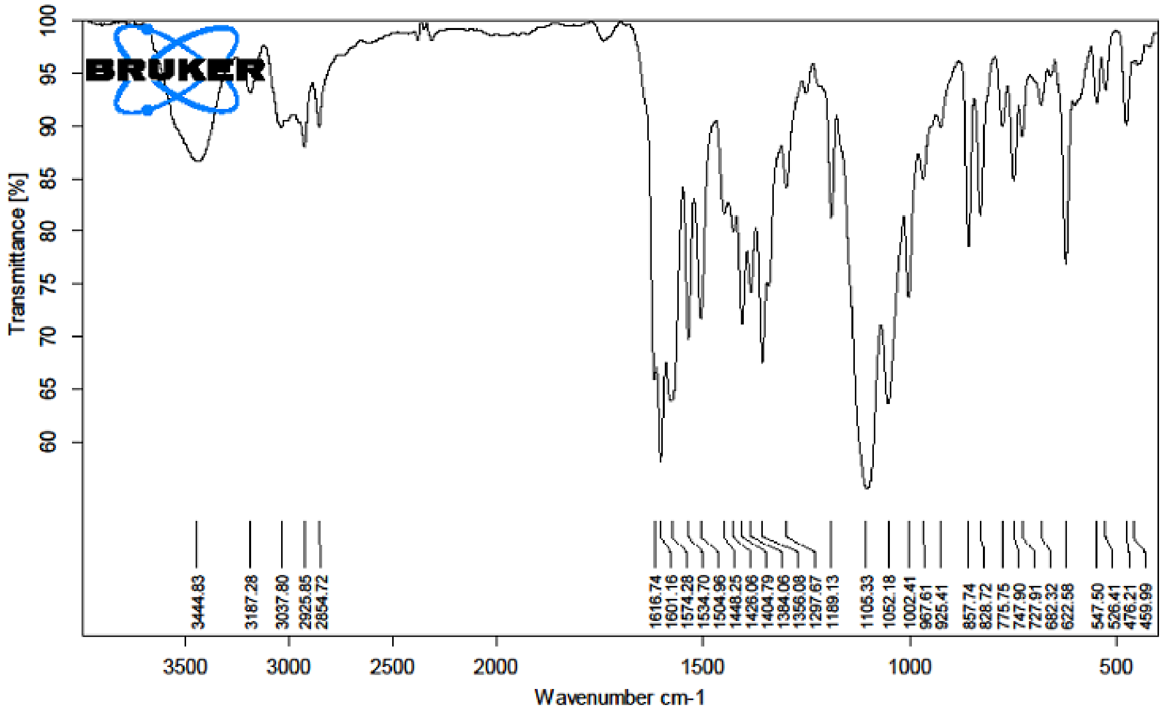

Fig. 8. FTIR spectrum of complex **5**.

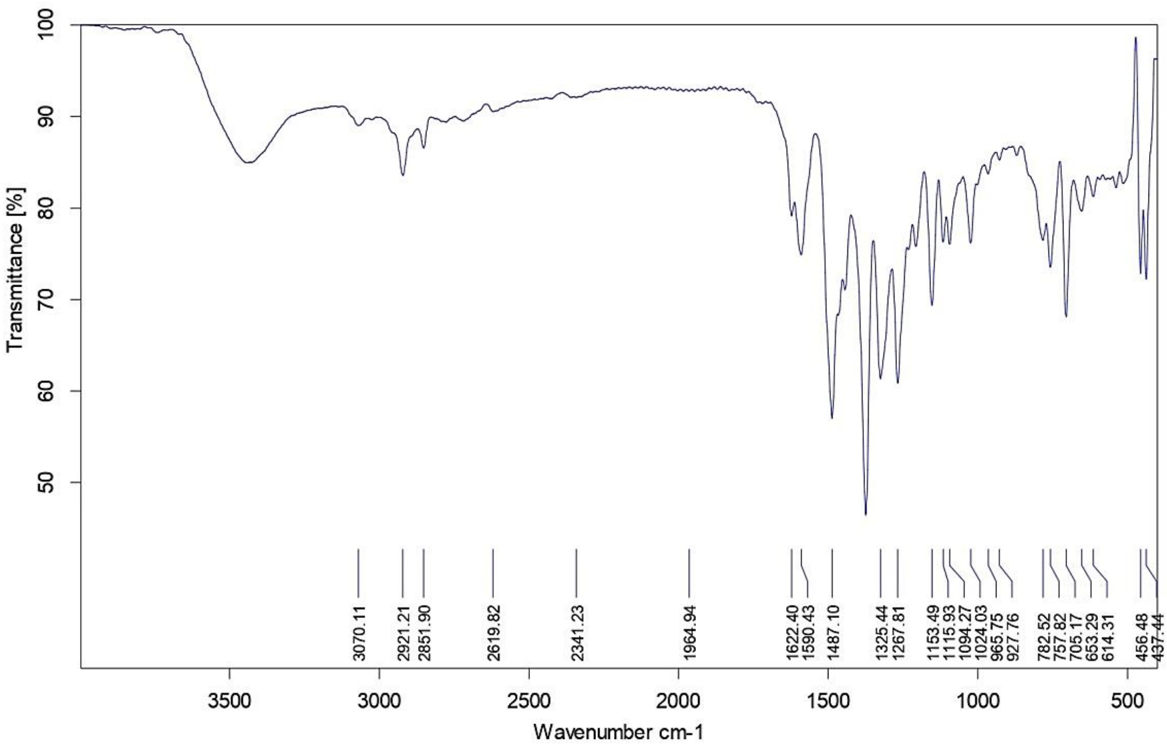

Fig. 9. FTIR spectrum of complex **6**.

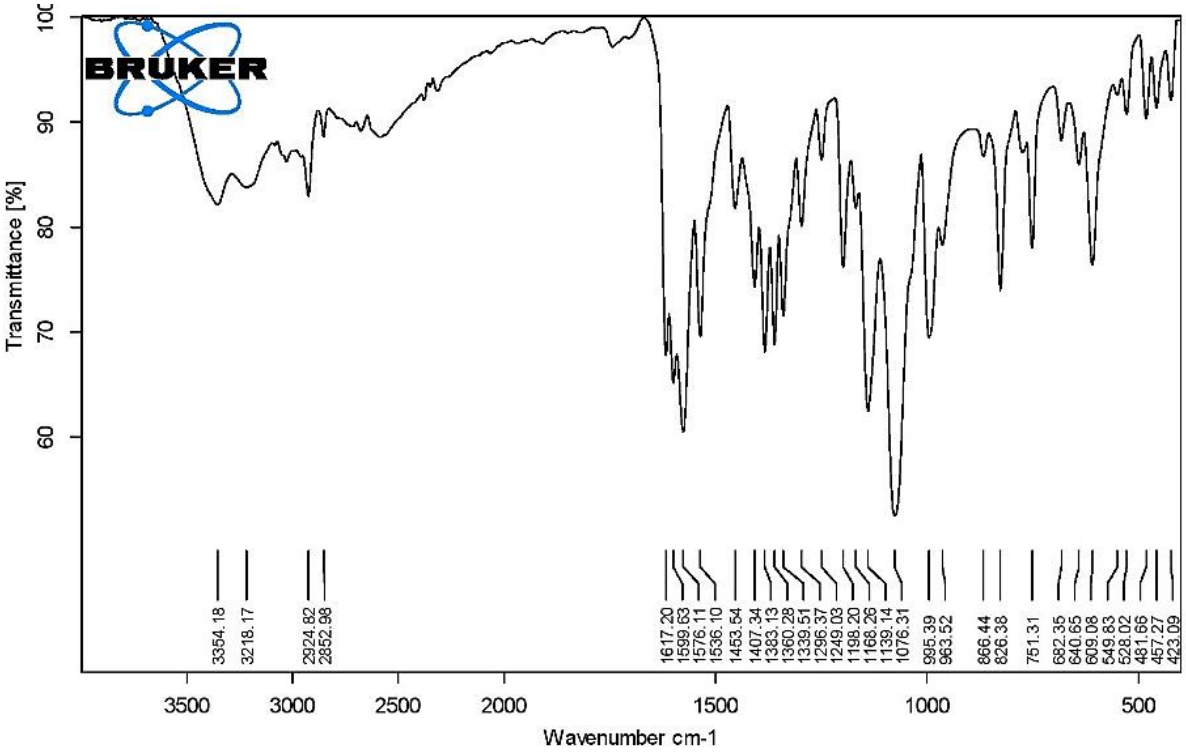

Fig. 10. FTIR spectrum of complex **7**.

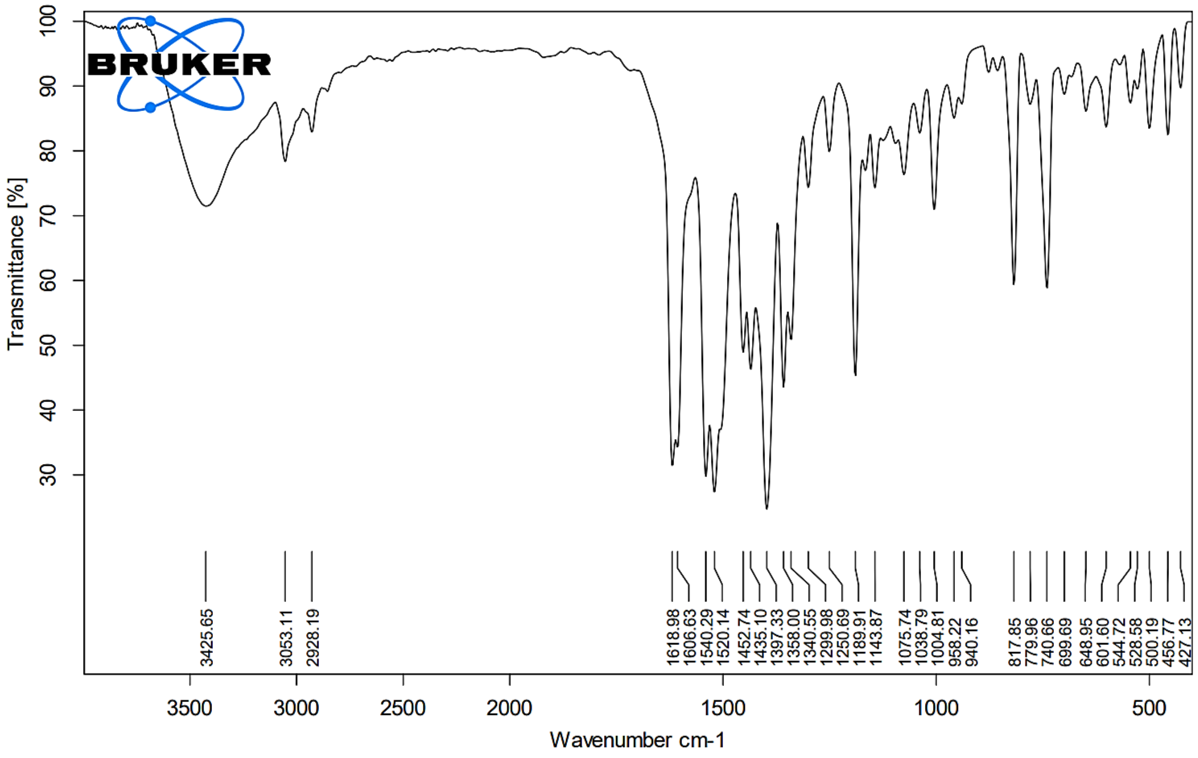

Fig. 11. FTIR spectrum of complex **8**.

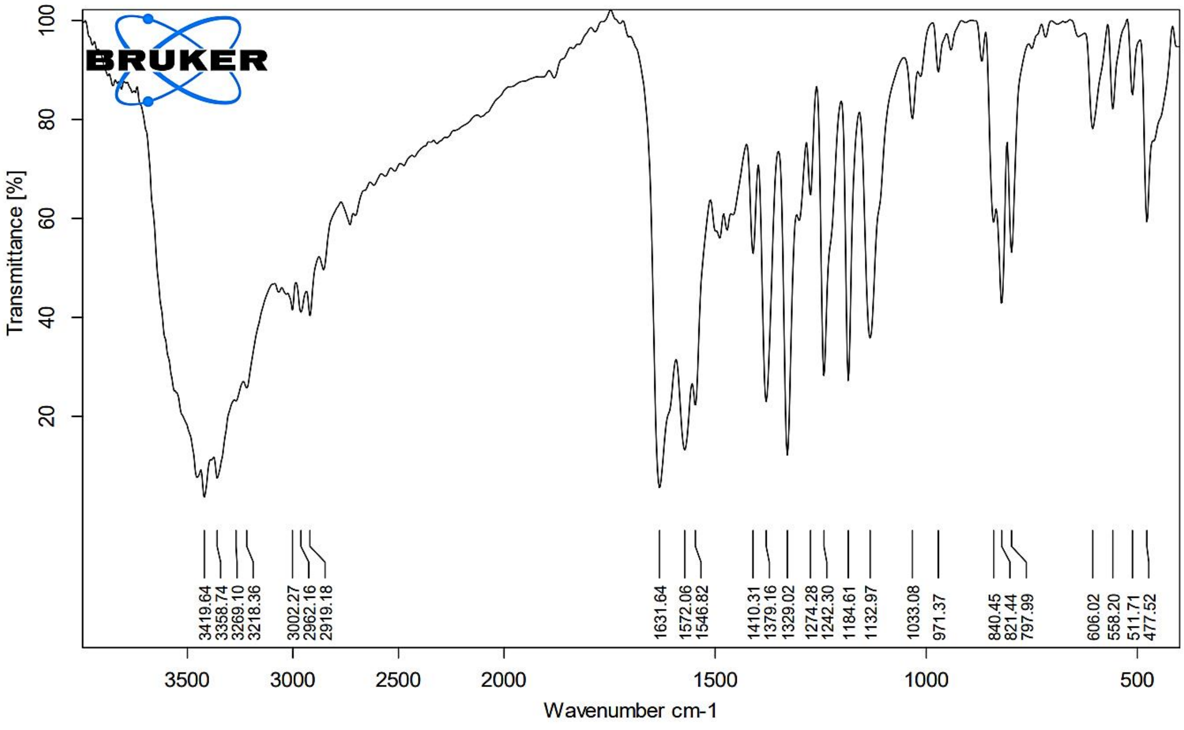

Fig. 12. FTIR spectrum of complex **9**.

3.4 Crystal Structures

3.4.1 Structures of mononuclear complexes 1-4

ORTEP diagram with atom-labeling plots of mononuclear complexes **1-4** are shown in Fig. 13-16. The crystal data of complexes **1-4** are presented in Table 2 and selected bond distances and angles (interatomic parameters) are summarized in Table 3.

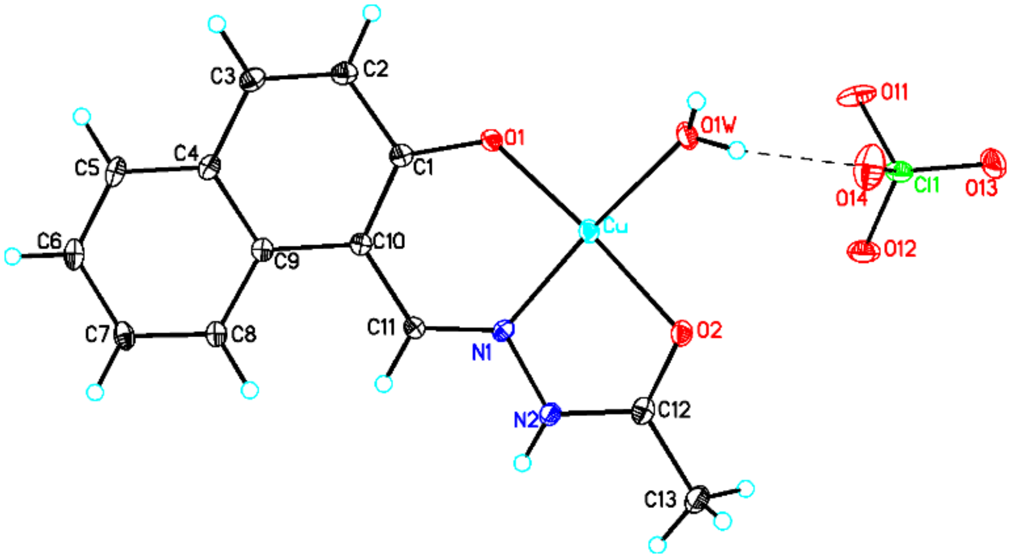

Fig. 13. ORTEP view of complex **1**.

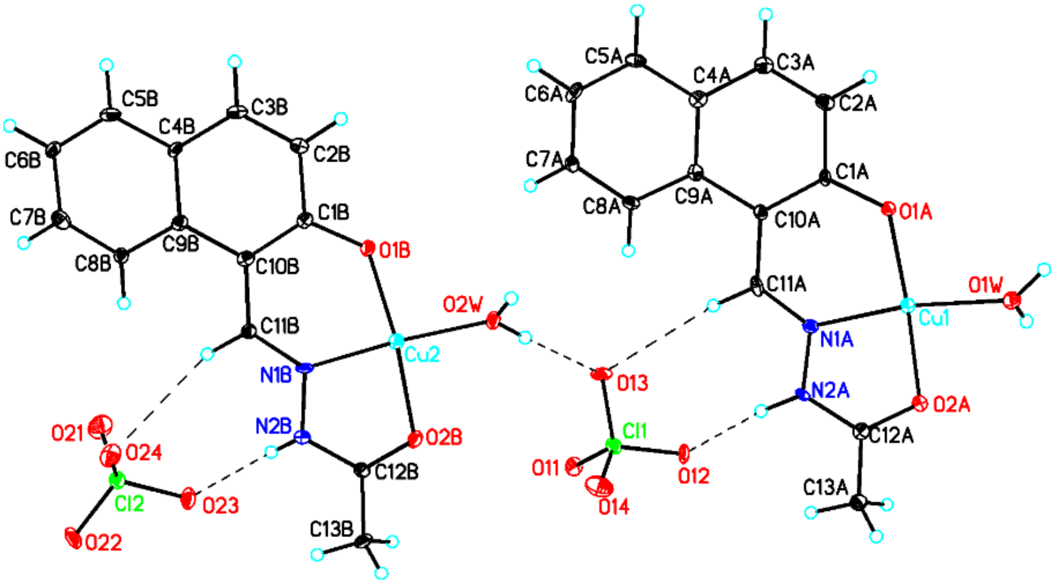

Fig. 14. ORTEP view of complex **2**(dimeric view).

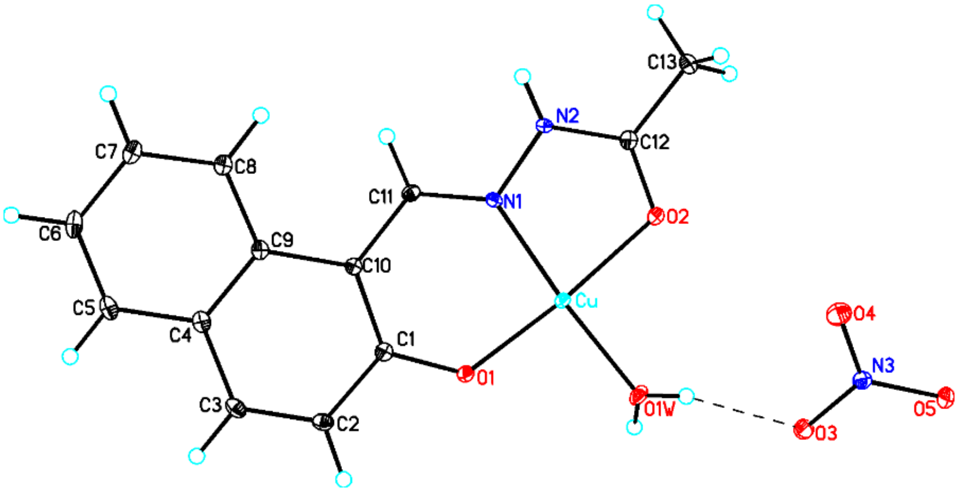

Fig. 15. ORTEP view of complex **3**.

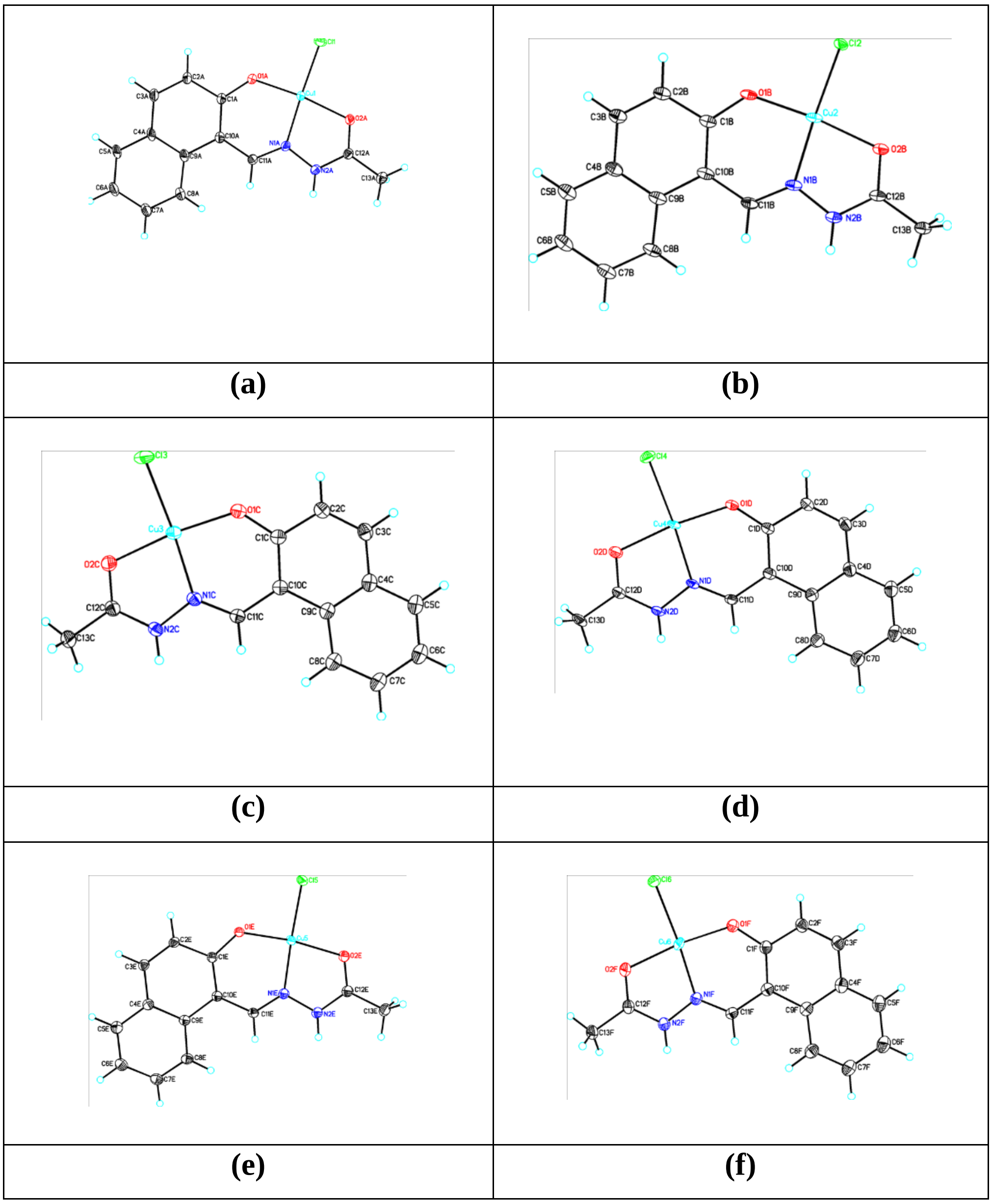

(a) (b)

(c) (d)

(e) (f)

Fig. 16. ORTEP view of complex **4** six containing six units (hexameric view) ((**a**)-(**f**)).

The copper ions in mononuclear complexes (**1-3**) have tetra-coordinated structures including a water molecule which can be readily replaced by a substrate as shown in Fig. 13-16. Complex **1** is mononuclear, whereas **2** shows dimer *via* H-bondings of perchlorate anion (Fig. 14). The asymmetric unit of **2** contains two chemically similar but crystallographically independent units. In these complexes (**1-4**) hydrazone ligands act as tridentate atom set ONO and are singly deprotonated at the O1 atom in the hydrazinato L^- form and copper(II) atom remains in a four coordinated square-planar ($CuNO_3$) geometry *via* water oxygen atom O1W being at a distance in the range 1.917-1.933 Å. In complex **4** again a square planar ($CuNO_2Cl$) coordination environment is observed at the copper(II) center in each discrete unit of the hexamer.

Table 2 Crystal data and structure refinement of complexes **1-4**.

	1	2	3	4
Empirical formula	$C_{13}H_{13}ClCuN_2O_7$	$C_{13}H_{13}ClCuN_2O_7$	$C_{13}H_{13}CuN_3O_6$	$C_{26}H_{24}Cl_2Cu_2N_4O_5$
Formula weight	408.24	408.24	370.80	670.47
Temperature (K)	100(2)	100(2) K	100(2)	123(2)
Wavelength (Å)	0.71073	0.71073	0.71073	0.71073
Crystal system	Triclinic	Triclinic	Triclinic	Triclinic
Space group	*P -1*	*P -1*	*P -1*	*P -1*
a (Å)	6.9261(2)	6.7676(8)	6.5243(3)	13.7161(5)
b (Å)	9.6299(2)	11.6637(16)	9.4250(4)	15.0921(6)
c (Å)	11.7237(3)	18.848(2)	11.3430(5)	22.3398(9)
α (°)	79.1380(10)	101.057(5)	98.115(2)	83.937(3)
β (°)	78.6780(10)	95.869(5)	93.768(2)	79.801(3)
γ (°)	74.6770(10)	97.346(6)	96.371(2)	64.504(4)
Volume ($Å^3$)	731.72(3)	1435.8(3)	683.90(5)	4105.9(3)
Z	2	4	2	6
Density (calculated) (Mg/m^3)	1.853	1.889	1.801	1.627
Absorption coefficient (mm^{-1})	1.717	1.750	1.635	1.793
F(000)	414	828	378	2040
Crystal size (mm^3)	0.19 x 0.16 x 0.11	0.22 x 0.18 x 0.08	0.25 x 0.20 x 0.15	0.32 x 0.17 x 0.15
Theta range for data collection (°)	2.640 to 28.395	3.061 to 25.635	2.636 to 28.445	2.077 to 25.252

Index ranges	-9<=h<=9, -12<=k<=12, -15<=l<=15	-7<=h<=8, -14<=k<=14, -22<=l<=21	-8<=h<=8, -12<=k<=12, -15<=l<=15	-16<=h<=16, -18<=k<=18, -26<=l<=26
Reflections collected	14285	11888	9705	102687
Independent reflections	3657 [R(int) = 0.0265]	5345 [R(int) = 0.0761]	3421 [R(int) = 0.0262]	14715 [R(int) = 0.1007]
Completeness to theta = 25.242°	99.8 %	99.2 %	99.7 %	98.9 %
Absorption correction	Semi-empirical from equivalents	None	Semi-empirical from equivalents	Semi-empirical from equivalents
Refinement method	Full-matrix least-squares on F^2	Full-matrix least-squares on F^2	Full-matrix least-squares on F^2	Full-matrix least-squares on F^2
Data / restraints /parameters	3657 / 62 / 269	5345 / 0 / 453	3421 / 0 / 221	14715 / 2895 / 1066
Goodness-of-fit on F^2	1.124	0.984	1.071	1.030
Final R indices [I>2sigma(I)]	R1 = 0.0340, wR2 = 0.0765	R1 = 0.0540, wR2 = 0.0868	R1 = 0.0243, wR2 = 0.0596	R1 = 0.0877, wR2 = 0.1930
R indices (all data)	R1 = 0.0452, wR2 = 0.0859	R1 = 0.1176, wR2 = 0.1067	R1 = 0.0282, wR2 = 0.0617	R1 = 0.2199, wR2 = 0.2507
Extinction coefficient	n/a	n/a	n/a	n/a
Largest diff. peak and hole (e. Å^{-3})	1.018 and -0.639	0.517 and -0.598	0.562 and -0.383	1.421 and -0.595

Table 3 Bond lengths [Å] and angles [°] of complexes **1-4**.

1					
Bond lengths					
	XRD	**DFT**		**XRD**	**DFT**
Cu-O(1)	1.8838(16)	1.8837	Cu-O(1W)	1.9331(18)	1.9332
Cu-N(1)	1.908(2)	1.908	Cu-O(2)	1.9514(17)	1.9515
Bond angles					
O(1)-Cu-N(1)	92.42(7)	92.41	O(1)-Cu-O(2)	175.01(7)	175.01
O(1)-Cu-O(1W)	92.43(8)	92.44	N(1)-Cu-O(2)	82.65(8)	82.64
N(1)-Cu-O(1W)	175.11(8)	175.11	O(1W)-Cu-O(2)	92.49(8)	92.48
2					
Bond lengths					
Cu(1)-O(1A)	1.877(4)	1.876	Cu(2)-O(1B)	1.877(4)	1.877

Cu(1)-N(1A)	1.895(4)	1.894	Cu(2)-N(1B)	1.901(4)	1.900
Cu(1)-O(1W)	1.924(4)	1.924	Cu(2)-O(2W)	1.920(4)	1.920
Cu(1)-O(2A)	1.935(4)	1.935	Cu(2)-O(2B)	1.955(4)	1.954
Bond angles					
O(1A)-Cu(1)-N(1A)	92.27(17)	92.27	O(1B)-Cu(2)-N(1B)	91.61(17)	91.61
O(1A)-Cu(1)-O(1W)	96.91(17)	96.93	O(1B)-Cu(2)-O(2W)	92.92(16)	92.91
N(1A)-Cu(1)-O(1W)	170.78(19)	170.79	N(1B)-Cu(2)-O(2W)	174.66(18)	174.65
O(1A)-Cu(1)-O(2A)	172.41(15)	172.42	O(1B)-Cu(2)-O(2B)	173.81(15)	173.81
N(1A)-Cu(1)-O(2A)	82.99(17)	82.99	N(1B)-Cu(2)-O(2B)	82.21(17)	82.22
O(1W)-Cu(1)-O(2A)	87.78(16)	87.78	O(2W)-Cu(2)-O(2B)	93.26(16)	93.26
3					
Bond lengths					
Cu-O(1)	1.8944(11)	1.8944	Cu-O(1W)	1.9174(12)	1.9175
Cu-N(1)	1.9027(13)	1.9028	Cu-O(2)	1.9583(11)	1.9584
Bond angles					
O(1)-Cu-N(1)	92.41(5)	92.41	O(1)-Cu-O(2)	174.86(5)	174.87
O(1)-Cu-O(1W)	91.98(5)	91.99	N(1)-Cu-O(2)	82.45(5)	82.46
N(1)-Cu-O(1W)	175.36(6)	175.35	O(1W)-Cu-O(2)	93.16(5)	93.15
4					
Bond lengths					
Cu(1)-O(1A)	1.894(3)	1.894	Cu(4)-O(1D)	1.891(3)	1.891
Cu(1)-N(1A)	1.927(3)	1.928	Cu(4)-N(1D)	1.923(3)	1.923
Cu(1)-O(2A)	1.989(3)	1.989	Cu(4)-O(2D)	1.988(3)	1.987
Cu(1)-Cl(1)	2.2135(18)	2.213	Cu(4)-Cl(4)	2.2137(18)	2.213
Cu(2)-O(1B)	1.896(3)	1.897	Cu(5)-O(1E)	1.894(3)	1.894
Cu(2)-N(1B)	1.925(3)	1.925	Cu(5)-N(1E)	1.925(3)	1.924
Cu(2)-O(2B)	1.990(3)	1.990	Cu(5)-O(2E)	1.990(3)	1.990
Cu(2)-Cl(2)	2.2125(18)	2.212	Cu(5)-Cl(5)	2.2142(18)	2.214
Cu(3)-O(1C)	1.891(3)	1.891	Cu(6)-O(1F)	1.891(3)	1.892
Cu(3)-N(1C)	1.923(3)	1.923	Cu(6)-N(1F)	1.925(3)	1.924
Cu(3)-O(2C)	1.988(3)	1.988	Cu(6)-O(2F)	1.988(3)	1.986
Cu(3)-Cl(3)	2.2143(19)	2.214	Cu(6)-Cl(6)	2.2123(19)	2.212
Bond angles					
O(1A)-Cu(1)-N(1A)	90.83(16)	90.82	O(1D)-Cu(4)-N(1D)	91.54(16)	91.55
O(1A)-Cu(1)-O(2A)	171.2(2)	171.20	O(1D)-Cu(4)-O(2D)	172.85(19)	172.85
N(1A)-Cu(1)-O(2A)	81.34(15)	81.34	N(1D)-Cu(4)-O(2D)	81.60(15)	81.60
O(1A)-Cu(1)-Cl(1)	92.73(14)	92.72	O(1D)-Cu(4)-Cl(4)	92.31(13)	92.32
N(1A)-Cu(1)-Cl(1)	171.9(3)	171.9	N(1D)-Cu(4)-Cl(4)	175.3(2)	175.3
O(2A)-Cu(1)-Cl(1)	95.55(14)	95.54	O(2D)-Cu(4)-Cl(4)	94.64(13)	94.64
O(1B)-Cu(2)N(1B)	90.69(16)	90.68	O(1E)-Cu(5)-N(1E)	90.88(16)	90.88
O(1B)-Cu(2)O(2B)	168.2(3)	168.2	O(1E)-Cu(5)-O(2E)	170.5(3)	170.5
N(1B)-Cu(2)O(2B)	81.36(15)	81.35	N(1E)-Cu(5)-O(2E)	81.32(15)	81.32

O(1B)-Cu(2)-Cl(2)	92.72(13)	92.72	O(1E)-Cu(5)-Cl(5)	92.66(13)	92.66
N(1B)-Cu(2)-Cl(2)	175.7(2)	175.7	N(1E)-Cu(5)-Cl(5)	176.0(2)	176.0
O(2B)-Cu(2)-Cl(2)	95.66(13)	95.66	O(2E)-Cu(5)-Cl(5)	95.33(13)	95.34
O(1C)-Cu(3)N(1C)	91.39(16)	91.38	O(1F)-Cu(6)-N(1F)	91.39(16)	91.38
O(1C)-Cu(3)O(2C)	172.3(2)	172.3	O(1F)-Cu(6)-O(2F)	172.91(17)	172.92
N(1C)-Cu(3)O(2C)	81.62(15)	81.62	N(1F)-Cu(6)-O(2F)	81.55(15)	81.56
O(1C)-Cu(3)-Cl(3)	92.38(14)	92.39	O(1F)-Cu(6)-Cl(6)	92.38(14)	92.37
N(1C)-Cu(3)-Cl(3)	176.07(18)	176.08	N(1F)-Cu(6)-Cl(6)	175.8(2)	175.8
O(2C)-Cu(3)-Cl(3)	94.67(14)	94.68	O(2F)-Cu(6)-Cl(6)	94.69(14)	94.68

The bond distances of Cu1-N1, Cu1-O1, Cu1-O2 and Cu1-O1W remain in the range 1.908(2), 1.884(16), 1.951(17) and 1.938(18) Å for **1**, 1.895(4), 1.877(4), 1.935(4) and 1.924(4) Å for **2** and 1.9027(13), 1.844(11), 1.958(11) and 1.917(12) Å for **3,** respectively. The donor atoms form two chelate rings which are fused *via* Cu1 N1 bond and thus two chelate rings are formed. One chelate ring is five coordinated with the hydrazone part of HL and the other six-membered rings are formed by the aldehyde residue of the HL. The bond distances and bond angles are agreed very well with those reported similar copper(II) complexes [83]. In complexes **1** and **2,** there are no meaningful interactions in axial positions. Though there is no direct bond between the two molecular units. The perchlorate O atoms act as hydrogen bond acceptors and form the dimeric structure of complex **2**. The neighbouring contact in complex **2** in between two molecular units is 9.740 Å (Fig. 17).

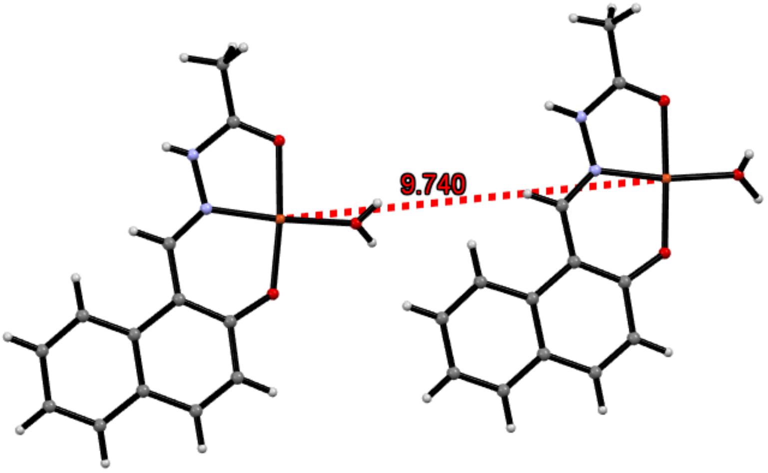

Fig. 17. The neighbouring contact in complex **2**.

In these complexes (**1** and **2**) deviations of tetra coordinated donor atoms O1, N1, O2 and O1W from their plane are 0.11Å for **1** whereas the four donor atoms are partly coplanar in **2**, with an rms of 0.006 Å. The central copper(II) atom deviates marginally from the based plane by ~ 0.044(6) Å in **1** and ~0.051 Å in **2**. The tetrahedral distortion is possible in **1** since one pair of associated trans donor atoms (O1 O2 and N1 O1W) apparently lie below the plane while the other pair is above the plane with the copper ion in the mean plane. The geometry index for four coordinate complexes τ_4 (= 360 – (α + β) / 141º) is 0.11 for **1** and 0.07 for **2**. Where sum of the angles α + β = the two largest angles in the four-coordinate complex [84-86]. The value of τ_4 will range from 1.00 for a perfect tetrahedral to 0 for a perfect square planar geometry. Thus, such a low geometry index τ_4 reveals a slightly distorted square planar geometry in these complexes. The dihedral angles between the two planes N1 Cu O2 and O1 Cu O1W are ~10.5 Å for **1** and ~5.25 Å for **2**. Such distorted square planar geometry has been explored for other similar complexes containing tridentate ligand [83].

The molecular structures of complex **3** are similar to those of complexes **1** and **2** concerning the coordination geometry with nitrate as a counter ion in **3**. This complex copper centre exhibits geometry index τ_4 = 0.07, which indicates slightly distorted square planar geometry similar to geometries of **1** and **2**.

The molecular structure of complex **4** is shown in Fig. 16. Molecular crystal refinement data are given in Table 2. Some important and interatomic distances and angles are show parameters in Table. 3. Hydrogen bonding parameters are also collected in Table 4. The complex crystallizes in the triclinic space group *P-1*. In this complex, there are six discrete molecules of [Cu(HL)(Cl)] in the asymmetric unit, which have similar structures. In these discrete units, each copper atom has four coordinate geometry. The tridentate Schiff base ligand coordinated type coordinate through O1A, O2A and N1A. The fourth position is occupied by chlorine atom (Cl1). For the present complexes, τ_4 show the value are ~0.119, ~0.114, ~0.083, ~0.084, ~0.096 and ~0.080 for Cu_1 and Cu_6 centres, respectively. Such values confirm the distorted square planar geometry around each copper centre of each distance unit. The chlorine atom of each discrete unit is responsible for the formation of the hexamer. Although there is no discrete bond among these discrete units. The intermolecular Cu-Cu distance is 5.657 Å (Fig. 18).

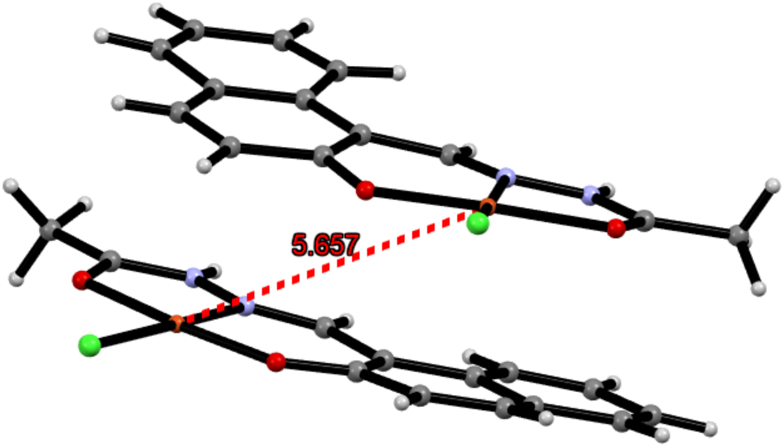

Fig. 18. The intermolecular distance in complex **4**.

3.4.2 Supramolecular assembling of complexes 1-4

In complex **1** hydrogen bond networks are present. The carbonyl moiety of HL and free perchlorate anions behave as H-bond acceptors towards the acetyl, azo and imine moieties of HL ligands resulting in the formation of a supramolecular network (Fig. 19 and 20). In this supramolecular cluster, two types of H-bond interaction are observed.

(i) Classical H-bonds in between H atoms of acetyl, azo and imine moieties of HL ligands and bound water and O atoms of carbonyl and O atoms of a free perchlorate ion (Fig. 19).

(ii) Bifurcated H-bonds between the H-atoms of acetyl moiety of HL ligands and O atoms of carbonyl moiety of HL and free perchlorate anions. O14 atoms of free perchlorate anions act as doubly H-bond acceptors. Thus, two H-bonds forms in a tetramer like association among the four units of complex in four extended heterosynthon (motif) $R_2^2(8)$. In this complex, three categories of C-H···π interactions (Fig. 20). C-H···π is the interaction of H-atom with a π-system of an aromatic or aryl ring. The classical image of a C-H···π interactions is a T-shape with interacting H atoms generally directly over the centre of aryl or chelate ring. Measurements of distances (CH···π) and horizontal distance (2.512 Å) were evaluated. Type I, C-H···π (aryl) intramolecular interactions have the distance (CH···π) 3.392 Å. Type II, C-H···π (metal chelate) intermolecular interactions with distances (CH···π) 3.186 Å. In this complex again π···π interactions (aryl and metal chelates) in between phenyl ring of one unit with a metal chelate ring of the neighbouring unit were observed with Cg···Cg(π···π) distances of 3.575 Å (Fig. 20) These π···π stacking, H-bonding and CH···π interactions lead to the formation of three-dimensional supramolecular interactions. The crystal packing diagram is viewed along the c axis containing two molecular units (Fig. 21).

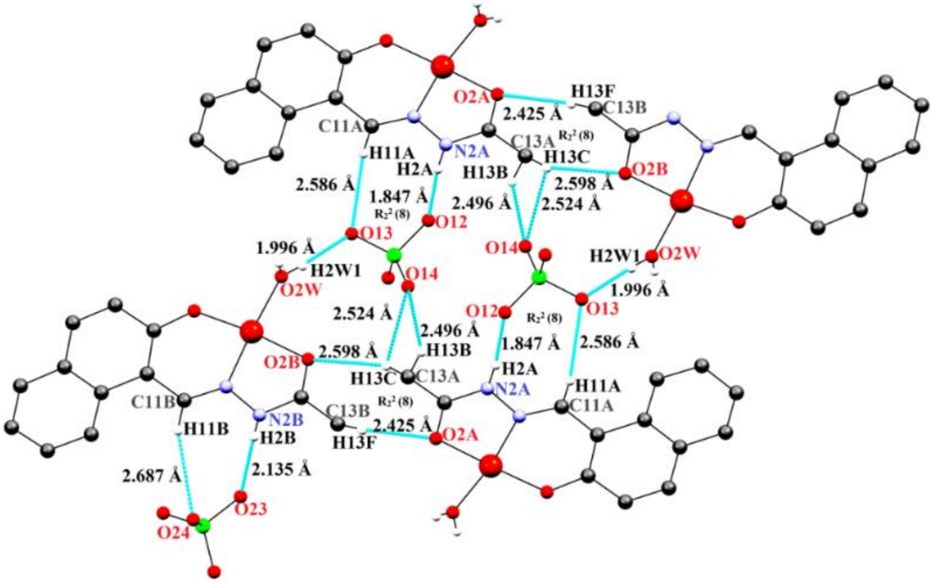

Fig. 19. Hydrogen bonding in complex **1**.

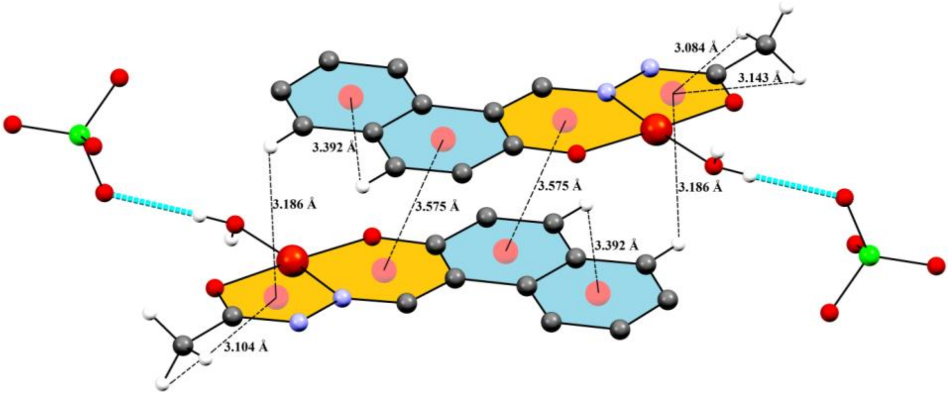

Fig. 20. Centroid Packing diagram of complex **1**.

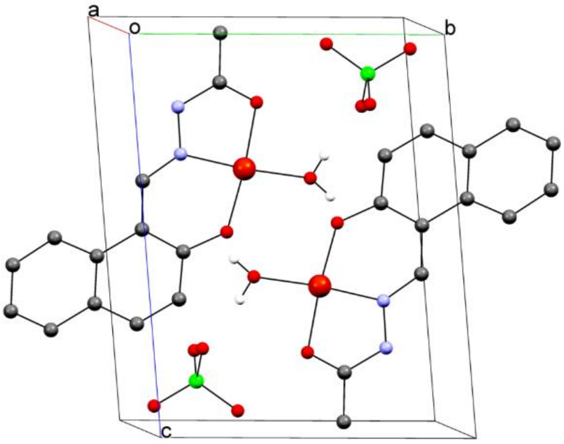

Fig. 21. Packing diagram of complex **1**.

The intermolecular interactions of the coordinate water (O1W-H1W), the CH groups (C2H2) of Schiff base and perchlorate counter anions are also interesting. The O11 and O14 act as H-bond acceptor and forming a heterosynthon motif of $R_4^4(20)$ in complex **2**. Thus, a centrosymmetric dimer is formed by this motif. Similarly, O11 and 013 atoms of bridging perchlorate again connects the adjacent unit by another eight-membered ring motif ($R_2^2(8)$). Similarly, O11 and O13 of perchlorate anions act as H-bond acceptors with third units of the complex having N2H2 and C11H11 donor groups. These donor and acceptor groups lead to the formation of eight-membered $R_2^2(20)$, heterosynthon motif (Fig. 22). Similar to complex **1**, this complex also exhibits several CH···π (aryl and metal chelate) and lone pair, lp···π interactions. The distances of CH···π aryl and metal chelate rings remain in the range of 3.089 Å- 3.414 Å whereas the distance of lp···π (metal chelate) is 3.258 Å (Fig. 23). No π-π stacking interaction is observed in this complex. In this complex interplanar distance is 9.740 Å. The presence of lone pair interaction can afford a degree of stability [87]. The distance of lp···π is similar to the reported distance in literature [88]. Similarly, the presence of CH···π (aryl and metal chelates) sustain the molecular structure in a given dimension. Fig. 24 shows a packing diagram of the unit cell among the b-axis. The CH···π (metal chelate and aryl) with the neighbouring molecules and also intermolecular H-bonding contribute stability to the unit cell packing.

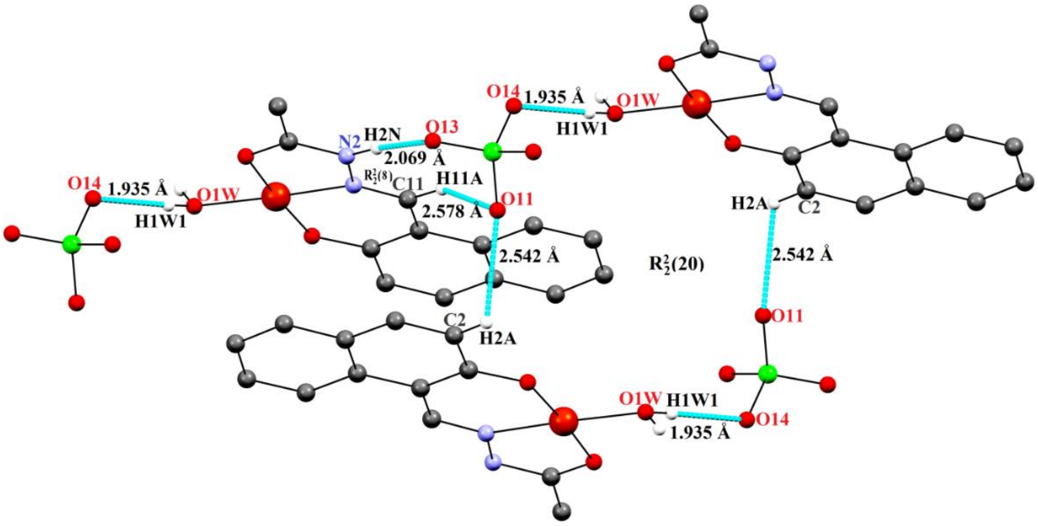

Fig. 22. Hydrogen bonding in complex **2**.

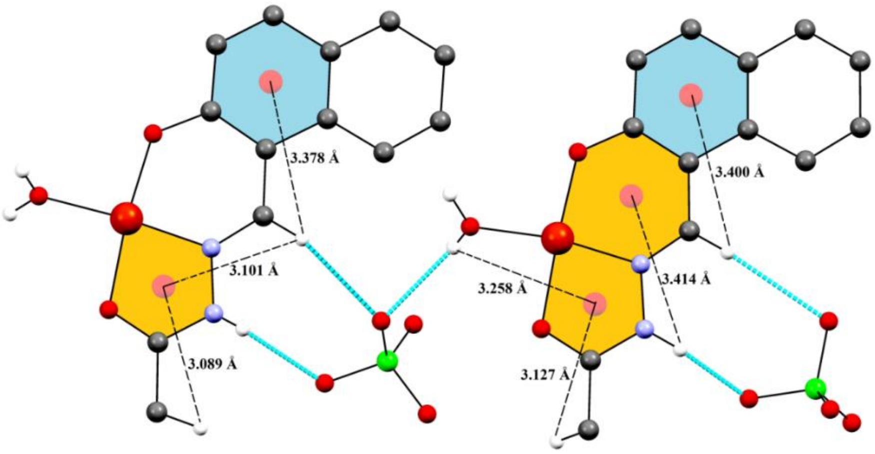

Fig. 23. C-H···π (chelate ring) interactions of complex **2**.

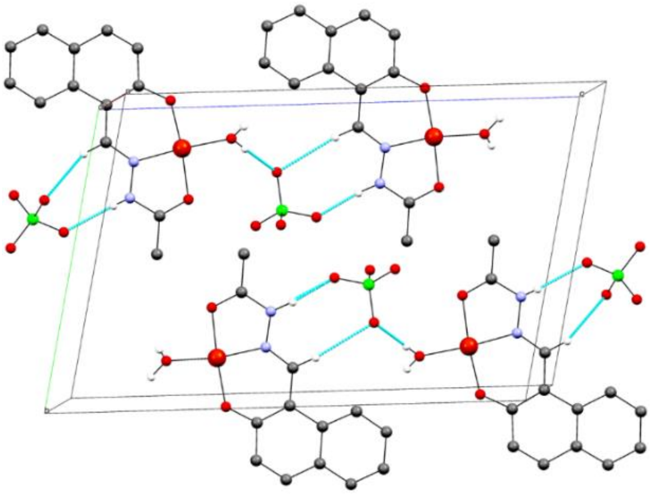

Fig. 24. Packing diagram of complex **2**.

In complex **3**, the crystal lattice is aggregated through various H-bondings (C-H···O, N-H···O and O-H···O), C-H···π (aryl and metal chelates) and π···π (aryl metal chelate) interactions. In this complex **3**, Schiff base (C11 and N2) interact with the (O3 and O5) O atoms of free nitrate anions through N-H···O and CH···O hydrogen bonds (heterosynthon) forming an eight-membered ring motif $R_2^2(8)$. Similarly, two units of complexes centro symmetrically paired through C13-H···O2 hydrogen bonds (homosynthon) involving the acetyl group (C-H) and the O2 (C=N) atom of neighbouring complex molecule to form the ring motif $R_2^2(8)$ (Fig. 25). Besides, one more H-bonding O1W-H···O3 (free nitrate anion) is also observed. The role of such H-bonded supramolecular synthons (motif) is well established in crystal engineering [89, 90]. The two moieties (phenyl and metal chelate rings) of two complexes units show π···π (aryl metal chelate) interactions with distances lp···lp = 3.443 Å. Similarly, in between two metal complex units, two types of C-H···π (aryl and metal chelates) are also observed. The details of these non-covalent interactions with distances are shown in Fig. 26. The packing diagram is also shown in Fig. 27. The hydrogen bonding table for complexes **1-4** are shown in Table 4.

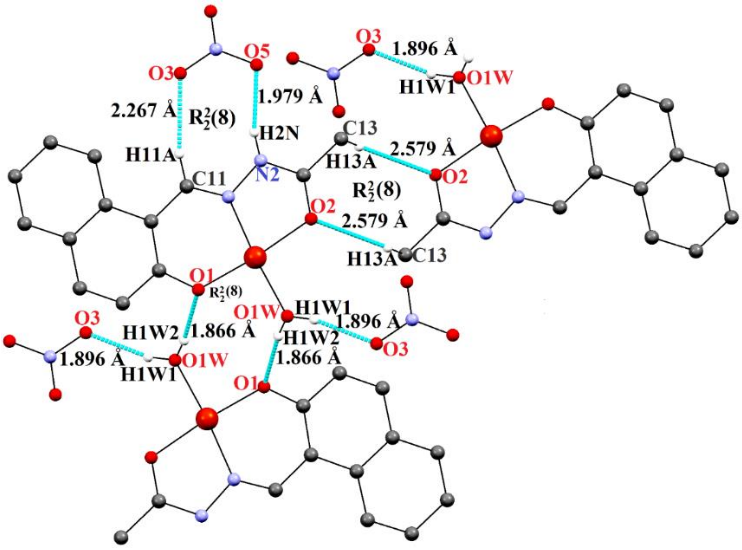

Fig. 25. H-Bonding of complex **3**.

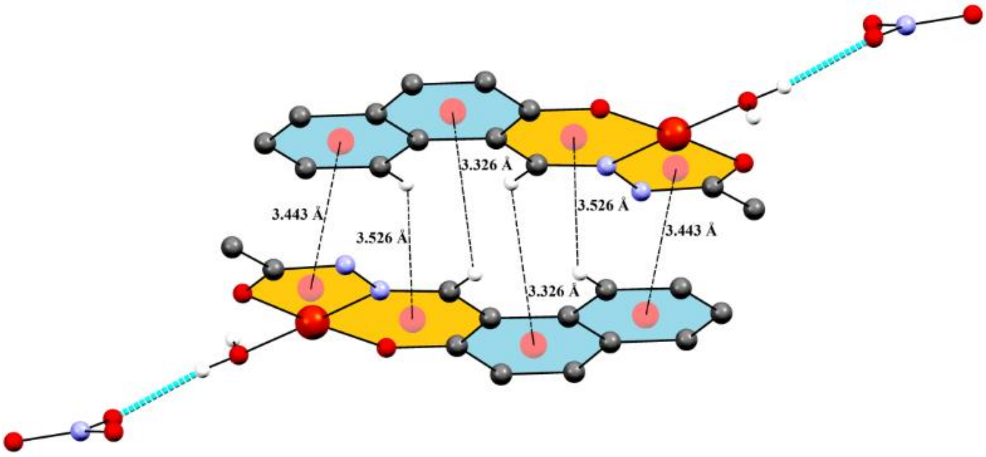

Fig. 26. C-H···π (chelate ring) interactions of complex **3**.

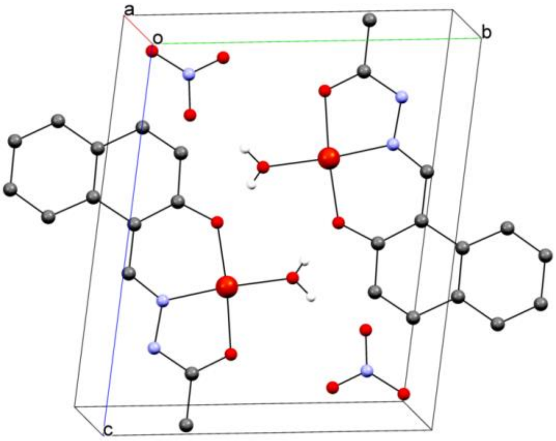

Fig. 27. Packing diagram of complex **3**.

In complex **4** the discrete units are well connected by intermolecular hydrogen bondings. Hydrogen bond donors are C-H and O-H moiety of ligand and water molecules whereas hydrogen bond acceptor atoms are Cl atom and O atom of the bound Schiff base. Water molecule also acts as hydrogen bond acceptor. The oxygen atom of water molecules generates bifurcated hydrogen bonding (Fig. 28). The donor-acceptor distances ($d_{D...A}$) and angles <(DAA) are given in Table 4. These various hydrogen bondings give rise to three-dimensional frameworks. There are also three π···π (aryl-metal) chelate interactions in between two molecules (Fig. 29). These centroid-to-centroid distances ($d_{Cg...Cg}$) are in the range 3.522-3.572 Å. The view of packing along the b-axis along with hydrogen bonding is showing in Fig. 30.

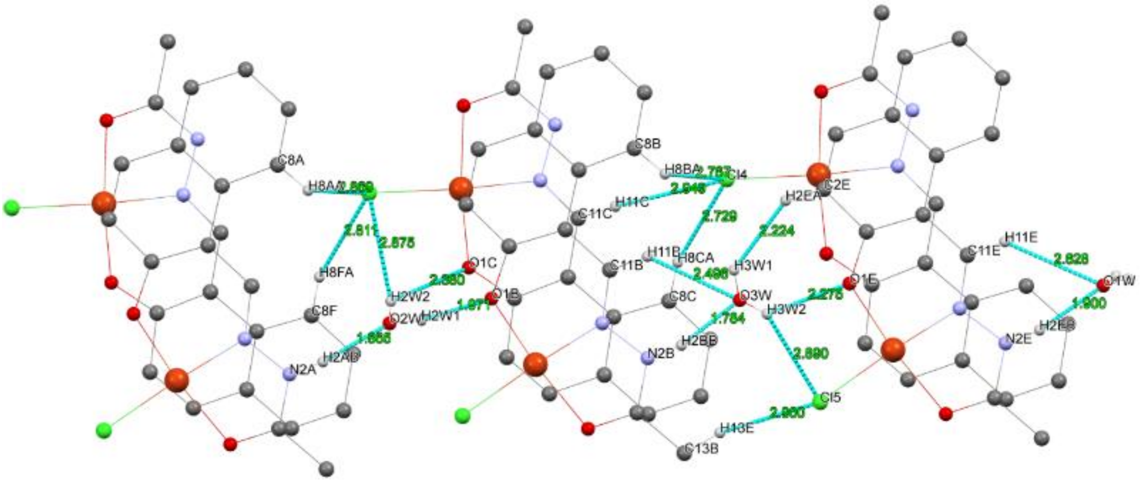

Fig. 28. Hydrogen bonding of complex **4**.

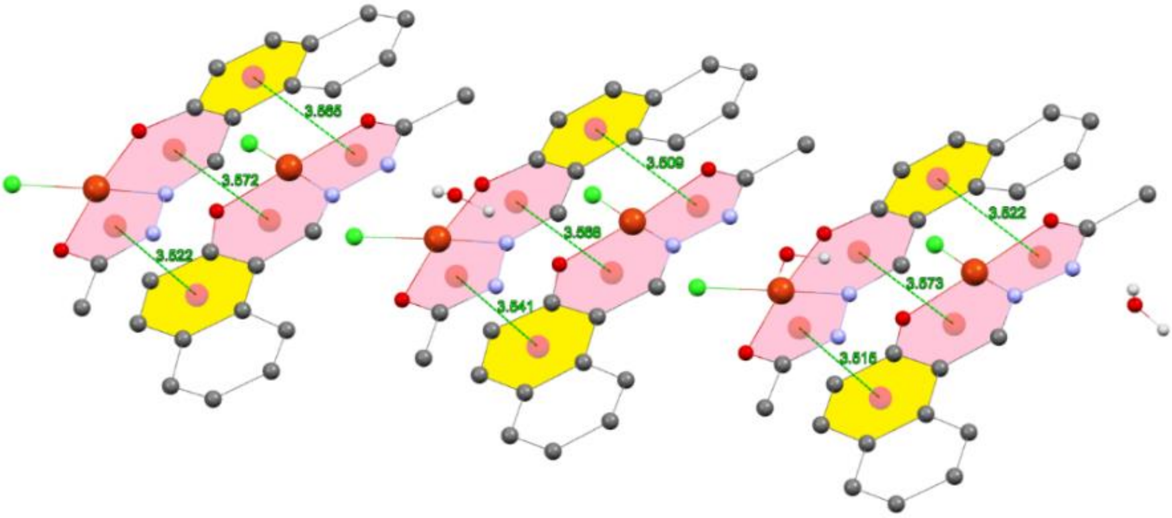

Fig. 29. π ···π (aryl-chelate ring) interactions of complex **4**.

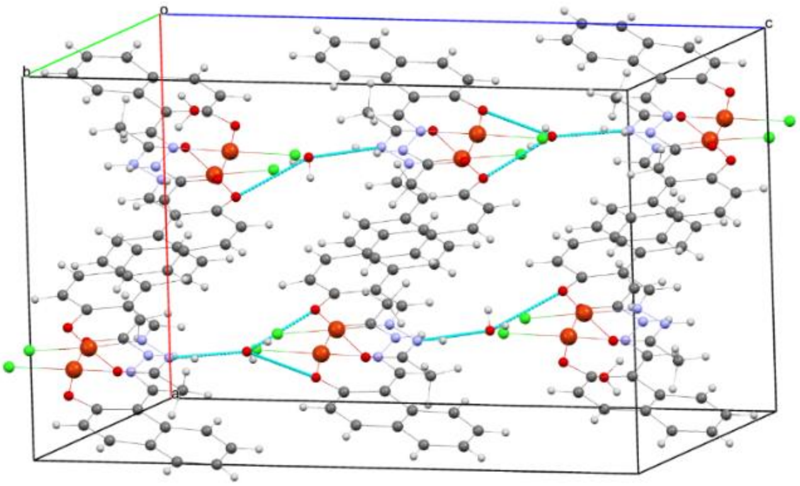

Fig. 30. Packing diagram of complex **4**.

Table 4 Hydrogen bonds of complexes **1-4** [Å and °].

D-H...A	d(D-H)	d(H...A)	d(D...A)	<(DHA)	Symmetry transformations
1					
O(2W)-H(2W1)...O(13)#1	0.76(5)	1.99(6)	2.749(5)	172(6)	#1 -x+1,-y,-z+1
N(2A)-H(2A)...O(12)	0.92(5)	1.84(5)	2.755(6)	172(5)	
C(11A)-H(11A)...O(13)	0.95	2.59	3.522(6)	168.4	
C(11B)-H(11B)...O(24)	0.99	2.69	3.501(6)	148.4	
C(13A)-H(13B)...O(14)#3	0.98	2.50	3.052(6)	115.7	#3 -x,-y+1,z+1
C(13A)-H(13C)...O(2B)#2	0.98	2.60	3.514(6)	155.6	#2 -x+1,-y+1,z+1
C(13A)-H(13C)...O(14)#2	0.98	2.52	3.002(7)	110.4	
N(2B)-H(2B)...O(23)#4	0.70(5)	2.13(5)	2.821(6)	170(7)	#4 -x+1,-y+1,-z
C(13B)-H(13F)...O(2A)#2	0.98	2.42	3.372(6)	164.0	
2					
O(1W)-H(1W1)...O(14^a) #1	0.76(4)	1.93(4)	2.686(4)	169(4)	#1 -x+2,-y+1,-z+1
N(2)-H(2N)...O(13^a)#2	0.85(3)	2.07(3)	2.892(4)	162(3)	#2 x,y+1,z
C(2)-H(2A)...O(11^a)#3	0.95	2.54	3.137(6)	120.8	#3 -x+1,-y+1,-z+1
C(11)-H(11A)...O(11^a)#2	0.95	2.58	3.400(10)	145.1	
3					
O(1W)-H(1W1)...O(3)	0.77(3)	1.90(3)	2.6495(17)	166(3)	
O(1W)-H(1W2)...O(1)#1	0.83(2)	1.86(3)	2.6862(17)	172(2)	#1 -x+1,-y+1,-z+1
N(2)-H(2N)...O(5)#2	0.83(2)	1.98(2)	2.7973(18)	165(2)	#2 x,y+1,z
C(11)-H(11A)...O(3)#2	0.95	2.27	3.1802(19)	161.0	
C(13)-H(13A)...O(2)#3	0.98	2.58	3.468(2)	151.0	#3 -x+1,-y+1,-z
4					

N(2A)-H(2AB)...O(2W)	0.88	1.86	2.733(9)	169.0	
N(2B)-H(2BB)...O(3W)	0.88	1.78	2.638(10)	163.1	
C(11B)-H(11B)...O(3W)	0.95	2.50	3.237(11)	134.9	
C(13B)-H(13E)...Cl(5)	0.98	2.90	3.751(11)	145.9	
N(2E)-H(2EB)...O(1W)	0.88	1.90	2.762(10)	165.9	
C(11E)-H(11E)...O(1W)	0.95	2.63	3.381(11)	136.6	
C(11D)-H(11D)...Cl(6)#1	0.95	2.88	3.758(7)	153.5	#1 x,y-1,z+1
C(13D)-H(13K)...Cl(1)#2	0.98	2.85	3.821(13)	172.9	#2 x,y,z+1
C(11C)-H(11C)...Cl(4)	0.95	2.95	3.774(7)	146.0	
C(11F)-H(11F)...Cl(3)	0.95	2.98	3.777(7)	142.7	
C(13F)-H(13Q)...Cl(2)#3	0.98	2.88	3.850(14)	172.8	#3 x,y+1,z
O(1W)-H(1W1)...Cl(6)#1	0.82(2)	2.99(11)	3.457(10)	119(10)	
O(1W)-H(1W1)...O(1F)#1	0.82(2)	2.23(6)	2.974(11)	152(10)	
O(1W)-H(1W2)...O(1A)#1	0.82(2)	1.97(5)	2.740(10)	156(11)	
O(2W)-H(2W1)...Cl(2)	0.83(2)	2.98(10)	3.443(10)	117(9)	
O(2W)-H(2W1)...O(1B)	0.83(2)	1.97(3)	2.789(10)	168(12)	
O(2W)-H(2W2)...Cl(3)	0.83(2)	2.87(6)	3.617(10)	151(11)	
O(2W)-H(2W2)...O(1C)	0.83(2)	2.37(9)	2.980(10)	131(9)	
O(3W)-H(3W2)...Cl(5)	0.81(2)	2.89(6)	3.631(10)	153(11)	
O(3W)-H(3W2)...O(1E)	0.81(2)	2.28(8)	2.929(11)	137(10)	

3.4.3 Molecular structure description of mixed ligand complexes 5 and 6

The mixed ligand complexes **5** and **6** are isostructural and Ortep structures are shown in Fig. 31 and 32. Crystallographic data and structural refinement details are given in Table 5, while Table 6 summarized the selected bond distances and bond angles of both complexes. The copper ion in complex **5** has a pentacoordinate polyhedron with a geometry that is intermediate between a trigonal pyramid (C_{3v}) and a square based pyramid (C_{4v}), with the base formed by pyridyl nitrogen (N3) of DMPHEN, enolate oxygen (O1), imine nitrogen (N1) and ketonic oxygen (O2) atoms, while the axial position is occupied by pyridyl nitrogen (N4) of DMPHEN co-ligand with slightly larger bond length Cu-N4 (2.282(3) Å. In this complex, the trans-base angles (O1- Cu-O2 = 161.17(13)˚ and N1- Cu-N3 = 170.67(14)˚ correspond to the displacement of Cu center by 0.220 Å from the mean basal plane. For a pentacoordinate metal center, the distortion in the coordination environment from trigonal pyramidal (TBP) to square pyramidal (SP) can be described by the Addison distortion index (τ_5) [84]. The Addison parameter tau (τ) is a degree of trigonality index defined by the equation $\tau_5 = \frac{(\beta - \alpha)}{60}$ (where β and α are first and second-largest angles, respectively) and its value varies from 0 (in regular square pyramidal structure) to 1 (in regular trigonal pyramidal structure). For Penta coordinated complexes, the distortion index (τ) was found to 0.16, respectively. Therefore, the coordination polyhedron of complex **5** is better described as a distorted square base pyramid. Complex **6** is four coordinate having donor sites of ONO of HL and one N of BZI. The distortion in four coordinate geometry is defined by $\tau_4 = 360-(\alpha + \beta)/ 141)$ [91]. The value of $\tau_4$for complex **6** is 0.007 (1 for perfect tetrahedral and 0 for square planar complex). Therefore, geometry around copper(II) is a distorted square planar. The small distortion in the basal plane of each polyhedron may be attributed to the strain imposed by the tridentate Schiff base (HL) to the copper center during metal-ligand coordination. In both complexes, the basal coordination sites are comprised of donor atoms of tridentate Schiff base and mono/bidentate co-ligand. In the basal plane, the bond distances range is 1.916 - 2.019 Å in **5** and 1.9147-1.9694 Å in **6** with the apical site having longer distances of 2.282 Å in **5**. These bond distances and bond angles are agreed very well with those reported in similar copper(II) complexes. [92-94]

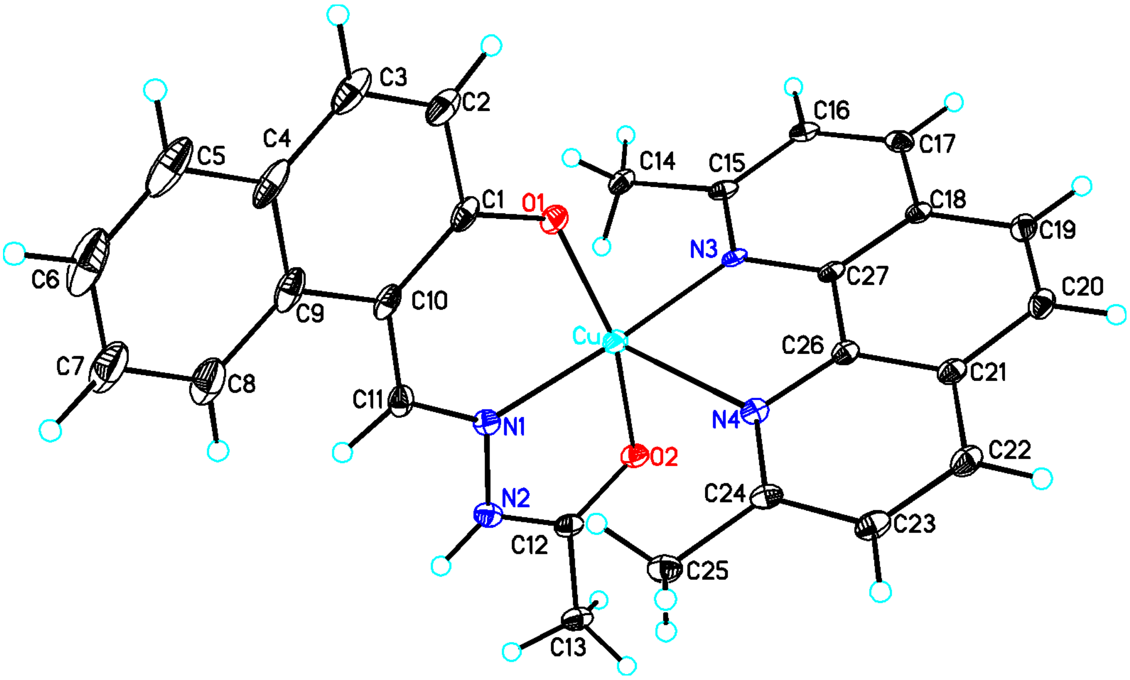

Fig. 31. ORTEP view of complex **5.**

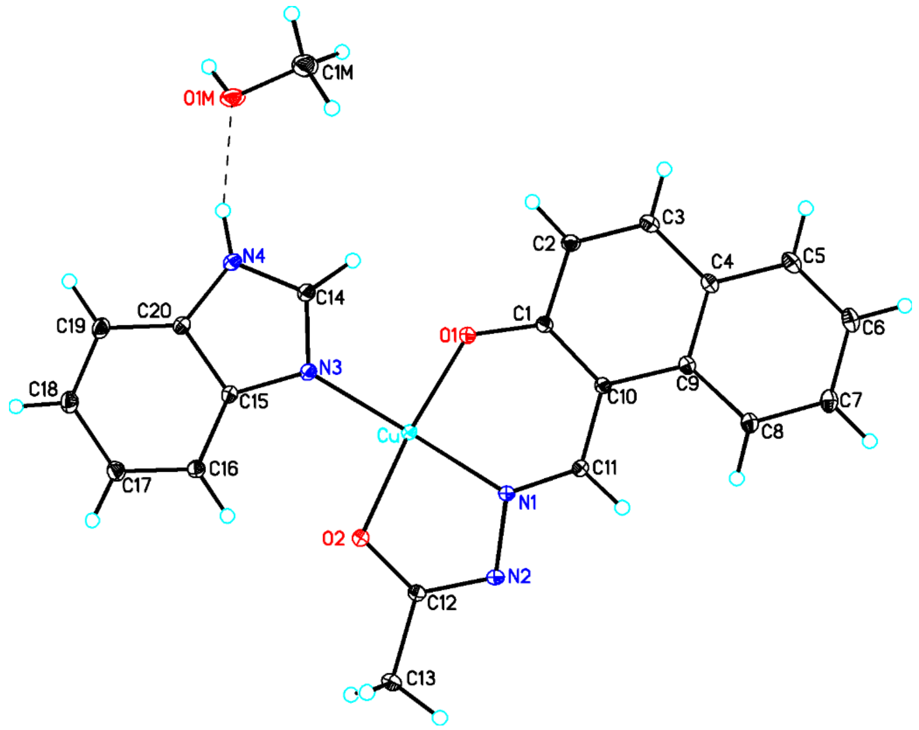

Fig. 32. ORTEP view of complex **6**.

Table 5 Crystal data and structure refinement of mixed ligand complexes **5** and **6**.

	5	6
Empirical formula	$C_{27}H_{23}ClCuN_4O_6$	$C_{21}H_{20}CuN_4 O_3$
Formula weight	598.48	439.95
Temperature (K)	100(2)	100(2)
Wavelength (Å)	0.71073	0.71073
Crystal system	Monoclinic	Monoclinic
Space group	$P2_1/n$	P 21/c
a (Å)	14.3642(14)	10.0749(2)
b (Å)	7.2444(7)	16.9282(3)
c (Å)	24.751(2)	11.5490(2)
α (°)	90	90
β (°)	97.282(3)	104.4080(10)
γ (°)	90	90
Volume (Å^3)	2554.8(4)	1907.73(6)
Z	4	4
Density (calculated) (Mg/m^3)	1.556	1.532
Absorption coefficient (mm^{-1})	1.011	1.176
F(000)	1228	908
Crystal size (mm^3)	0.31 x 0.15 x 0.11	0.18 x 0.16 x 0.08
Theta range for data collection (°)	2.709 to 28.346	2.689 to 34.986

Index ranges	-7<=h<=9, -13<=k<=12, -15<=l<=15	-16<=h<=15, -27<=k<=27, -17<=l<=18
Reflections collected	6368	50945
Independent reflections	6368 [R(int) = 0.0279]	8391 [R(int) = 0.0328]
Completeness to theta = 25.242°	99.9 %	99.9 %
Absorption correction	None	None
Refinement method	Full-matrix least-squares on F^2	Full-matrix least-squares on F^2
Data / restraints / parameters	6368 / 0 / 359	8391 / 0 / 272
Goodness-of-fit on F^2	1.211	1.051
Final R indices [I>2sigma(I)]	R1 = 0.0665, wR2 = 0.1431	R1 = 0.0303, wR2 = 0.0724
R indices (all data)	R1 = 0.0894, wR2 = 0.1524	R1 = 0.0434, wR2 = 0.0804
Extinction coefficient	n/a	n/a
Largest diff. peak and hole (e. Å^{-3})	0.796 and -0.582	0.572 and -0.589

Table 6 Bond lengths [Å] and angles [°] of complexes **5** and **6**.

5					
Bond lengths	**XRD**	**DFT**		**XRD**	**DFT**
Cu(01)-O(1)	1.916(3)	1.915	Cu(01)-O(2)	2.019(3)	2.018
Cu(01)-N(1)	1.933(3)	1.934	Cu(01)-N(4)	2.282(3)	2.282
Cu(01)-N(3)	1.988(3)	1.987			
Bond angles					
O(1)-Cu(01)-N(1)	89.63(14)	89.62	O(1)-Cu(01)-N(4)	108.53(13)	108.52
O(1)-Cu(01)-N(3)	91.95(13)	91.94	N(1)-Cu(01)-N(4)	108.87(13)	108.88
N(1)-Cu(01)-N(3)	170.67(14)	170.67	N(3)-Cu(01)-N(4)	79.31(12)	79.33
O(1)-Cu(01)-O(2)	161.17(13)	161.17	O(2)-Cu(01)-N(4)	89.97(12)	89.98
N(1)-Cu(01)-O(2)	80.83(13)	80.82	N(3)-Cu(01)-O(2)	94.98(12)	94.98
6					
Bond lengths					
Cu-O(1)	1.9038(8)	1.9037	Cu-O(2)	1.9425(8)	1.9426
Cu-N(1)	1.9147(9)	1.9147	Cu-N(3)	1.9694(9)	1.9695
Bond angles					
O(1)-Cu-N(1)	91.46(4)	91.45	O(1)-Cu-N(3)	89.80(4)	89.80
O(1)-Cu-O(2)	171.92(4)	171.93	N(1)-Cu-N(3)	178.64(4)	178.65
N(1)-Cu-O(2)	81.92(4)	81.92	O(2)-Cu-N(3)	96.87(4)	96.88

3.4.4 Supramolecular assembling of complexes 5 and 6

The C(11)-H(11A)...O(4) and N(2)-H(2N)...O(3) of Schiff base form intermolecular hydrogen bondings in complex **5**. The H-bonding table is shown in Table 7. The N2H2N showed bifurcated hydrogen bonding, thus forming $R_3^1(3)$ membered heterosynthons Fig. 33. Similarly, C17H11A showed intramolecular hydrogen bonding and formed $R_2^2(7)$ heterosynthon. In addition to hydrogen bondings, two C-H···π (aryl and metal chelate) interactions, having ring centroid (H···C_g) distances are 3.506 and 3.318 Å respectively Fig. 34. The C-H···π interactions are responsible for extra stabilization in the solid-state.The crystal packing diagram of complex **5** is shown in Fig. 35.

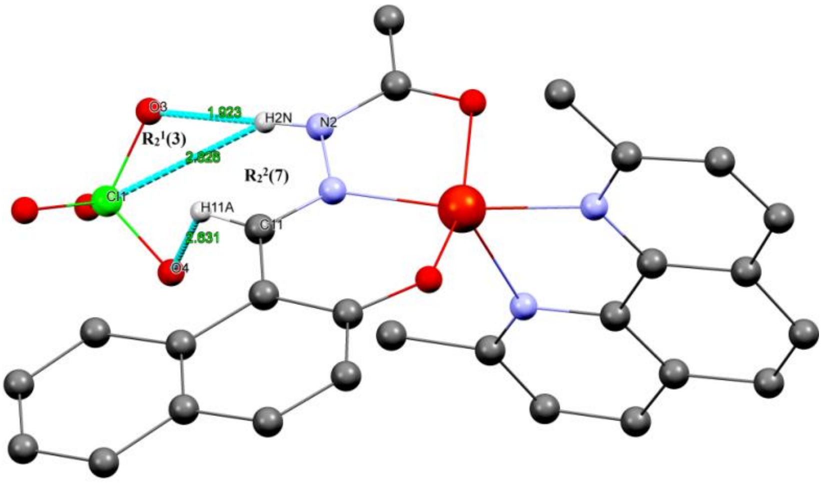

Fig. 33. H-bonding of complex **5.**

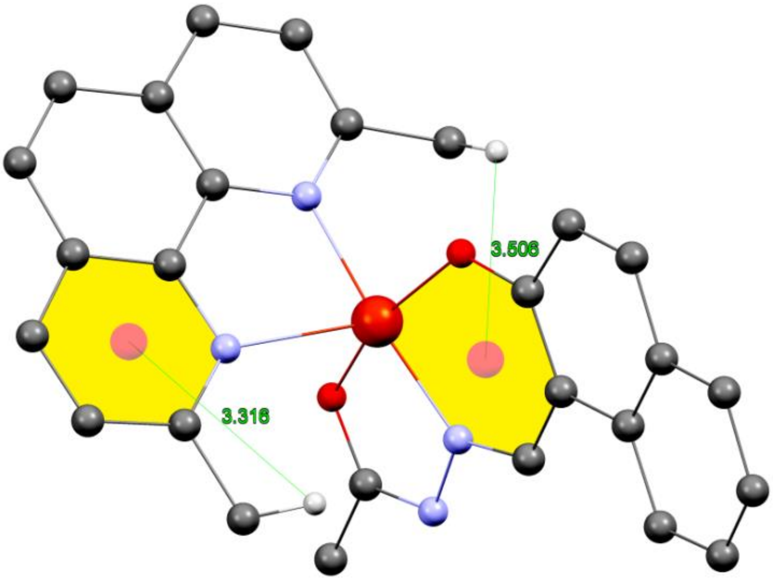

Fig. 34. Centroid diagram of complex **5**.

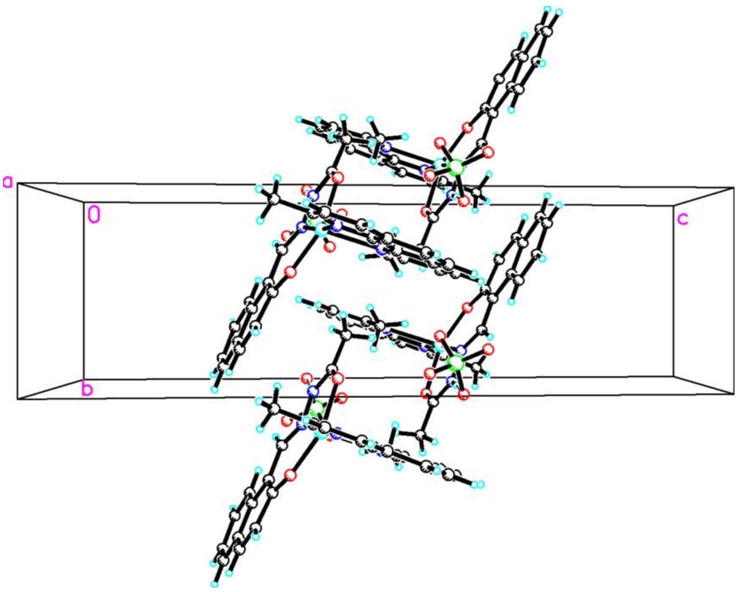

Fig. 35. Crystal view of complex **5**.

In complex **6** there are two intermolecular hydrogen bondings. The interesting features of the structure are the formation of a supramolecular network through hydrogen bondings interactions in between methanol and complex molecule. The solvent molecule (CH_3OH) forms asymmetric hydrogen bonds (N(4)-H (4N)···O(1M) and O(1M)-H (1M)···N(2)) leading to the formation of the dimer Fig. 36. The two monomeric units also show π···π stacking (chelate-chelate) interactions with a centroid-centroid distances ($d_{Cg\cdots Cg}$) 3.171Å Fig. 37. The π···π and hydrogen bonding interactions, furnish extra stabilization to the solid-state. The crystal packing diagram of complex **6** is shown in Fig. 38. The H-bonding table is shown in Table 7.

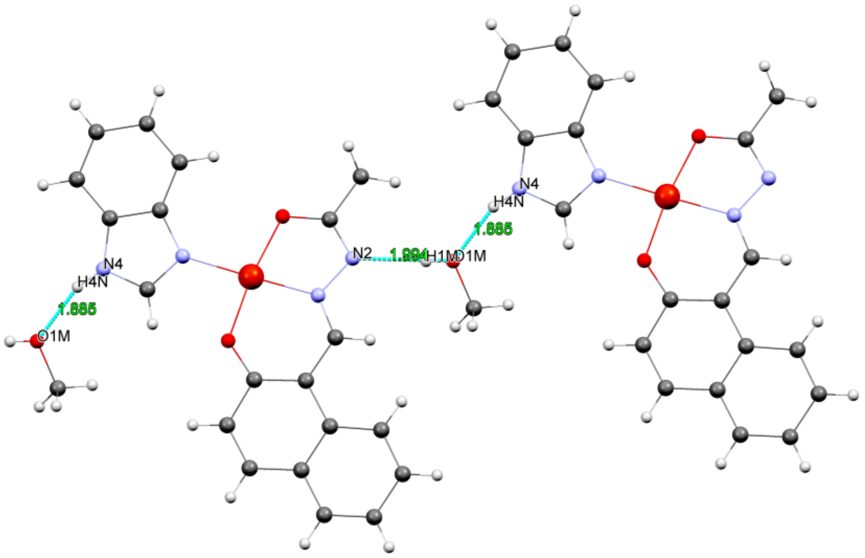

Fig. 36. H-bonding interaction in complex **6**.

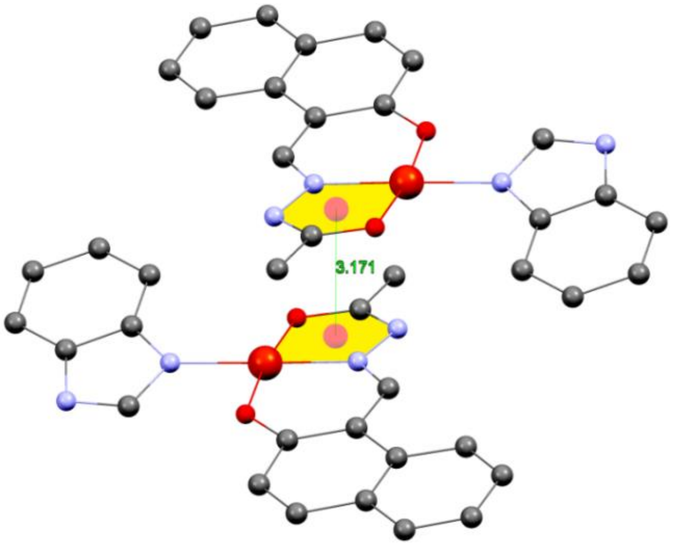

Fig. 37. Stacking interaction in complex **6.**

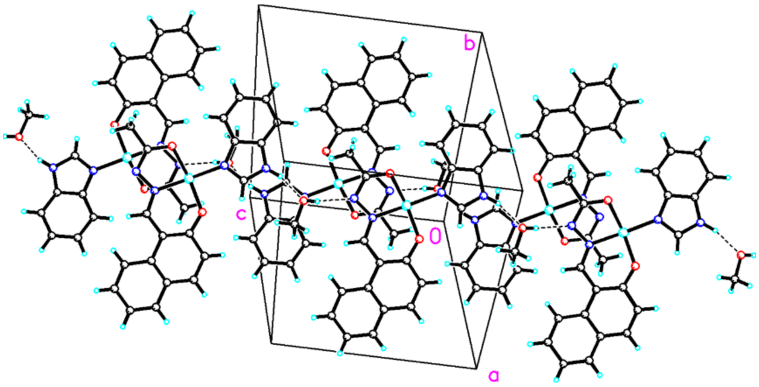

Fig. 38. Crystal view of complex **6**.

Table 7 Hydrogen bonds of complexes **5** and **6** [Å and °].

D-H...A	d(D-H)	d(H...A)	d(D...A)	<(DHA)	Symmetry transformations
1					
N(2)-H(2N)...Cl(1)	0.90(5)	2.83(5)	3.642(4)	152(4)	1 -x+1,-y,-z+1
N(2)-H(2N)...O(3)	0.90(5)	1.92(5)	2.819(5)	178(5)	
C(11)-H(11A)...O(4)	0.95	2.63	3.122(5)	112.6	
C(25)-H(25A)...N(1)	0.98	2.59	3.436(6)	145.2	
2					
C(14)-H(14A)...O(1)	0.95	2.30	2.7868(14)	111.0	1 -x,-y,z-1
C(16)-H(16A)...O(2)	0.95	2.49	3.1544(14)	127.4	1 -x,-y,z-1
O(1M)-H(1M)...N(2)#1	0.75(3)	1.99(3)	2.7394(14)	171(3)	1 -x,-y,z-1
N(4)-H(4N)...O(1M)	0.86(2)	1.89(2)	2.7182(14)	160.7(19)	1 -x,-y,z-1

3.4.5 Molecular structures of binuclear complexes 7, 8 and 9

All these three binuclear complexes contain two copper atoms in the symmetric unit with the molecular formula $[Cu(HL)(\mu\text{-}ClO_4)(L).2H_2O]$ **7,** $[(HL)Cu(\mu\text{-}SO_4)Cu(HL)]$ **8,** $[(HL)Cu(\mu\text{-}bpm)Cu(HL)]ClO_4.3H_2O$ **9.** In these binuclear complexes (**7-9**) each copper atom has a pentacoordinated (N, O in **7** and **8**, N, O in **9**) environment thus forming a $[Cu_2(\mu\text{-}SO_4/\text{-}ClO_4/\text{-}bpm)]$ core unit (Fig. 39-41). The angles of these complexes at Cu1 between the cis-positioned donor pairs span the range ~78.2-103º and those between the trans-positioned pairs span in the range 155-166º. The crystal table along with the bond length and angles is shown in Tables 8 and 9. The binuclear complexes **7** and **8** are isostructural. The **7** and **8** dimmers have crystallographically imposed C_2 symmetry that describes two monomeric halves of complexes. The core of these complexes constitutes $[Cu_2(\mu\text{-}ClO_4/SO_4)_2]$ unit, which has bond distances of ~1.9, 2.1 for $\mu\text{-}ClO_4^{2-}$ and 1.92, 2.7 for $\mu\text{-}SO_4^{2-}$ respectively.

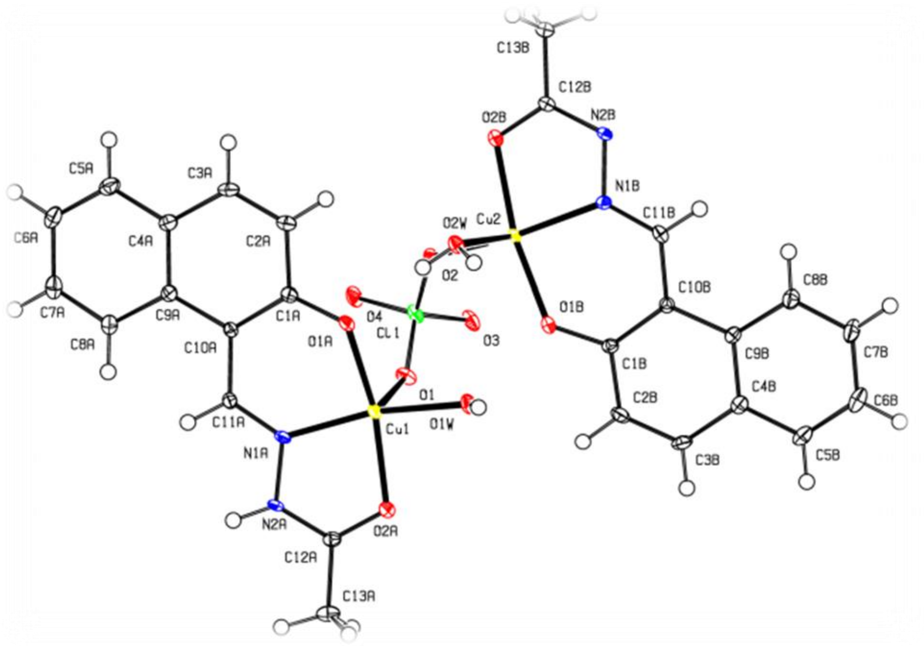

Fig. 39. ORTEP view of complex **7.**

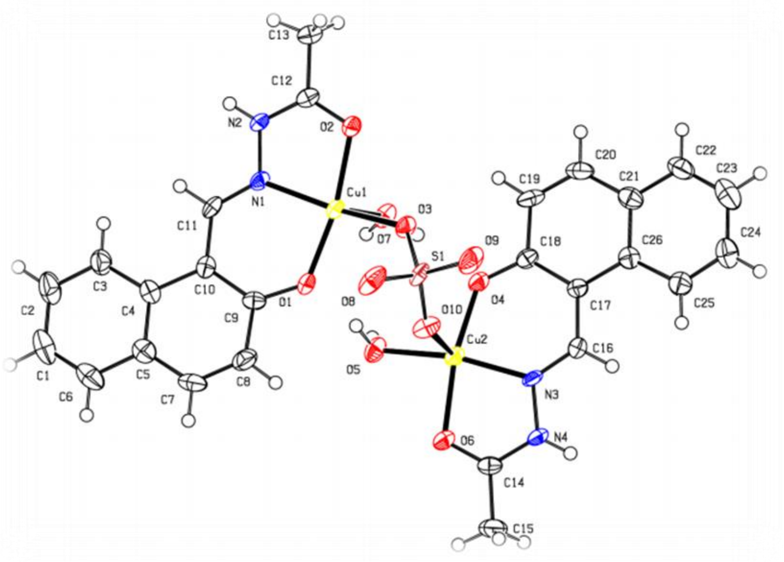

Fig. 40. ORTEP view of complex **8.**

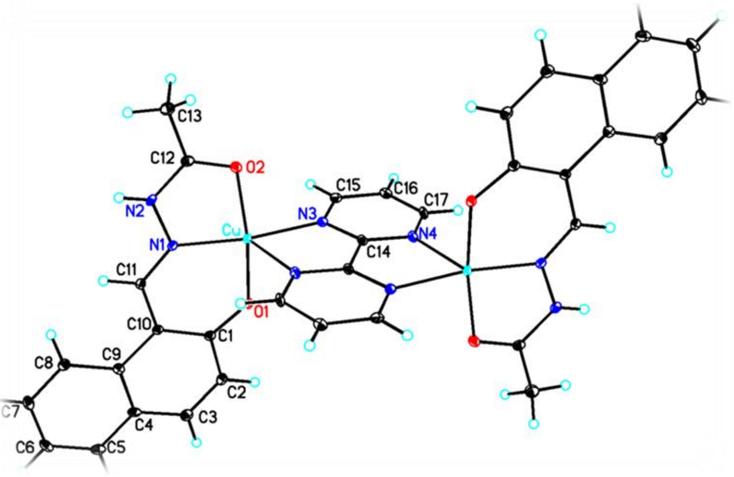

Fig. 41. ORTEP view of complex **9.**

The Cu-Cu distances in these complexes are 4.578 Å for **7** and 4.581 Å for **8**. The µ-ClO_4^{2-}/ SO_4^{2-} ligands can be illustrated as bridging in a basal-apical fashion, i.e., one oxygen of each bridging ligand occupies a basal site of one copper center with oxygen occupying the apical site of the second copper center. $[Cu_2(\mu\text{-}ClO_4/SO_4)_2]$ unit maintains the W-shaped conformation in which the legating oxygen atoms illustrate a plane that lies below the plane illustrated by the copper and chlorine or sulphur atoms. Such types of complexes have already been reported [95]. The basal plane of complexes **7** and **8** consists of three donor atoms (O1A, O2A and N1A) of Schiff base (HL) together with one atom of bridging perchlorate or sulphate oxygen atoms (O1, O2)at 1.984 and 2.293 Å from the Cu(II) atom in molecule 7A and 7B, respectively. Similar binding pattern found in **8** with sulphate bridging unit. In complexes **7** and **8** each copper atom is connected through a perchlorate or sulphate group bridging in an end-to-end fashion, respectively.

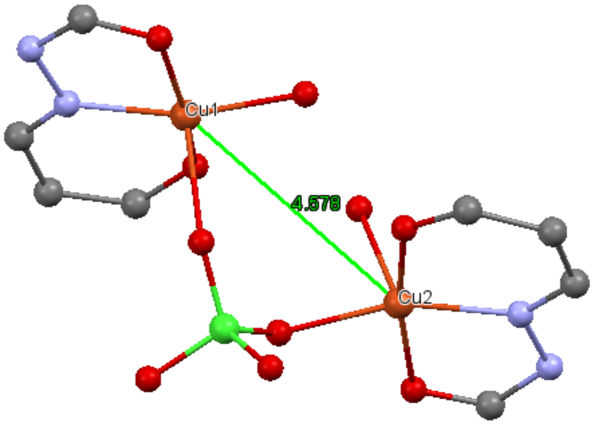

Fig. 42. Cu-Cu distance in complex **7**.

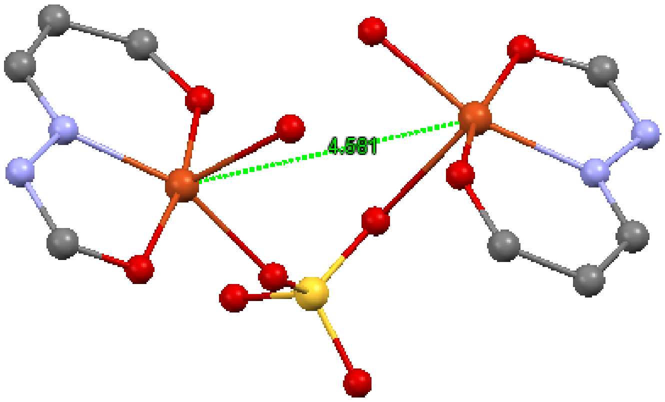

Fig. 43. Cu-Cu distance in complex **8**.

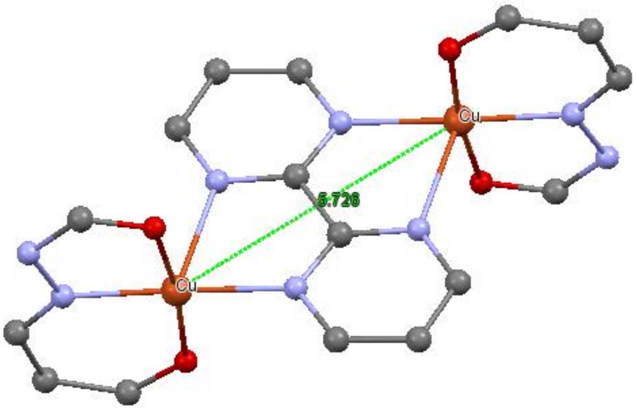

Fig. 44. Cu-Cu distance in complex **9**.

The structure of **9** is µ-pyramidine bridged complex. The basal plane of this complex comprises three donor atoms of HL O1, O2 and N1 and one nitrogen atom (N3) of bpm for both metal centres. All three binuclear complexes **7**, **8** and**9** have C_i symmetry, the centre of symmetry being located at the centre of the bridging molecule. Thus, the (L) Cu fragments are in transpositions with Cu(II)-Cu(II) distance of 5.726 Å respectively (Fig. 42-44). The copper(II) centres in these complexes exhibit distorted square pyramidal geometries (τ = 0.004, 0.178 and 0.013 for **7**, **8** and **9** respectively) for the O_4N (in **7** and **8**) and O_2N_3 donor set in **9**. As usual, the copper ions are displaced up from the mean basal plane toward the apically coordinated atoms by 0.226, 0.243 and 0.319 Å for **7**, **8** and **9** respectively. The bond lengths and bond angles of these complexes are in agreement with those reported for similar copper(II) complexes [80].

Table 8 Crystal data and structure refinement of complexes **7, 8** and **9**.

	7	8	9
Empirical formula	$C_{26}H_{25}ClCu_2N_4O_{10}$	$C_{26}H_{26}Cu_2N_4O_{10}S$	$C_{34}H_{33}ClCu_2N_8O_{11}$
Formula weight	716.03	713.65	829.23
Temperature (K)	100.0	293(2)	100(2) K
Wavelength (Å)	0.71073	0.71073	0.71073
Crystal system	Monoclinic	Monoclinic	Monoclinic
Space group	Cc	Cc	P 21/c
a (Å)	9.2106(2)	9.2020(5)	10.6175(5) Å
b (Å)	23.2111(5)	23.3430(14)	23.4076(6) Å
c (Å)	12.8350(3)	12.9312(8)	13.4434(6) Å
α (°)	90.00	90.00	90
β (°)	103.6630(10)	103.307(6)	109.401(2)°
γ (°)	90.00	90.00	90
Volume (Å^{3})	2666.32(10)	2703.1(3)	2074.33(16)
Z	4	4	4
Density (calculated) (Mg/m^{3})	1.784	1.754	1.633
Absorption coefficient (mm^{-1})	1.764	1.718	1.236
F(000)	1456.0	1456.0	1042
Crystal size (mm^{3})	0.220 x 0.180 x 0.167	0.220 x 0.170 x 0.120	0.220 x 0.180 x 0.110
Theta range for data collection (°)	4.8 to 66.74	6.94 to 58.54	2.644 to 28.310
Index ranges	-14 ≤ h ≤ 14, -35 ≤ k ≤ 34, -19 ≤ l ≤ 18	-11 ≤ h ≤ 12, -29 ≤ k ≤ 31, -16 ≤ l ≤ 17	-14<=h<=14, -20<=k<=20, -17<=l<=17

Reflections collected	31306	15140	29206
Independent reflections	9235 [R_{int} = 0.0456, R_{sigma} = 0.0574]	6212 [R_{int} = 0.0420, R_{sigma} = 0.0583]	9145 [R(int) = 0.0656]
Completeness to theta = 25.242°	99.2 %	99.2 %	99.2 %
Absorption correction	None	None	Semi-empirical from equivalents
Refinement method	Full-matrix least-squares on F^2	Full-matrix least-squares on F^2	Full-matrix least-squares on F^2
Data / restraints / parameters	9235/2/392	6212/2/392	5145 / 10 / 316
Goodness-of-fit on F^2	1.015	1.051	1.122
Final R indices [I>2sigma(I)]	R_1 = 0.0305, wR_2 = 0.0735	R_1 = 0.0396, wR_2 = 0.0729	R1 = 0.0551, wR2 = 0.0884
R indices (all data)	R_1 = 0.0342, wR_2 = 0.0752	R_1 = 0.0507, wR_2 = 0.0795	R1 = 0.0802, wR2 = 0.0974
Extinction coefficient	n/a	n/a	n/a
Largest diff. peak and hole (e. Å^{-3})	0.61/-0.62	0.34/-0.42	0.622 /-0.748

Table 9 Bond lengths [Å] and angles [°] of complexes **7-9**.

7					
Bond lengths					
	XRD	**DFT**		**XRD**	**DFT**
Cu1-O1	2.2932(15)	2.2947	Cu2-O2	1.9841(13)	1.9842
Cu1-O1W	1.9553(15)	1.5954	Cu2-O2W	2.2059(15)	2.2054
Cu1-O1A	1.9139(16)	1.9137	Cu2-O1B	1.9006(16)	1.9001
Cu1-O2A	2.0021 (16)	2.0024	Cu2-O2B	1.9920(16)	1.9920
Cu1-N1A	1.9241(18)	1.9241	Cu2-N1B	1.9419(18)	1.9418
Bond angles					
O1W-Cu1-O1	88.44(6)	88.45	O2-Cu2-O2W	87.51(6)	87.52
O1W-Cu1-O2A	88.71(6)	88.72	O2-Cu2-O2B	91.43(6)	91.42
O1A-Cu1-O1	91.86(6)	91.87	O1B-Cu2-O2	96.19(6)	96.18
O1A-Cu1-O1W	98.22(6)	98.22	O1B-Cu2-O2W	96.32(6)	96.32

O1A-Cu1-O2A	164.81(6)	164.81	O1B-Cu2-O2B	169.34(6)	169.34
O1A-Cu1-N1A	89.27(7)	89.28	O1B-Cu2-N1B	89.31(7)	89.30
O2A-Cu1-O1	101.87(6)	101.87	O2B-Cu2-O2W	91.43(6)	91.42
N1A-Cu1-O1	104.88(6)	104.89	N1B-Cu2-O2	159.44(7)	159.45
N1A-Cu1-O1W	164.55(7)	164.57	N1B-Cu2-O2W	111.63(6)	111.62
N1A-Cu1-O2A	81.01(7)	81.00	N1B-Cu2-O2B	81.01(7)	81.00
8					
Bond lengths					
Cu-O2	1.996(3)	1.997	Cu2-O5	1.964(3)	1.963
Cu-O7	2.231(3)	2.230	Cu2-O10	2.304(3)	2.302
Cu-O1	1.897(3)	1.897	Cu2-o6	2.007(3)	2.006
Cu-O3	1.981(2)	1.982	Cu2-O4	1.908(3)	1.908
Cu1-N1	1.935(3)	1.934	Cu2-N3	1.919(3)	1.918
Bond angles					
O2-Cu1-O7	90.30(10)	90.30(10)	O5-Cu2-O10	87.99(11)	87.90
O1-Cu1-O2	169.79(10)	169.79(10)	O5-Cu2-O6	88.82(11)	88.80
O1-Cu1-O3	96.31(11)	96.31(11)	O4-Cu2-O5	98.09(11)	98.08
O1-Cu1-N1	89.35(12)	89.35(12)	O4-Cu2-O10	92.04(11)	92.05
O3-Cu1-O2	91.42(10)	91.42(10)	O5-Cu2-O6	88.82(11)	88.81
O3-Cu1-O7	88.12(10)	88.12(10)	O4-Cu2-O3	89.16(12)	89.16
N1-Cu1-O7	81.12(12)	81.12(12)	N3-Cu2-O5	164.16(12)	164.17
N1-Cu1-O7	111.26(11)	111.26(11)	N3-Cu2-O10	105.89(12)	105.89
N1-Cu1-O3	159.11(12)	159.11(12)	N3-Cu2-O6	81.17(12)	81.17
9					
Bond lengths					
Cu-N(1)	1.913(3)	1.913	Cu-N(3)	2.022(3)	2.021
Cu-O(1)	1.914(2)	1.912	Cu-N(4)#1	2.287(3)	2.286
Cu-O(2)	1.974(2)	1.972			

Bond angles					
N(1)-Cu-O(1)	91.25(10)	91.25	O(2)-Cu-N(3)	92.28(10)	92.27
N(1)-Cu-O(2)	82.32(10)	82.32	N(1)-Cu-N(4)#1	108.54(10)	108.51
O(1)-Cu-O(2)	171.43(9)	171.43	O(1)-Cu-N(4)#1	93.19(9)	93.18
N(1)-Cu-N(3)	172.20(10)	172.20	O(2)-Cu-N(4)#1	94.22(9)	94.20
O(1)-Cu-N(3)	93.54(10)	93.54	N(3)-Cu-N(4)#1	77.35(10)	77.35
C(1)-O(1)-Cu	127.7(2)	127.70	C(11)-N(1)-Cu	130.2(2)	130.20
C(12)-O(2)-Cu	111.2(2)	111.20	N(2)-N(1)-Cu	110.98(19)	110.97
C(14)-N(3)-Cu	118.0(2)	118.01	C(14)-N(4)-Cu#1	109.9(2)	109.90
C(15)-N(3)-Cu	125.5(2)	125.50	C(17)-N(4)-Cu#1	132.7(2)	132.70

3.4.6 Supramolecular assembling binary complexes 7-9

In complex **7** the bound water molecule behaves as a hydrogen bond donor towards the oxygen atom of naphthyl moiety of the HL ligand resulting in a formation of intramolecular hydrogen bonding (d_{HA} = 0.790 Å) while bridging the perchlorate ion oxygen atom (O_3) acts as hydrogen bond acceptor towards the N2A-H2A moiety of the HL ligand resulting in the formation of a supramolecular network Fig. 45. Besides this hydrogen bonding interaction there weak π···π (chelate–chelate) interactions in a slipped pattern among the four chelate ring with centroid-centroid distances ($d_{Cg\cdots Cg}$) 3.379 and 3.590 **Å** Fig. 46. A different interaction between a coordinated water molecule and [90] a chelate ring (ln···π) has been observed by single-crystal X-ray analysis. One oxygen atom of coordinated water forms a weak intramolecular interaction with π-electron of a metal chelate ring (ln···π) with a distance of 3.374 **Å** [88, 97]. Intermolecular π···π (metal chelate-metal chelate) and O-H···π (ln···π) interactions lead to the tight packing of four units of complexes in the unit cell Fig. 47.

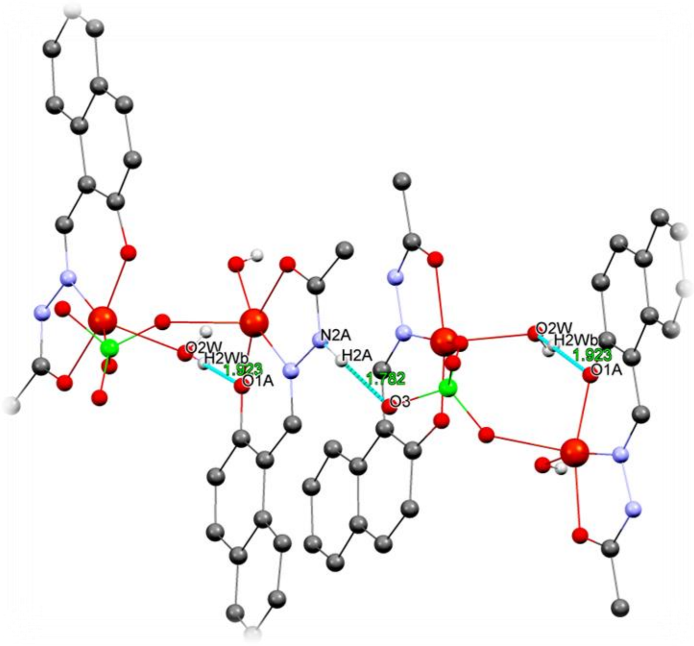

Fig. 45. Hydrogen bonding of complex **7.**

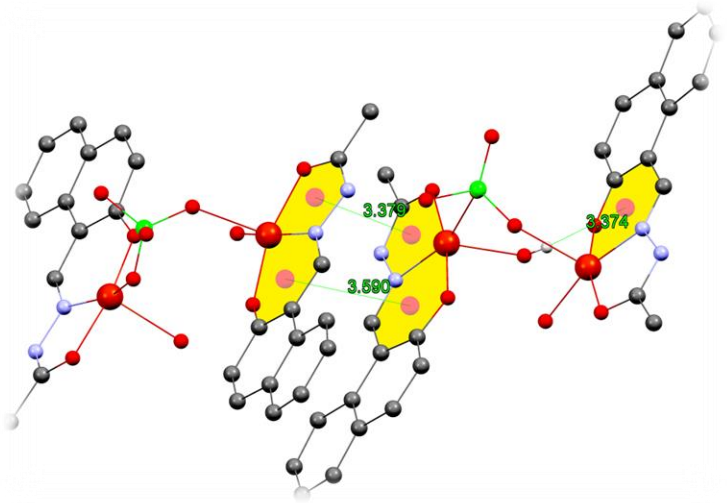

Fig. 46. Stacking interaction in complex **7.**

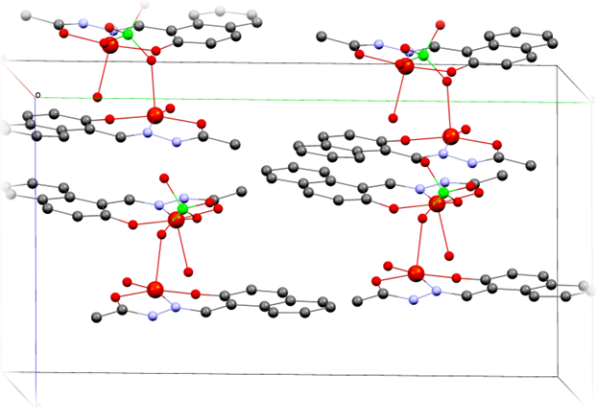

Fig. 47. Packing diagram in complex **7.**

In this complex **8** oxygen atoms (O3 and O6) of bridging perchlorate act as H-bond acceptors and C19, N21 and C11 act as H-bond donors. The oxygen atoms (O43 and O8) of coordinated water molecules also play the role of hydrogen bond donor and imino nitrogen and phenolic atoms (N42 and O25) act as hydrogen bond acceptors. The O3 atom of the bridging atom showed bifurcated interactions and hence forming one $R_2^1(7)$ membered heterosynthons (Fig. 48. The interesting features of the structure are the formation of a supramolecular assembly through H-bonding interactions coordinated water molecule and bridging perchlorate anion. The hydrogen atom of coordinated water molecule involved in O-H$\cdots\pi$ interaction. The stacking of aryl metal chelate rings seen with centroid-centroid distance ($d_{Cg\cdots Cg}$) at 3.415 Å. The stacking of aryl-aryl planar rings is also observed with a centroid –centroid distance ($d_{Cg\cdots Cg}$) at 3.561 Å [98, 99] (Fig. 49). The involved hydrogen bonding, OH$\cdots\pi$ and $\pi\cdots\pi$ interactions, enrich extra stabilization to the solid-state. A stereoscopic projection of the molecular arrangement within the unit cell along c-axis is shown in Fig. 50. In this packing diagram, dimer units constitute a 1D motif.

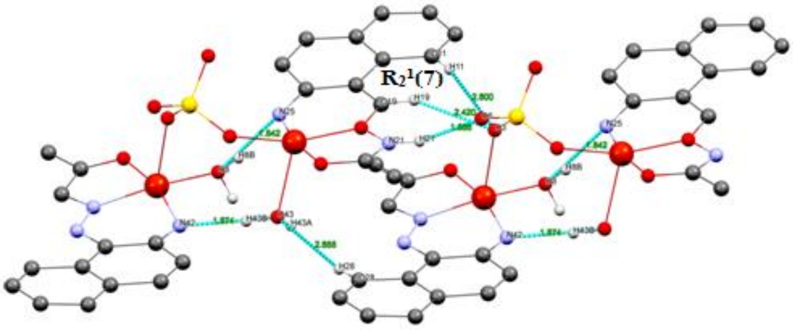

Fig. 48. Hydrogen bonding of complex **8.**

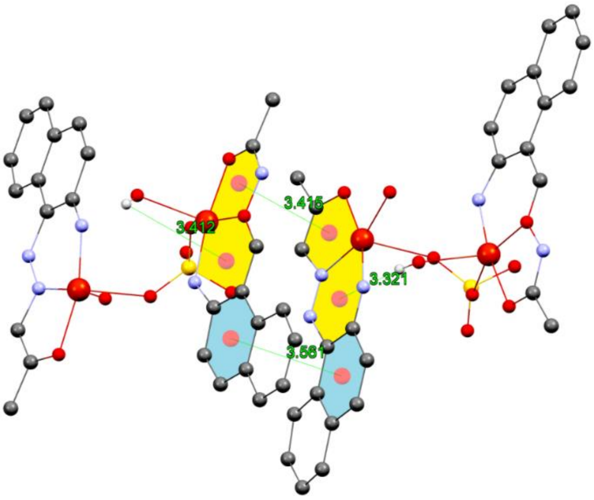

Fig. 49. Stacking interaction in complex **8.**

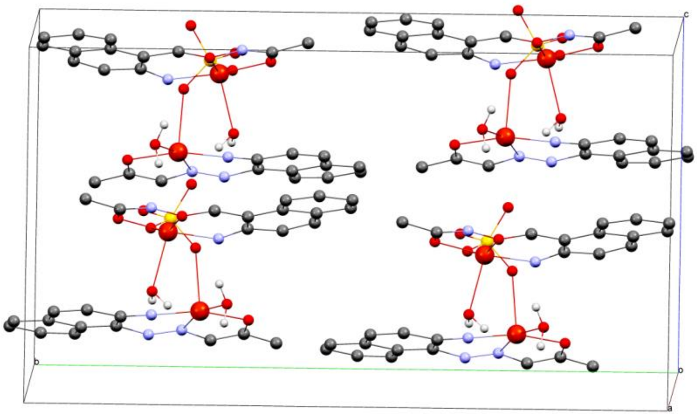

Fig. 50. Packing diagram in complex **8.**

In complex **9** three uncoordinated water molecule and perchlorate anion generates several H-bonding interactions Fig. 51. The two oxygen atoms (O12 and O13) act as an H-bond acceptor. The H-bond donor atoms oxygen atom of crystalline water and carbon atoms (C17) of bridging 2,2-bipyrimidine molecule. Apart from these H-bonding interactions, the crystalline water molecule from other H-bondings is shown in Fig. 52. This molecule is also established due to the presence of another type of interactions like C-H···π (aryl and metal chelate) interactions. A pair of aromatic stacking were seen between phenyl rings of one Cu unit with chelate rings of neighbouring complex with a centroid-centroid distance ($d_{Cg\cdots Cg}$) at 3.420 Å [98]. In this complex intermolecular, π···π and C-H···π interactions of various moieties lead to the tight packing with water and ionic perchlorate molecules in a distinctive channel. The packing diagram of this binuclear complex along the a-axis is shown in Fig. 53. The hydrogen bonding of complexes **7-9** is shown in Table 10.

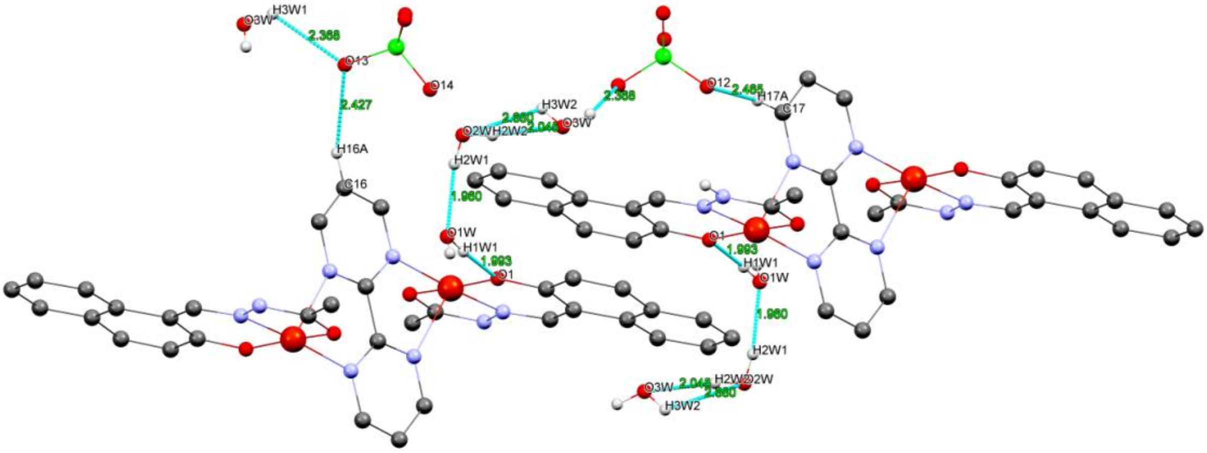

Fig. 51. Hydrogen bonding of complex **9.**

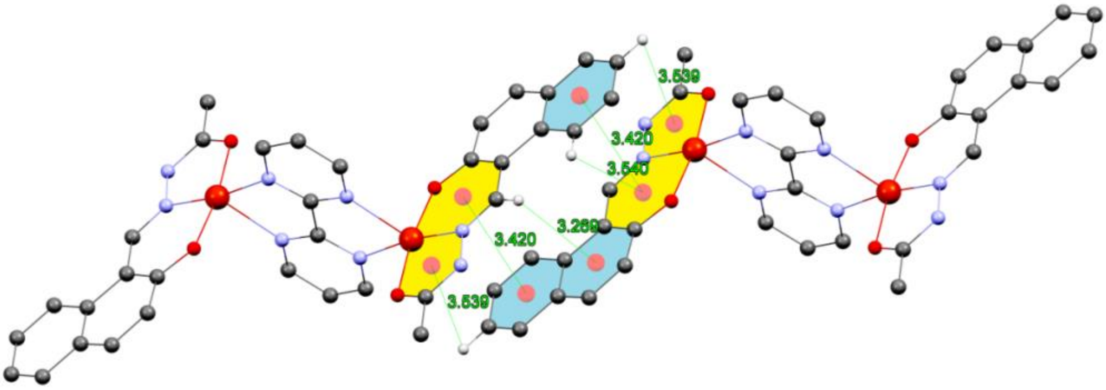

Fig. 52. Stacking interaction in complex **9.**

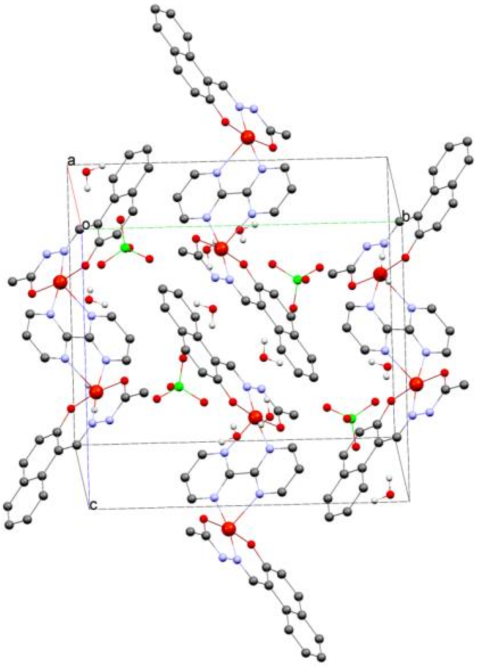

Fig. 53. Packing diagram in complex **9.**

Table 10 Hydrogen bonds of complexes **7-9** [Å and °].

D-H...A	d(D-H)	d(H...A)	d(D...A)	<(DHA)	Symmetry transformations
7					
O1W-H1WA...O4^{1}	0.88	1.93	2.778(2)	159.1	1/2+X
O2W-H2WA...O1A	0.88	1.85	2.733(2)	175.0	
C11A-H11A...O3^{2}	0.95	2.53	3.263(3)	134.1	1/2-Y,1/2+Z
C12A-H13C...O2B^{2}	0.98	2.87	3.171(3)	98.9	-1/2+X,1/2-Y,
C11B-H11B...O1^{3}	0.95	2.37	3.254(3)	154.4	1/2+Z, 1+X,+Y,+Z

9					
N(2)-H(2N)...O(2W)	0.81(4)	1.93(4)	2.731(4)	178(4)	#1 -x+1,-y+1,-z
C(16)-H(16A)...O(13)#2	0.95	2.43	3.322(4)	156.8	#2 -x+1,y-1/2,-z+1/2
C(17)-H(17A)...O(12)#1	0.95	2.46	3.378(4)	161.1	#3 x-1,y,z
O(1W)-H(1W1)...O(1)#3	0.819(18)	1.990(18)	2.800(3)	170(4)	#4 -x,-y+1,-z+1
O(1W)-H(1W2)...Cl(1)	0.812(18)	2.93(3)	3.565(3)	137(4)	#1 -x+1,-y+1,-z
O(1W)-H(1W2)...O(11)	0.812(18)	2.14(2)	2.932(4)	164(5)	#2 -x+1,y-1/2,-z+1/2
O(2W)-H(2W1)...O(1W)	0.806(18)	1.96(2)	2.757(4)	168(4)	#3 x-1,y,z
O(2W)-H(2W2)...O(3W)	0.854(19)	2.32(5)	2.923(12)	128(5)	#4 -x,-y+1,-z+1
O(2W)-H(2W2)...O(3W)#4	0.854(19)	2.05(2)	2.895(11)	174(4)	#1 -x+1,-y+1,-z
O(3W)-H(3W2)...O(2W)#4	0.82(2)	2.68(10)	2.895(11)	97(8)	#2 -x+1,y-1/2,-z+1/2
O(3W)-H(3W1)...O(13)	0.81(2)	2.35(11)	2.917(12)	127(12)	#3 x-1,y,z

3.5 Hirshfeld Surface Analysis (HSA)

3.5.1 Hirshfeld Surface Analysis (HSA) for mononuclear complex 1-4

The intermolecular forces of the molecular structures have been quantified using the CIF under Hirshfeld analysis (HSA). HSA surfaces for complexes **1-3** are shown in Fig. 54. Similarly, fingerprint plots are presented in Fig. 55. Fig. 54 reveals surfaces that were mapped over d_{norm} and shape index. The d_{norm} surface has been mapped over a range of -0.5 to 1.5 Å while shape index and curvedness are mapped over the ranges -1.0 to 1.0 Å and -4.0 to 0.4 Å, respectively. For better visualization of the aromatic rings, chelate rings and other entities of all the three complexes these surfaces are presented as transparent. The weak interactions discussed in the structural description for all the three complexes are presented effectively in the various spots. In the d_{norm} surfaces, the large circular deep red depressions are indicating hydrogen bonding contacts. The other dominant interaction C−H···π and π···π interactions for both the complexes in Hirshfeld surface plots are evident as a faint red shaded area.

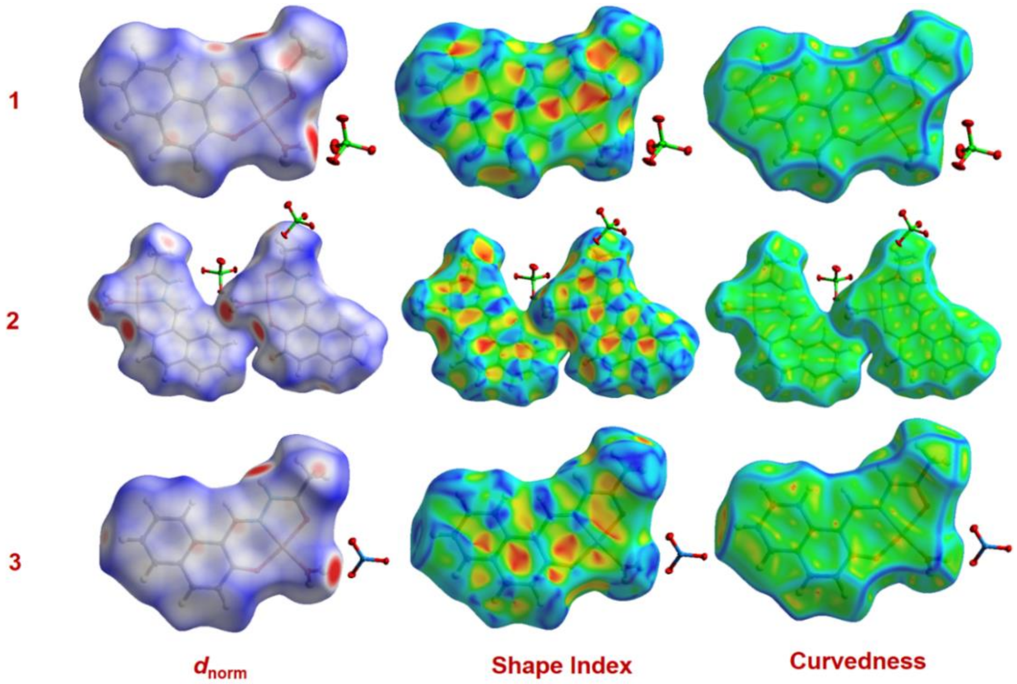

Fig. 54. Hirshfeld surfaces mapped with d_{norm}, shape index and curvedness for **1-3**.

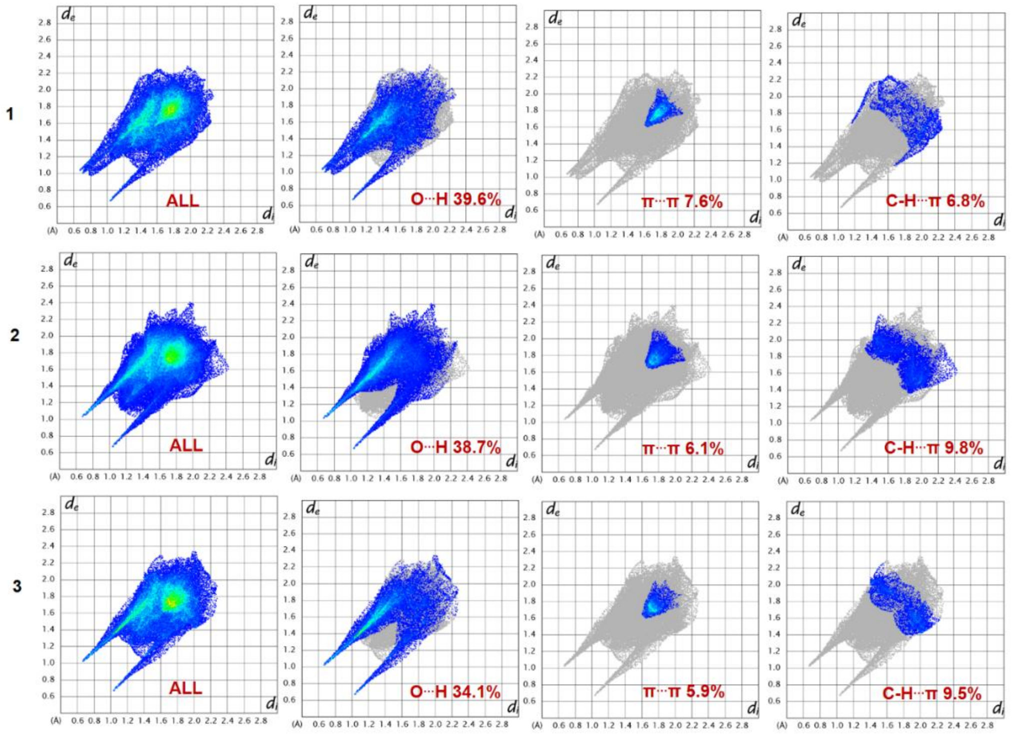

Fig. 55. Fingerprint plots for **1-3** showing percentages of contact contributed to the total Hirshfeld surface area of the molecules.

The fingerprint plots for the complexes **1-3** are presented in Fig. 55. The complementary regions in these plots are visualized where one molecule behaves as a donor ($d_e>d_i$) while other acts as an acceptor ($d_e<d_i$). The fingerprint plots for complex **1** is not having equal sized spikes while in the case of **2** and **3** the spikes are equal in length. The O···H interactions for all the

three complexes appear as two distinct spikes of unequal width in **1** while they are of approximate equal lengths in **2** and **3** in the 2D fingerprint plots in the region 1.05 Å < ($d_e + d_i$) < 2.32 Å (for **1**); 1.05 Å < ($d_e + d_i$) < 2.40 Å (for **2**) and 1.05 Å < ($d_e + d_i$) < 2.35 Å (for **3**) as light sky-blue pattern in full fingerprint 2D plots. Also, π···π interaction area in all these complexes are lying at the center of the fingerprint plot in the region 1.6 Å < ($d_e + d_i$) < 2.0 Å (for **1**); 1.7 Å < ($d_e + d_i$) < 2.1 Å (for **2**) and 1.6 Å < ($d_e + d_i$) < 2.0 Å (for **3**). In addition, C-H···π interactions too appear at the upper region in the corresponding in the fingerprint plots in the region 1.65 Å < ($d_e + d_i$) < 2.20 Å (for **1**); 1.80 Å < ($d_e + d_i$) < 2.30 Å (for **2**) and 1.75 Å < ($d_e + d_i$) < 2.30 Å (for **3**) The fingerprint plots can be split apart to highlight particular atom pair close contacts. This enables separation of contributions from different interaction types, which overlap in the full fingerprint. The proportion of O···H interactions constitutes 39.6%, 38.7% and 34.1% of the total Hirshfeld surfaces in **1**, **2** and **3** respectively. The π···π interactions in **1**, **2** and **3** are having contributions of 7.6%, 6.1% and 5.9% in their respective Hirshfeld surfaces. While CH···π interactions are have contributions of 6.8%, 9.8% and 9.5% to their total Hirshfeld surface area of **1**, **2** and **3** respectively.

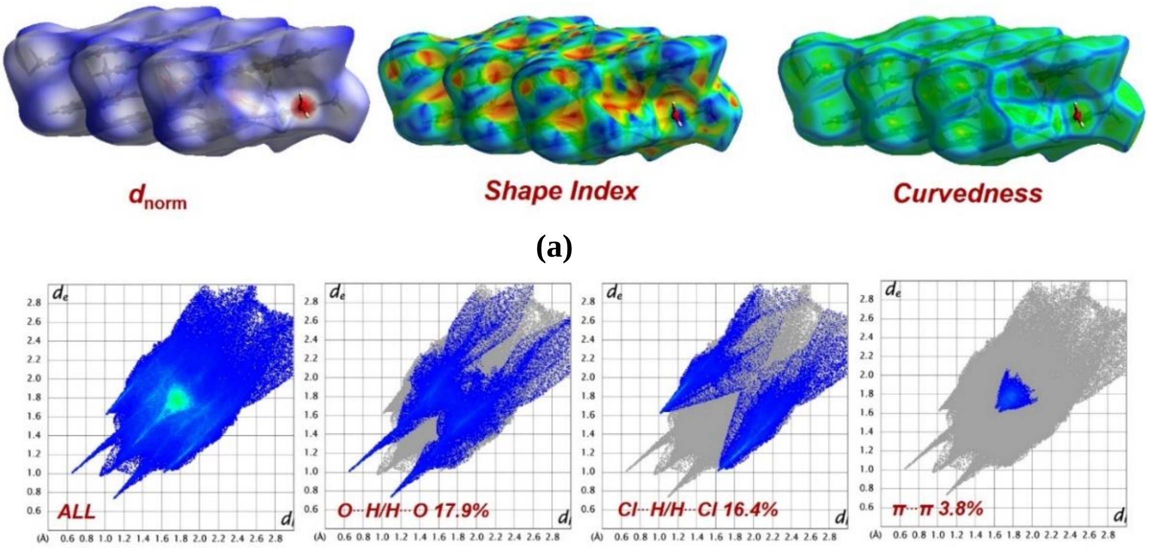

(a)

(b)

Fig. 56. Hirshfeld surfaces mapped with d_{norm}, shape index and curvedness for the complex **4**; **(b)** Fingerprint plots for the complex **4** showing percentages of contact contributed to the total Hirshfeld surface area of the complex **4**.

The Hirshfeld surface for the complex **4** is shown in Fig. 56. For this ligand the d_{norm} surface is mapped between the range of -0.20 to 1.1 Å, shape index is constructed between -0.8 to 0.8 Å and the curvedness is mapped in the range -4.0 to 0.4 Å. All of these surfaces are presented in a transparent fashion to offer better visualization of all the aromatic rings present in the ligand. The O···H and Cl···H interactions which are discussed in the molecular structure description (vide supra) can be visualised as different types of spots in the d_{norm} surface. The large circular deep red depressions in d_{norm} surface are indicative of O···H hydrogen bonding interactions as faint red shaded area while the weak π···π interactions are present as faded areas in the d_{norm} plot of the complex **4**.

In the fingerprint plot of complex **4** (Fig. 56(b)) the opposite regions are shown in the mode where one molecule is acting as a donor ($d_e > d_i$) whilst another behaves as an acceptor ($d_e<d_i$). The fingerprint plot of the complex possess various equal-sized spikes which are indicative of the different interactions present in the complex (vide infra). The most important interaction in the ligand is the O···H/H···O interaction which appears as discrete spikes 0.6 Å < (d_e + d_i) < 3.0 Å in the total fingerprint plot of the complex and contributes 17.9% of the total Hirshfeld surface area. Besides, Cl···H/H···Cl interaction also appears as pair of equal-sized spikes appearing in the region 1.0 Å < (d_e + d_i) < 3.0 Å in the total fingerprint plot of the complex and contributing 16.4% of the total Hirshfeld surface area. Unlike, O···H and Cl···H interactions, the π···π interactions are appearing as a very small sized patch in the center of the total fingerprint plot of the complex. Although it also comprises of very small-sized pair of spikes appearing in the region 1.6 Å < (d_e + d_i) < 2.0 Å in the total fingerprint plot of the complex and contributes 3.8% of the total Hirshfeld surface area.

3.5.2 Hirshfeld Surface Analysis of mixed ligand complexes 5 and 6

The Hirshfeld surfaces are used to associate the average electron density of atoms in a molecule with the entire electron density of crystal, by mapping the spatial contacts between the intermolecular interactions, lattice voids, shape index, surface curvedness, etc. involved in the crystals [100]. Additionally, is useful in demonstrating how the percentage of weak interactions plays a crucial role in developing the crystal geometry in the interstitial spaces in crystals. The white region in the d_{norm} surface illustrating the weak contacts within the van der Waals distance while the red and blue regions dictate the contacts less and more than van der Waals distance, respectively. Such type of in situ analysis permits one to identify how weak interactions govern the molecular packing in the crystals [101-107].

The Hirshfeld surfaces for both copper complexes **5** and **6** are presented in Fig. 57. For better visualization of the molecule, these surfaces are plotted as transparent. The d_{norm} surface for both the complexes has been mapped between -0.4 to 1.4 Å range and shape index plots are covering the range between -0.9 to 0.9 Å while curvedness plots are constructed between -4.0 to 0.4 Å. In both **5** and **6**, the O···H interactions as described in the crystallographic section (*vide supra*) can be seen as the large circular deep red depressions. The comparatively weaker interactions *viz.* CH···π interaction in **5** and π···π interactions in **6** can be seen as a faint red shaded area in the corresponding d_{norm} surfaces [107]. The surface curvedness scan is described as the function of the root mean square curvature of the surface. The close view of surfaces reveals dark blue patches with high surface curvature associated with a flat green surface. The dark blue patches indicate that the supramolecular interactions involved in building molecular packing in both **5** and **6** are not isoenergetic in nature and have variable bond strength. The shape index plot, which is sensitive to small changes in molecular shape due to irregular deformation-induced from the neighbouring crystalline environment, also indicates the mode of packing operating in the crystal. The reddish-yellow hollow section on the shape index plot governs the strong interactions in the crystal and is under the strong influence of the neighbouring environment which is involved in supramolecular interaction. The bump-like area in the shape index plot justifies weak interactions or interactions least affected by the neighbouring crystalline environment (Fig. 57).

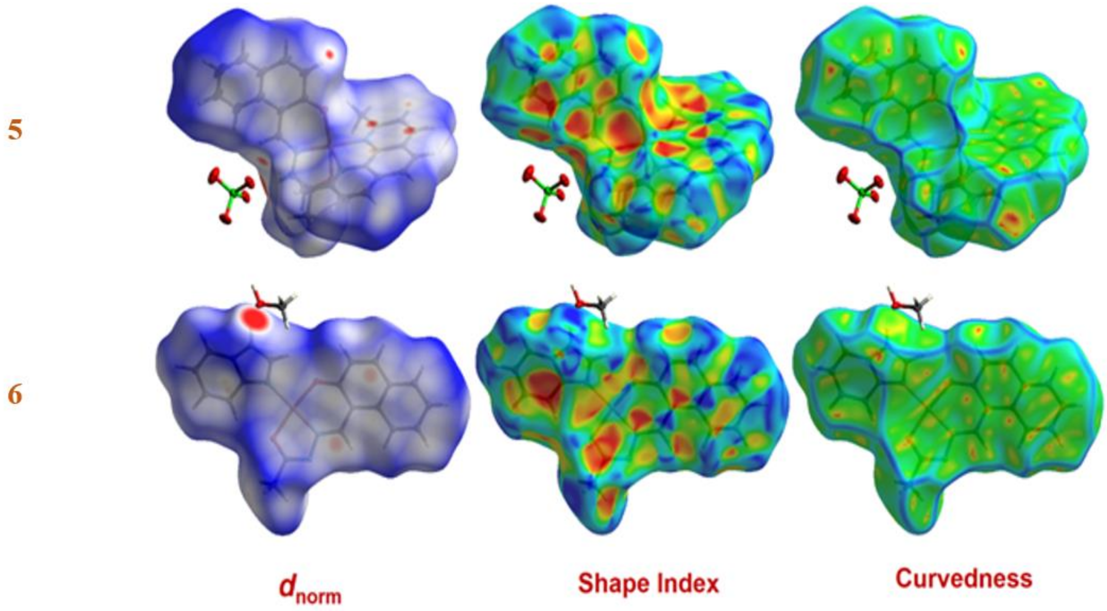

Fig. 57. Hirshfeld surfaces mapped with d_{norm}, shape index and curvedness for complexes **5** and **6**.

Fingerprint plot analyses Fig. 58 another very important outcome of Hirshfeld surface analyses have also been plotted for both the compounds. In fingerprint plots, the paired regions are presented in such a mode where one molecule act as a donor (d_e>d_i) and another as an acceptor (d_e<d_i). The presence of distinct bright red circular spots on d_{norm} surfaces for both complexes is indicative of the presence of hydrogen bonding which is additionally evidenced by the presence of spikes in the fingerprint plots [109]. Additionally, the total fingerprint plot can be split into several groups to have an idea about the specific atom pair close contacts. This enables the estimation of contributions coming from various interactions existing in the molecule. The fingerprint plots of both the complexes display a light blue region which represents various interactions existing in the complex (vide infra). In **5**, the most important interaction in the ligand is the O···H/H···O interaction which appears as discrete unequal spikes 0.7 Å < (d_e + d_i) < 2.8Å in the total fingerprint plot with21.8% contribution. In addition, H···π/π···H interaction too appears in **5** which contributes 22.3% in the total fingerprint plot and exist between 1.1 Å < (d_e + d_i) < 2.8 Å. In **6**, the O···H/H···O appearing as sharp unequal spikes in the region 0.7 Å < (d_e + d_i) < 2.4 Å and contributes 8.1% in the total Hirshfeld surface area of the complex. While π···π interactions appearing in the center of the total fingerprint plot between in 1.6 Å < (d_e + d_i) <2.0 Å with an overall contribution of 3.6% in the total fingerprint plot.

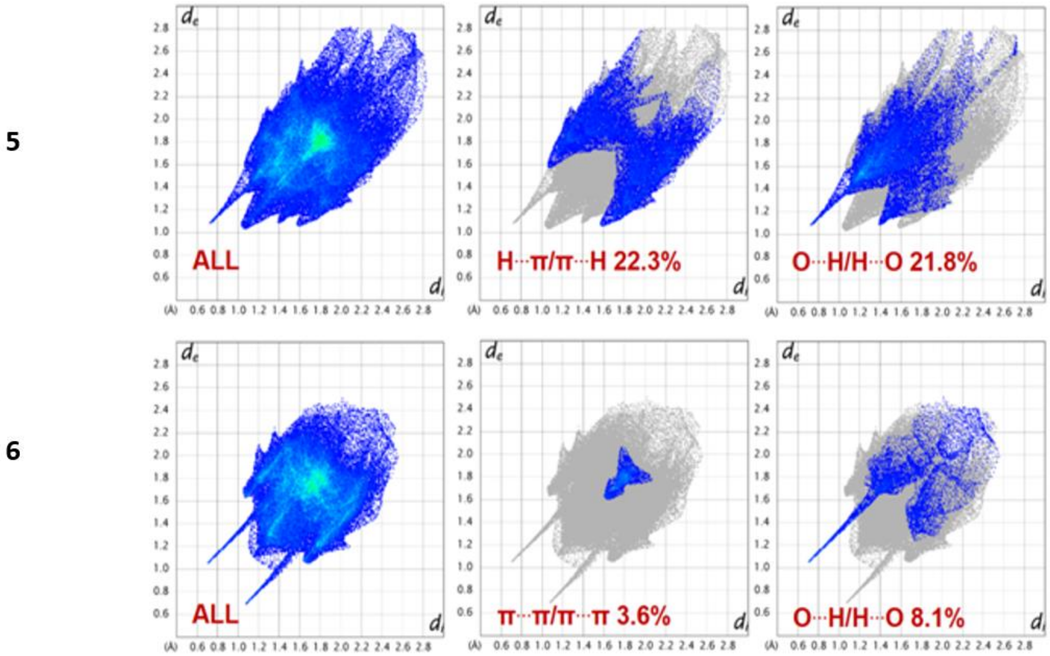

Fig. 58. Fingerprint plots for the ligand showing percentages of contact contributed to the total Hirshfeld surface area in complexes **5** and **6**.

Besides, crystal lattice void space has been evaluated with standard void cluster parameter "unit cell +5.0 Å" Fig. 59. From crystal void calculation, a pro-molecule surface capped within the unit cell, which incorporates all atoms in the molecule, is generated within a crystal radius of 5.0 Å. It quantifies the void space present in the crystal lattice. The data obtained from the calculation portrays that **5** has lattice void volume 451.20 Å^3 with void area 996.80 Å^2 with sphericity and globular indices of 0.289 and 0.285 units, respectively. Likewise, in **6** lattice void volumes of 253.52 Å^3 with void area 734.99 Å^2 with sphericity and globular indices of 0.096 and 0.264 units, respectively. The void volumes for both the complexes are large sizes which indicate the presence of strong non-covalent interactions in. The globular index is also very less and all these evidences collectively support that the supramolecular architecture is build up with the combination of strong and weak non-covalent interactions.

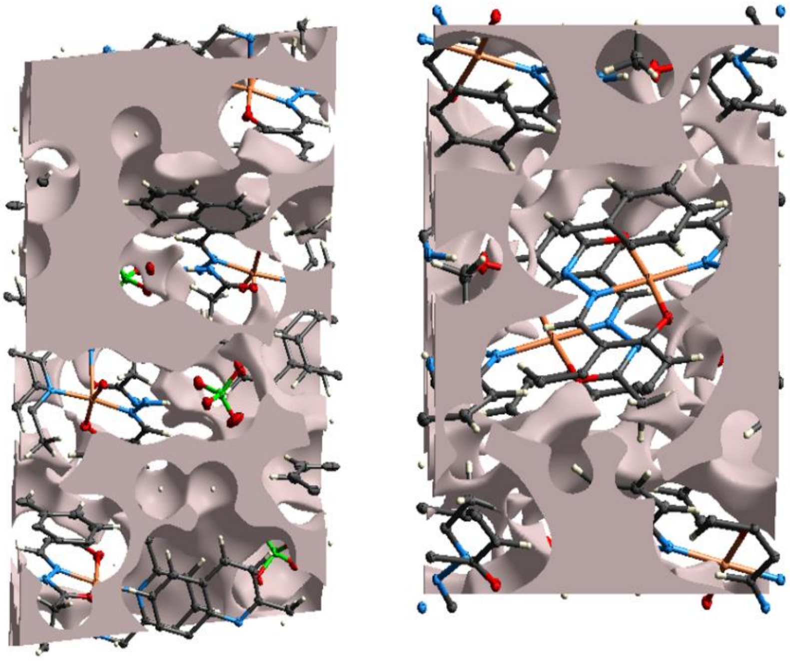

5 **6**

Fig. 59. Crystal void calculated with standard void cluster parameter "unit cell +5.0Å" for **5** and **6**.

3.5.3 Hirshfeld Surface Analysis of binuclear complexes 7-9

The Hirshfeld surfaces for complexes **7, 8** and **9** are presented in Fig. 60. The d_{norm} surface has been mapped over a range of -0.5 to 1.45 Å while shape index, as well as curvedness, are mapped over the ranges -0.9 to 0.9 Å and -4.0 to 0.4 Å, respectively. All the three types of surfaces shown in Fig. 60 have been shown as transparent to offer visualization of the molecular framework. All of the weak non-covalent interactions as described in the crystal structures for all the three complexes can be seen as varied spots in the d_{norm} surfaces. In the d_{norm} surfaces the large circular deep red depressions are indicating hydrogen bonding contacts such as O···H and N···H interactions while other dominant interaction C−H···π and π···π interactions are evinced as a faint red shaded area.

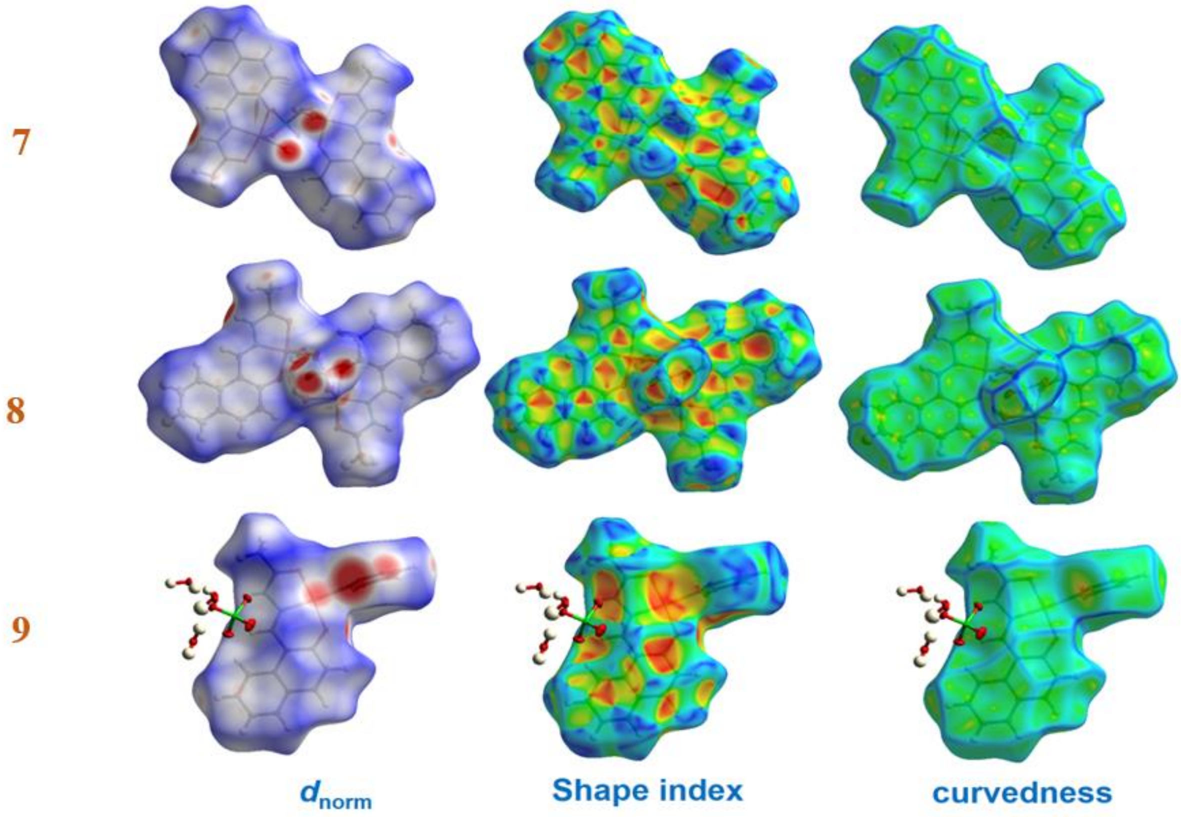

Fig. 60. Hirshfeld surfaces mapped with d_{norm}, shape index and curvedness for **7-9**.

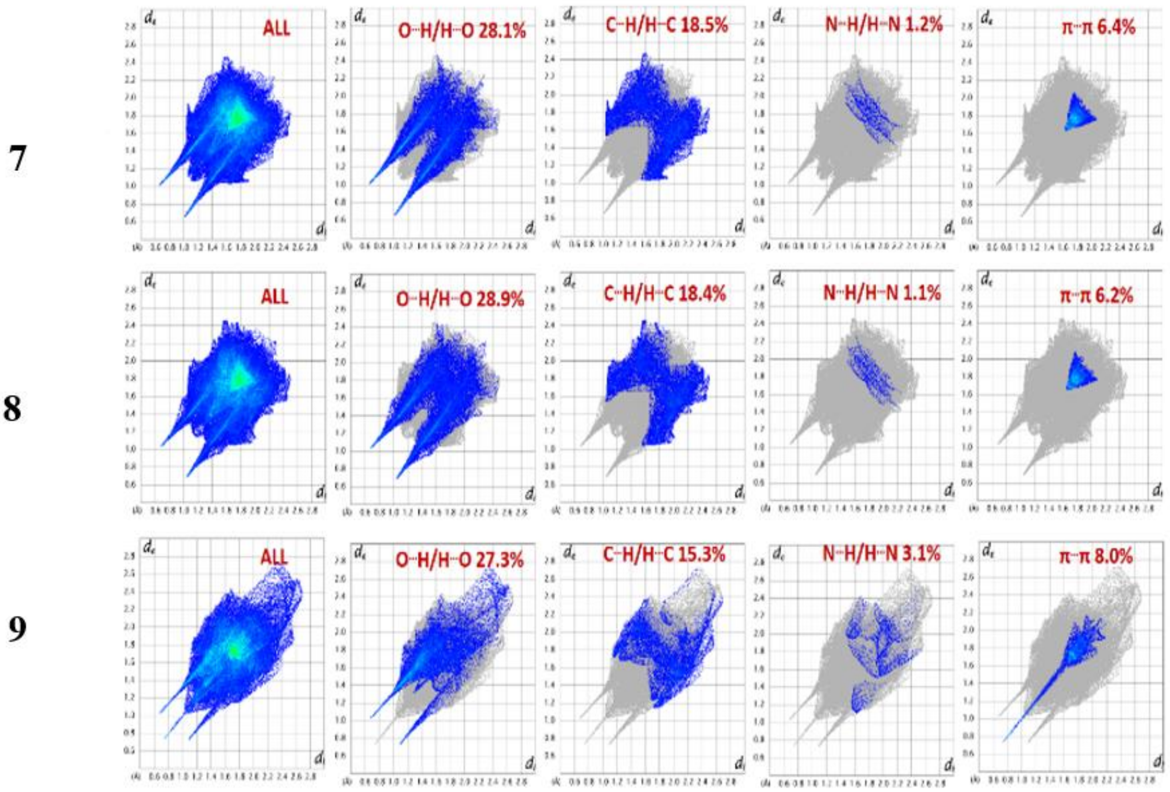

Fig. 61. Fingerprint plots for **7**, **8** and **9** showing percentages of contact contributed to the total Hirshfeld surface area of the molecules.

Another very pertinent result of the Hirshfeld surface analyses is the fingerprint plots which are presented in Fig. 61. In all these plots, the complementary regions can be visualized in the mode where one molecule act as donor ($d_e > d_i$) and another behaves as acceptor ($d_e < d_i$). The total fingerprint plots have been split apart to highlight particular atom pair close contacts which enabled the separation of contributions from different interaction types, which overlap in the full fingerprint. The fingerprint plots for all three complexes are having equal-sized spikes and represent varied interactions existing in the complexes (vide infra). The O···H interactions in complexes **7** and **8** exist as distinct spikes while in **9**in addition to the pair of spikes its 2D fingerprint plots possess a small notch indicating the presence of uncoordinated counter anion as well as an aqua molecule. In **7**the O···H interactions appear in the region 0.64 Å < ($d_e + d_i$) < 2.45 Å while in **8** these interactions also appear in an almost similar region as both 6 and 7 are iso-structural in nature. In **9**, the O···H interaction appears in 0.62 Å < ($d_e + d_i$) < 2.70 Å region. The C···H interaction in complexes **7**, **8** and **9** lie in the area 1.0 Å < ($d_e + d_i$) < 2.5 Å; 1.0 Å < ($d_e + d_i$) < 2.5 Å and 1.1 Å < ($d_e + d_i$) < 2.6 Å, respectively. In **7** and **8,** the N···H interaction occupy the upper portion of the fingerprint plot in region 1.45 Å < ($d_e + d_i$) < 2.20 Å while in **9** it appears at around 1.5 Å < ($d_e + d_i$) < 2.5 Å. The π···π interactions in **7** and

8 occupy almost the same area in the region 1.6 Å < (d_e + d_i) < 2.0 Å while in **9**, they are present as peculiar spikes emanating from 0.7 Å < (d_e + d_i) < 2.2 Å. The different percentage contributions of these interactions are presented in Fig. 61.

3.6 DFT Calculations

3.6.1 Optimized structure of complexes 1-4

The molecular geometry was optimized by the Gaussian 09 with the level of B3LYP basis set [110]. The optimized structures of all complexes are shown in Fig. 62-65. There are slight differences in bond parameters, owing to the theoretical calculations were carried out on an isolated molecule in the gas phase [111-114]. The geometry of complexes **1-3** is a distorted square planar. Distortion index τ_4 is also estimated [84, 115]. Based on the distortion index, the geometry of **1-3** is distorted square planar. These observations are in the same line of single-crystal X-ray analysis.

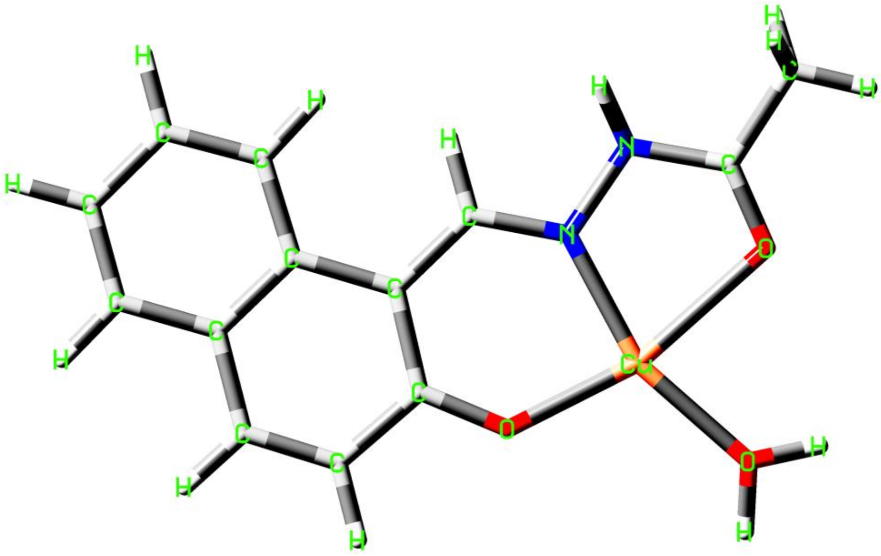

Fig. 62. Optimized structure of complexes **1.**

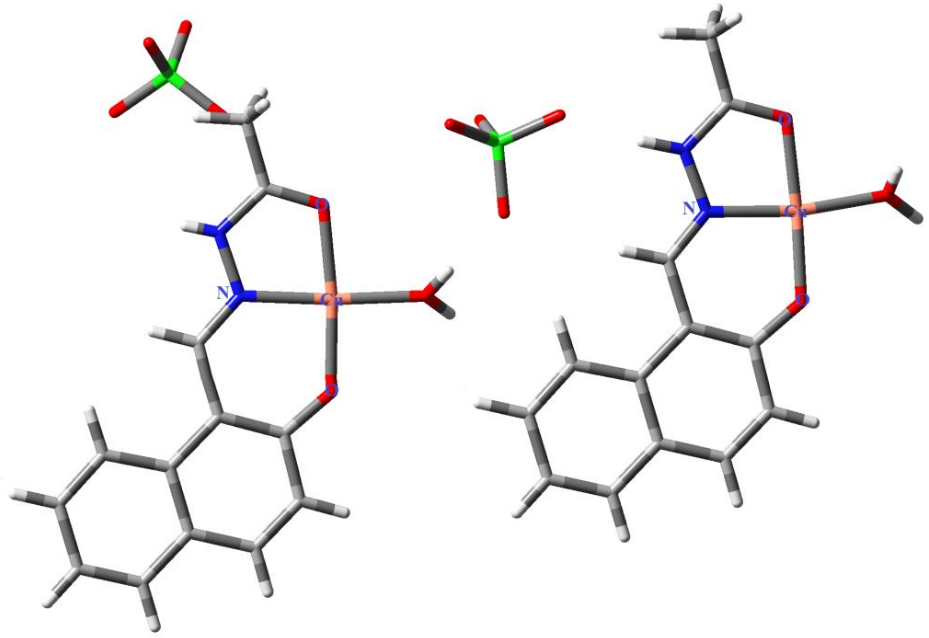

Fig. 63. Optimized structure of complexes **2.**

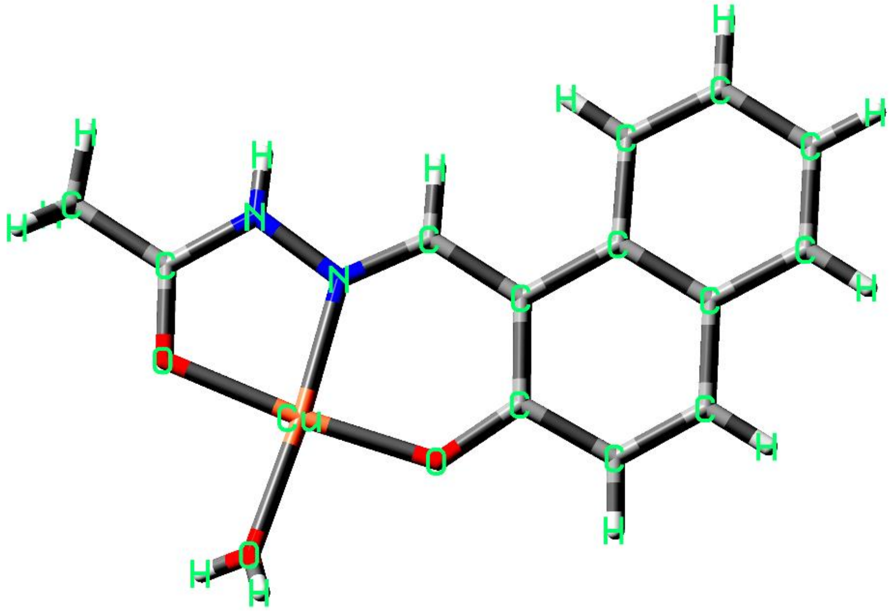

Fig. 64. Optimized structure of complex **3**.

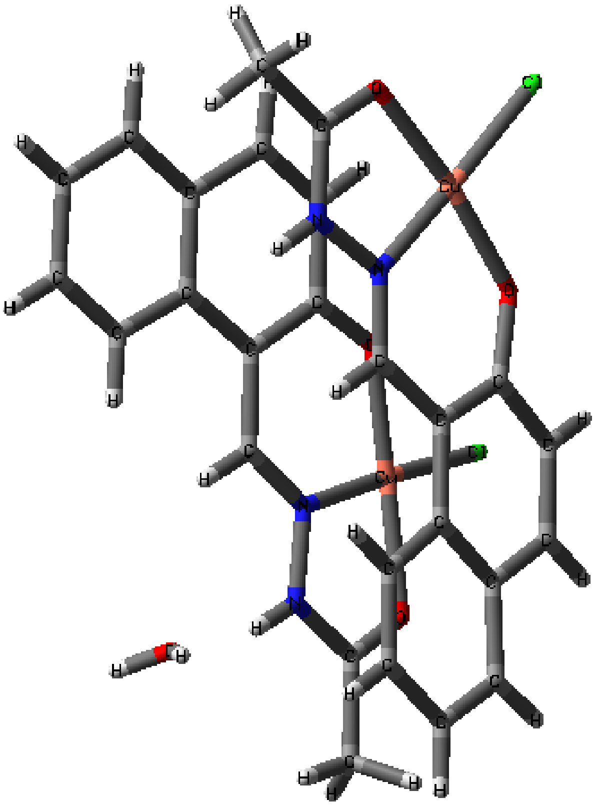

Fig. 65. Optimized structure of complex **4**.

3.6.2 HOMO-LUMO analysis and electronic properties

The electronic structures of complexes **1-4** by characterized by analyzing the highest occupied molecular orbital (HOMO) and lowest unoccupied molecular orbitals (LUMO). The HOMO-LUMO energy gaps (ΔE) furnish information about the reactivity and nature (soft or hard) of a given molecule. The graphical representations (counter plots) of frontier molecular orbitals (FMO) are depicted in Fig. 66-69. These HOMO and LUMO energies are negative for all complexes (**1-4**), indicating that the complexes are stable [116]. The ΔE also predicts the various reactivity parameters, which additionally reveal the internal charge transfer, susceptibility and stability of molecules [117-120]. These reactivity parameters are collected with their mathematical definition in Table 11. The variations in parameters are due to the structural variation of the complexes. Reactivity parameters such as energy gap (ΔE), ionization potential (I), electron affinity (EA), electronegativity (χ), chemical potential (μ), global hardness (η), softness (S), electrophilicity index (ω), electron-donating capacity (ω-) and electro accepting capacity (ω+) for complexes **1-4** were estimated from energy calculations, taking in to account the ground state geometry optimization. On perusal of reactivity parameters, the observed trend of ionization potential, electronegativity and global hardness is **2** > **3** > **4** > **1** whereas the trend of electron affinity is **4** > **3** > **2** > **1**.

Table 11 The crucial electronic parameters (in eV) for complexes **1-4**.

Molecular Descriptors	Mathematical descriptors	1	2	3	4
E_{HOMO} (eV)	Energy of HOMO	-3.0009	-9.3490	-5.5700	-8.2400
E_{LUMO} (eV)	Energy of LUMO	-2.9762	-3.3058	-3.6190	-6.5739
Energy gap (ΔE)	$\Delta E = E_{HOMO} - E_{LUMO}$	0.0247	6.0432	1.9510	1.6661
Ionization potential (I)	$I = - E_{HOMO}$	3.0009	9.3490	5.5700	8.2400
Electron affinity (EA)	$EA = - E_{LUMO}$	2.9762	3.3058	3.6190	6.5739
Electronegativity (χ)	$\chi = (I+EA)/2$	2.98855	6.3274	4.5954	7.40695
Chemical potential (μ)	$\mu = - \chi$	-2.98855	-6.3274	-4.5945	-7.40695
Global hardness (η)	$\eta = (I-EA)/2$	0.01235	3.0216	0.9755	0.83305
Softness (S)	$S = 1/2\eta$	40.4858	0.1654	0.5073	0.6002
Electrophilicity index (ω)	$\omega = \mu^2/2\eta$	349.5982	40.0359	10.8198	32.9289
Electron donating capacity (ω-)	$\omega- = (3E_{HOMO} + E_{LUMO})^2 / 16(E_{HOMO} – E_{LUMO})$	363.0922	10.1663	13.2389	36.7365
Electro accepting capacity (ω+)	$\omega+ = (E_{HOMO} + 3E_{LUMO})^2 / 16(E_{HOMO} – E_{LUMO})$	360.1037	3.8389	8.6445	29.9597

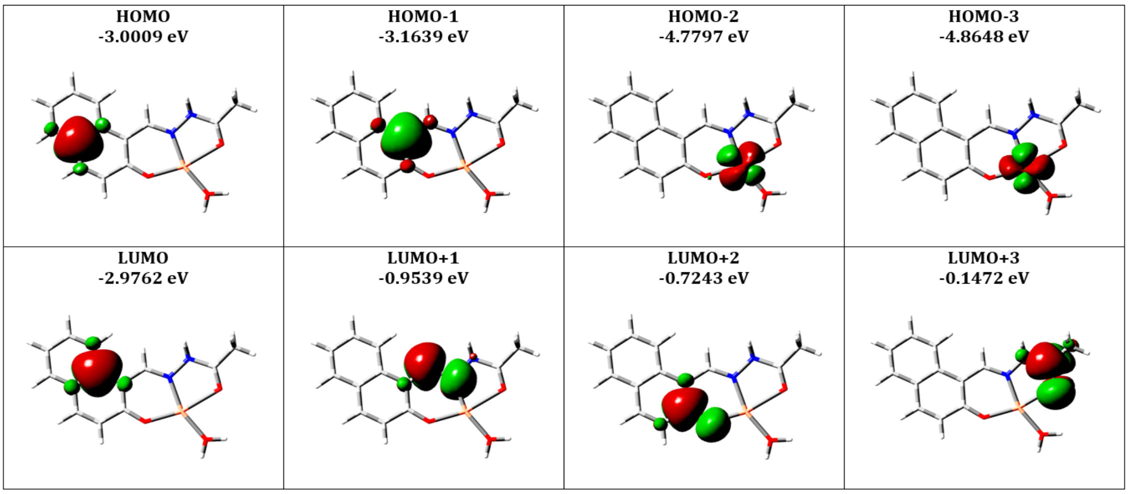

Fig. 66. HOMO-LUMO energy level diagram of complex **1**.

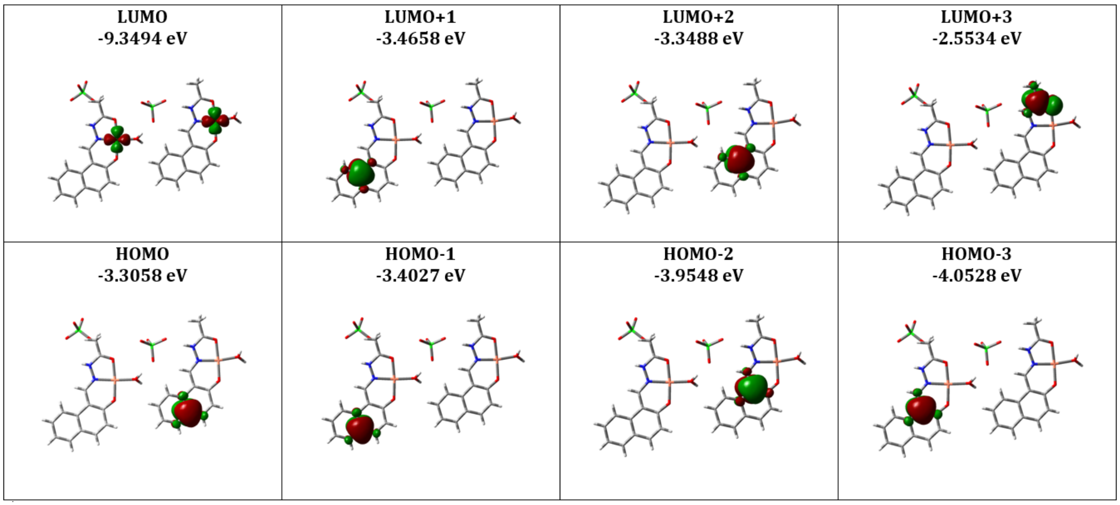

Fig. 67. HOMO-LUMO energy level diagram of complex **2**.

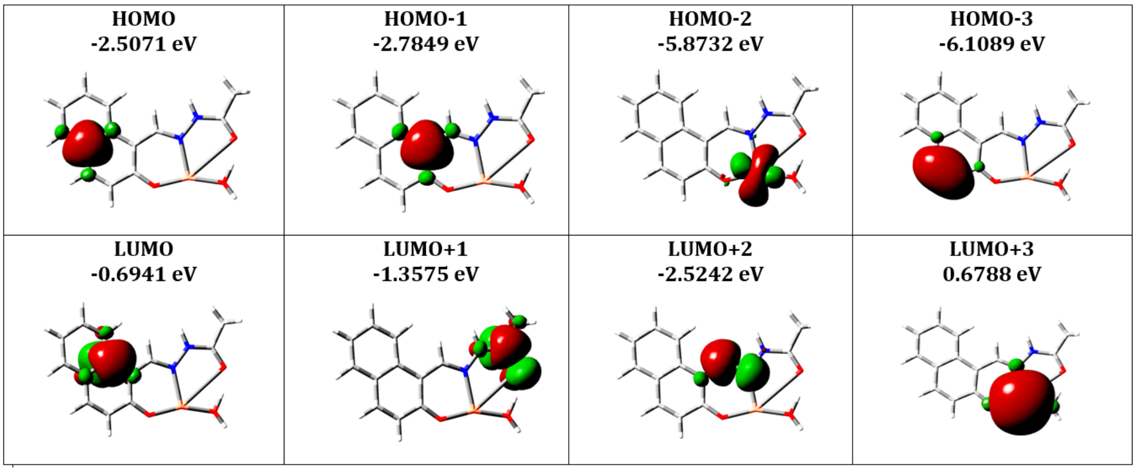

Fig. 68. HOMO-LUMO energy level diagram of complex **3**.

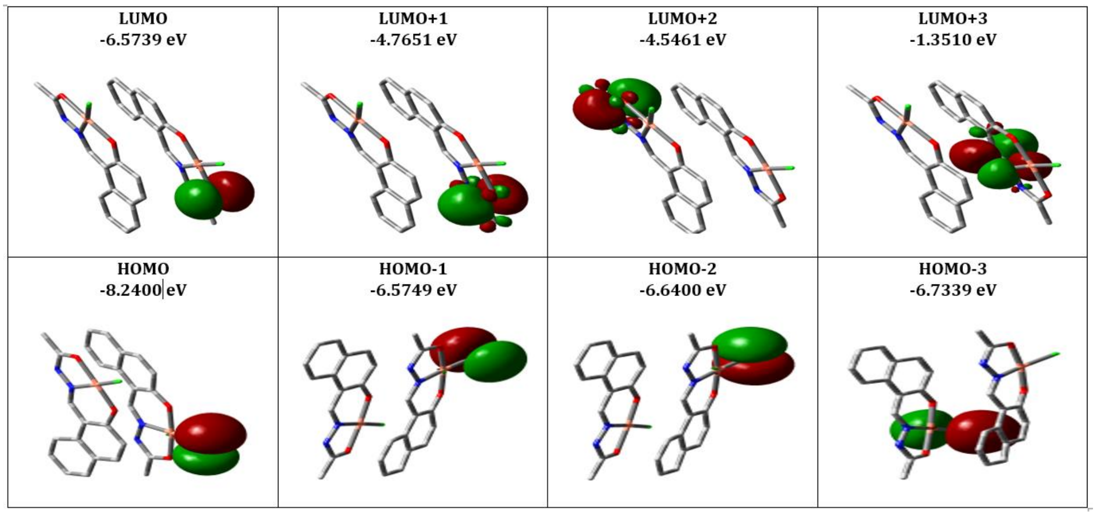

Fig. 69. HOMO-LUMO energy level diagram of complex **4**.

The calculated spin densities, total density and spin surface were performed using the B3LYP/LANL2DZ as basis sets for complexes **1**-**4**. Fig. 70-73. illustrates the spin densities for the ground state. The spin density plot has been obtained with the isosurface cut-off value of 0.002. The spin density distributions are mainly delocalized into the copper atom and those atoms which are directly coordinated to the copper atom [116]. The positive signed densities are spread over the metal center and the negative signed spin densities are distributed over the coordinated donor atoms. Such spin density distributions were also in agreement with HOMO-LUMO shapes observed in both complexes. It is also shown from DFT calculations that the DFT data agrees with epr spectral data from which a mainly ligand centered character of the unpaired electron in $d_{x^2-y^2}$ along with axial features of epr signals was concluded [117, 118].

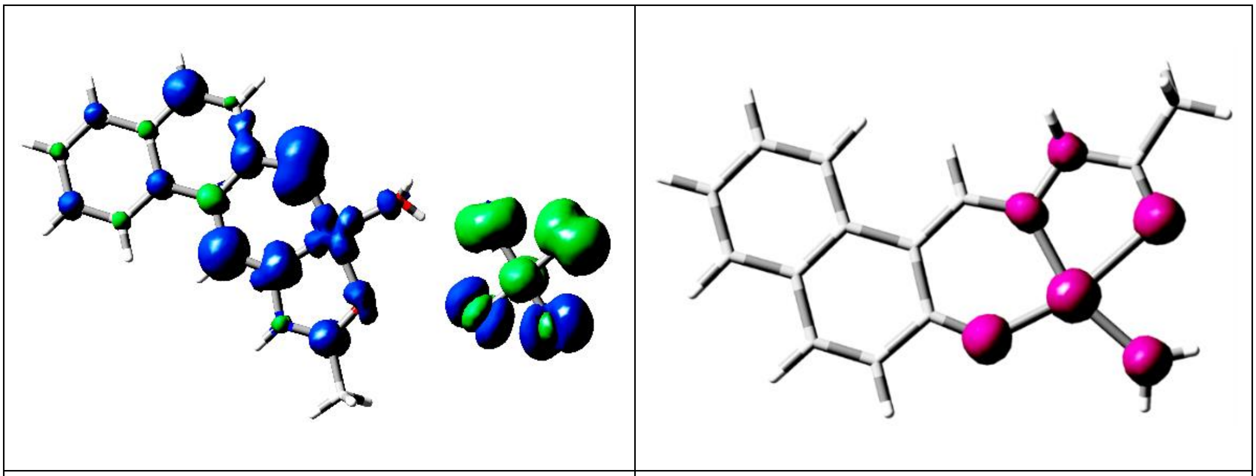

(a) Spin density plot

(b) Total density plot

Fig. 70. (a) Spin density and **(b)** Total density plots of complex **1**.

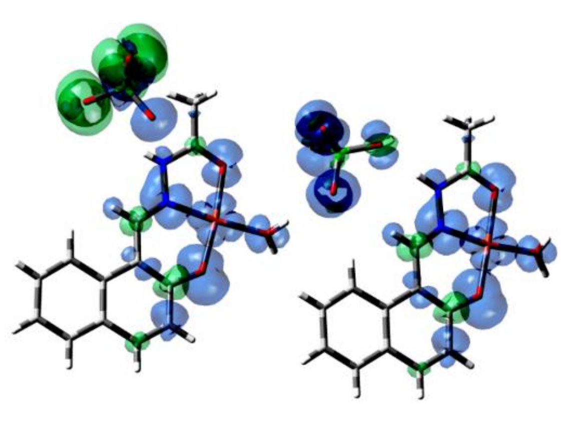	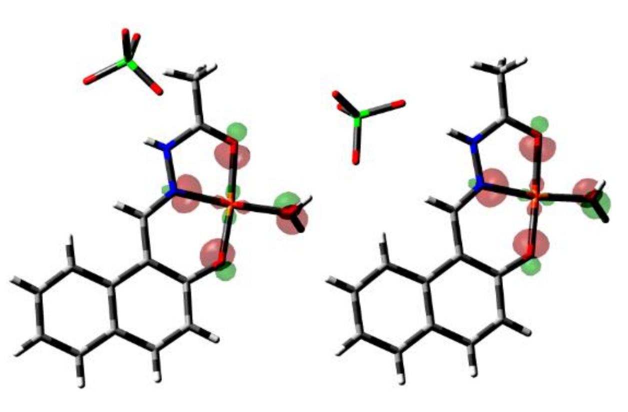
(a) Spin density plot	**(b)** Spin surface plot

Fig. 71. (a) Spin density and **(b)** Spin surface plot of complex **2**.

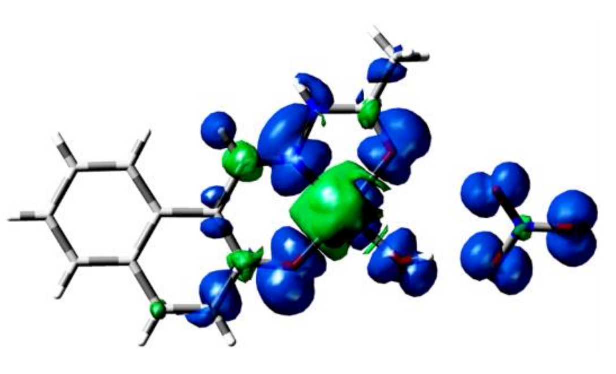	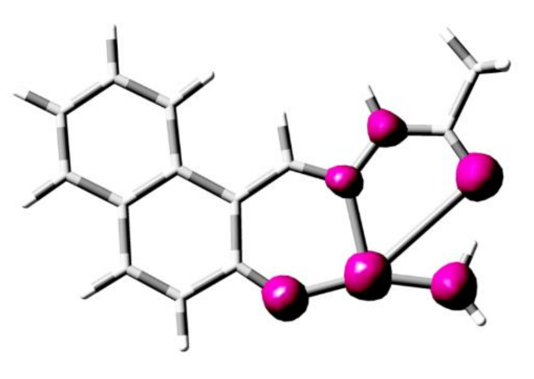
(a) Spin density plot	**(b)** Total density plot

Fig. 72. (a) Spin density and **(b)** Total density plots of complex **3**.

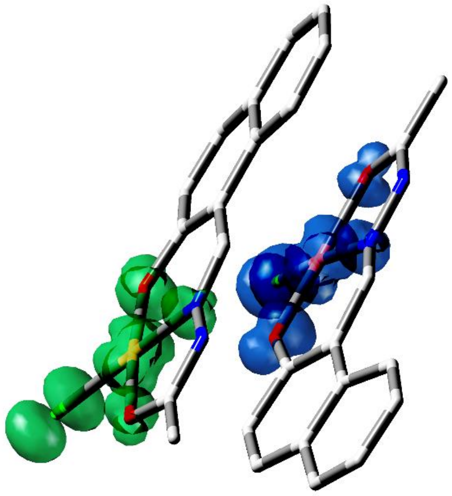

Fig. 73. Spin density plots of complex **4**.

3.6.3 TD-DFT Calculations of complex 5 and 6

Full geometry optimizations were carried of complex **5** and **6** using density functional theory (DFT) at the PBE0-D3BJ/def2-TZVP level of theory in the gas phase using the available crystal structure [121-124]. The def2-ECP effective core potential was used for the Cu atom [125]. Vertical electronic excitations were computed using the time-dependent density functional theory (TD-DFT) formalism [126]. TD-DFT calculations were performed at the M06/def2-TZVP level of theory [127] using the PBE0-D3BJ/def2-TZVP optimized geometries. M06 has been reported as one of the most reliable DFT functional for the calculation of electronic absorption spectra for Cu(II) complexes [128]. To correlate more closely with the experimental environment, TD-DFT calculations were performed in DMSO solvent using the implicit conductor-like polarizable continuum salvation model (CPCM) [129].

To explain the electronic transitions in the UV-Vis results, we have carried out TD-DFT calculations at the M06/def2-TZVP level of theory for complexes **5** and **6**. Fig. 74 and 75 shows the overlap between the optimized and the X-ray diffraction (XRD) structures. Optimized geometries resemble the XRD structures satisfactorily, which is a good starting point to accurately calculate the electronic absorption spectra. For both complexes, the calculated electronic absorption spectra focused on 25 low-energy transition singlet states are shown in Fig. 76. Similar to the experimental results, the appearance of two more intense and broad peaks in the range of 270-460 nm and one less intense and very broad feature in the lower-energy region suggest that the calculated spectrum can be considered as a suitable simulation for the experimental spectrum. The excitation energies, oscillator strength parameters, and corresponding major orbital contributions for important electronic transitions are provided in Table 12. The complete set for all 25 low-energy electronic transitions is given in Table 13. A TD-DFT result describes each excitation as involving contributions from many occupied and unoccupied molecular orbitals. We discuss here only the major contribution of the transition. For complex **5**, two bands appear at the high energy end with broadness of ~70 nm, and ~100 nm, which consist of numerous electronic transitions with maxima at 326.1 nm and 395.9 nm, respectively (Table 12). These peaks resemble the bands observed experimentally at 325 nm and 424 nm, respectively. The band at 326 nm is mainly caused by the HOMO-1(α)→LUMO+1(α) and HOMO-1(β)→LUMO+2(β) electronic excitations, and at 395.9 nm is mainly caused by the HOMO(α)→LUMO+1(α), HOMO(β)→LUMO+1(β)and HOMO(β)→LUMO+2(β) electronic transitions. Molecular orbital plots suggest that these occupied and unoccupied molecular orbitals are mainly located on the benzene rings of the ligand (Fig. 77), and thus both electronic transitions can be assigned to π…π* and intra ligand charge transfer (ILCT) / ligand to ligand charge transfer (LLCT) type. Similar, ILCT transitions appear at 310.0 nm and 382.9 nm for complex **6**. Significantly involved occupied (HOMO(α), HOMO(β), HOMO-2(α) and HOMO-1(β)) and unoccupied (LUMO(α) and LUMO+1(β)) molecular orbitals are located on the same ligand (Fig. 78).

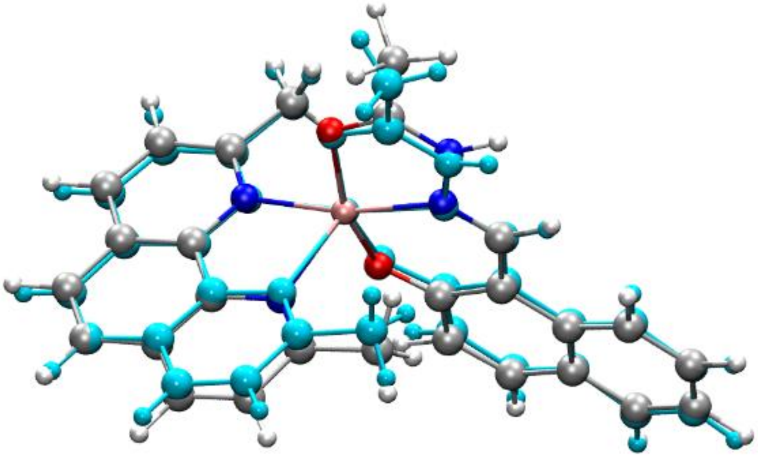

Fig. 74. Comparison of the PBE0-D3BJ/def2-TZVP optimized geometries (element color) and XRD crystal structures (cyan color) for complex **5**.

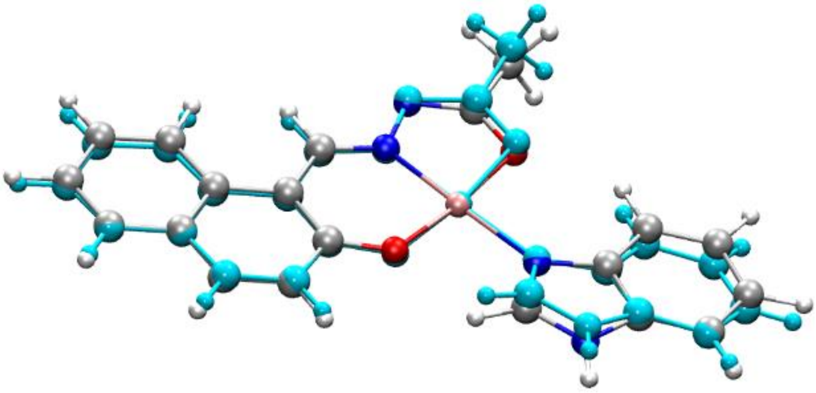

Fig. 75. Comparison of the PBE0-D3BJ/def2-TZVP optimized geometries (element color) and XRD crystal structures (cyan color) for complex **6**.

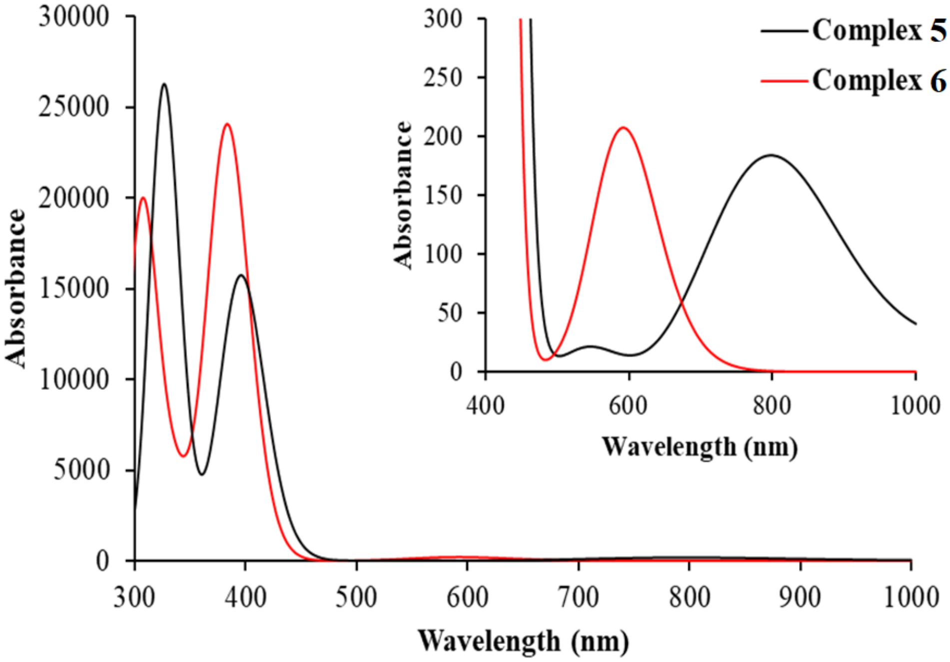

Fig. 76. The calculated UV-Vis absorption spectra for complexes **5** and **6**.

In the lowest-energy region, a very broad low-intensity feature appeared in the range of 610-1000 nm with a maximum of 817.1 nm for the complex **5**, and in the range of 480-750 nm with a maximum of 592.6 nm for the complex **6**. A transition in this lowest-energy region is from the variously occupied orbitals to the LUMO (β) for both complex **5** and **6**, which is mainly located on the Cu atom. However, participating low energy occupied orbitals are located on ligands, and high energy occupied orbitals are located on the metal center (Fig. 68 and 69). These results suggest that the transitions in the lowest-energy region are mixed bands with *d-d* transition and ligand to metal transition (LMCT).

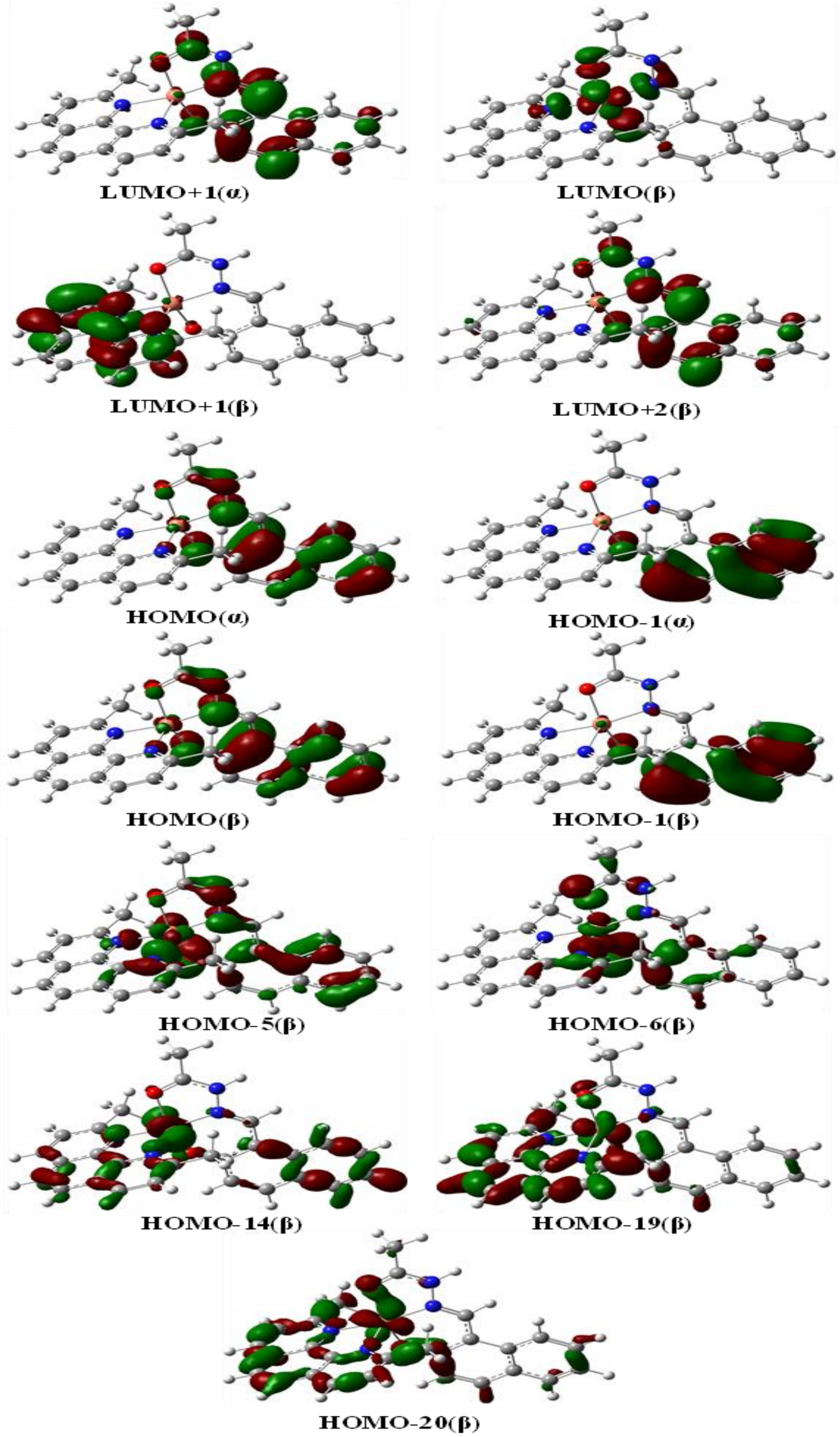

LUMO+1(α) LUMO(β)

LUMO+1(β) LUMO+2(β)

HOMO(α) HOMO-1(α)

HOMO(β) HOMO-1(β)

HOMO-5(β) HOMO-6(β)

HOMO-14(β) HOMO-19(β)

HOMO-20(β)

Fig. 77. Selected molecular orbitals plots for ground-state geometry of **5**.

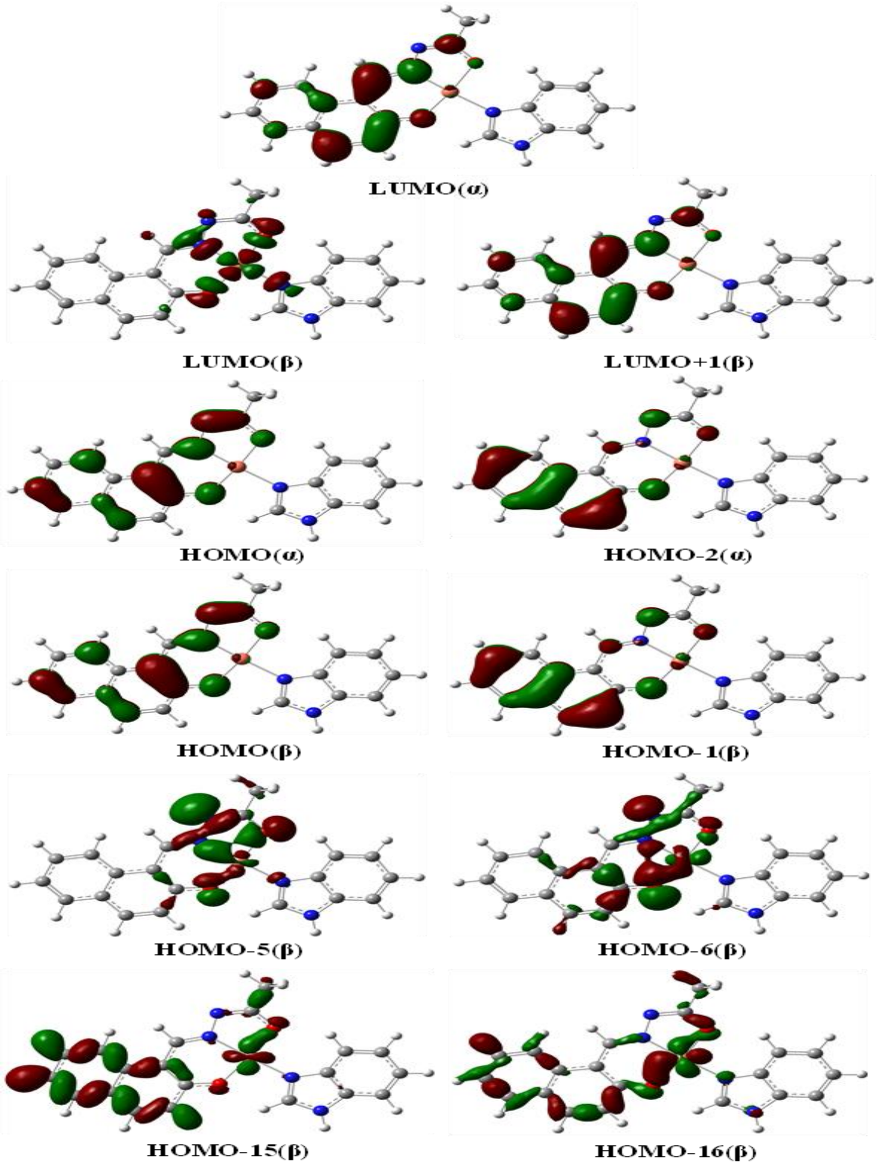

Fig. 78. Selected molecular orbital plots for ground-state geometry of **6**.

Table 12 Selected vertical excitations calculated by TD-DFT/M06/def2-TZVP method in the DMSO solvent.

Transition	$\lambda_{max(Cal.)}$ (nm)	Energy (10^3 cm^{-1})	Oscillator strength	Major contributions	Nature of transition
5					
S_2	817.1	12.2	0.002	HOMO-20(β)→LUMO(β) (12%) HOMO-19(β)→LUMO(β) (11%) HOMO-14(β)→LUMO(β) (10%) HOMO-6(β)→LUMO(β) (13%)	LMCT LMCT *d-d* transition *d-d* transition *d-d* transition

				HOMO-5(β)→LUMO(β) (14%)	
S_{11}	395.9	25.3	0.199	HOMO(α)→LUMO+1(α) (39%) HOMO(β)→LUMO+1(β) (11%) HOMO(β)→LUMO+2(β) (35%)	ILCT LLCT ILCT
S_{21}	326.1	30.7	0.306	HOMO-1(α)→LUMO+1(α) (29%) HOMO-1(β)→LUMO+2(β) (28%)	ILCT ILCT
6					
S_2	592.6	16.9	0.003	HOMO-16(β)→LUMO(β) (35%) HOMO-15(β)→LUMO(β) (12%) HOMO-6(β)→LUMO(β) (22%) HOMO-5(β)→LUMO(β) (13%)	LMCT LMCT *d-d* transition *d-d* transition
S_8	382.9	26.1	0.331	HOMO(α)→LUMO(α) (47%), HOMO(β)→LUMO+1(β) (46%)	ILCT ILCT
S_{19}	310.0	32.3	0.189	HOMO-2(α)→LUMO(α) (42%) HOMO-1(β)→LUMO+1(β) (42%)	ILCT ILCT

Table 13 Vertical excitations calculated by TD-DFT/M06/def2-TZVP method in DMSO solvent.

Transition	**$\lambda_{max(Cal.)}$ (nm)**	**Energy (10^3 cm^{-1})**	**Oscillator strength**	**Major contributions**
5				
S_1	1399.5	7.1	0.001	HOMO-18(β)→LUMO(β) (12%) HOMO-4(β)→LUMO(β) (27%) HOMO(β)→LUMO(β) (34%)
S_2	817.1	12.2	0.002	HOMO-20(β)→LUMO(β) (12%) HOMO-19(β)→LUMO(β) (11%) HOMO-14(β)→LUMO(β) (10%) HOMO-6(β)→LUMO(β) (13%) HOMO-5(β)→LUMO(β) (14%)
S_3	725.5	13.8	0.001	HOMO-16(β)→LUMO(β) (13%) HOMO-14(β)→LUMO(β) (13%) HOMO-6(β)→LUMO(β) (12%) HOMO(β)→LUMO(β) (16%)

S_4	681.9	14.7	0.000	HOMO-18(β)→LUMO(β) (17%) HOMO-17(β)→LUMO(β) (31%) HOMO-7(β)→LUMO(β) (11%)
S_5	550.1	18.2	0.000	HOMO-18(β)→LUMO(β) (20%) HOMO(β)→LUMO(β) (30%)
S_6	534.6	18.7	0.000	HOMO(α)→LUMO+1(α) (40%) HOMO(β)→LUMO+2(β) (38%)
S_7	437.3	22.9	0.000	HOMO-2(α)→LUMO+2(α) (31%) HOMO-2(β)→LUMO+3(β) (31%)
S_8	430.8	23.2	0.000	HOMO-1(α)→LUMO+1(α) (29%) HOMO-1(β)→LUMO+2(β) (29%)
S_9	417.7	23.9	0.000	HOMO-2(β)→LUMO(β) (24%) HOMO-1(β)→LUMO(β) (59%)
S_{10}	410.3	24.4	0.003	HOMO-2(β)→LUMO(β) (66%) HOMO-1(β)→LUMO(β) (19%)
S_{11}	395.9	25.3	0.199	HOMO(α)→LUMO+1(α) (39%) HOMO(β)→LUMO+1(β) (11%) HOMO(β)→LUMO+2(β) (35%)
S_{12}	389.5	25.7	0.006	HOMO-2(α)→LUMO(α) (12%) HOMO-2(β)→LUMO+1(β) (12%) HOMO(β)→LUMO+1(β) (54%)
S_{13}	385.4	25.9	0.009	HOMO-2(α)→LUMO(α) (29%) HOMO-2(β)→LUMO+1(β) (27%) HOMO(β)→LUMO+1(β) (27%)
S_{14}	380.9	26.3	0.004	HOMO(α)→LUMO(α) (84%)
S_{15}	363.7	27.5	0.001	HOMO(α)→LUMO+3(α) (19%) HOMO-3(β)→LUMO(β) (22%) HOMO(β)→LUMO+4(β) (20%)
S_{16}	363.5	27.5	0.000	HOMO(α)→LUMO+3(α) (12%) HOMO-3(β)→LUMO(β) (34%) HOMO(β)→LUMO+4(β) (12%)
S_{17}	355.6	28.1	0.001	HOMO-4(α)→LUMO(α) (22%) HOMO-3(β)→LUMO(β) (41%) HOMO-3(β)→LUMO+1(β) (20%)
S_{18}	352.4	28.4	0.001	HOMO(β)→LUMO+3(β) (91%)
S_{19}	345.4	28.9	0.001	HOMO(α)→LUMO+2(α) (94%)
S_{20}	328.4	30.4	0.023	HOMO-5(β)→LUMO(β) (41%) HOMO-4(β)→LUMO(β) (37%)
S_{21}	326.1	30.7	0.306	HOMO-1(α)→LUMO+1(α) (29%) HOMO-1(β)→LUMO+2(β) (28%)
S_{22}	324.8	30.8	0.000	HOMO-4(α)→LUMO+2(α) (37%) HOMO-3(β)→LUMO+3(β) (39%)
S_{23}	324.3	30.8	0.013	HOMO-3(α)→LUMO+1(α) (69%)
S_{24}	321.3	31.1	0.021	HOMO-2(α)→LUMO(α) (29%) HOMO-1(α)→LUMO+1(α) (11%) HOMO-2(β)→LUMO+1(β) (31%) HOMO-1(β)→LUMO+2(β) (11%)
S_{25}	317.5	31.5	0.001	HOMO(α)→LUMO+5(α) (28%) HOMO(β)→LUMO+6(β) (25%)

6				
S_1	675.2	14.8	0.000	HOMO(β)→LUMO(β) (79%)
S_2	592.6	16.9	0.003	HOMO-16(β)→LUMO(β) (35%) HOMO-15(β)→LUMO(β) (12%) HOMO-6(β)→LUMO(β) (22%) HOMO-5(β)→LUMO(β) (13%)
S_3	577.0	17.3	0.000	HOMO-17(β)→LUMO(β) (10%) HOMO-12(β)→LUMO(β) (22%) HOMO-7(β)→LUMO(β) (14%) HOMO-1(β)→LUMO(β) (22%)
S_4	537.1	18.6	0.000	HOMO(α)→LUMO(α) (43%) HOMO(β)→LUMO+1(β) (43%)
S_5	530.9	18.8	0.000	HOMO-13(β)→LUMO(β) (21%) HOMO-11(β)→LUMO(β) (49%)
S_6	467.8	21.4	0.000	HOMO-19(β)→LUMO(β) (13%) HOMO-17(β)→LUMO(β) (15%) HOMO-10(β)→LUMO(β) (37%) HOMO(β)→LUMO(β) (15%)
S_7	409.0	24.4	0.000	HOMO-2(α)→LUMO(α) (25%) HOMO-1(β)→LUMO+1(β) (24%)
S_8	382.9	26.1	0.331	HOMO(α)→LUMO(α) (47%), HOMO(β)→LUMO+1(β) (46%)
S_9	374.9	26.7	0.000	HOMO-2(α)→LUMO(α) (17%) HOMO(α)→LUMO+2(α) (21%) HOMO-1(β)→LUMO+1(β) (17%) HOMO(β)→LUMO+3(β) (23%)
S_{10}	367.9	27.2	0.000	HOMO-1(α)→LUMO(α) (92%)
S_{11}	358.9	27.9	0.000	HOMO-12(β)→LUMO(β) (14%) HOMO-1(β)→LUMO(β) (64%)
S_{12}	353.1	28.3	0.000	HOMO-3(α)→LUMO+1(α) (38%) HOMO-2(β)→LUMO+2(β) (37%)
S_{13}	336.9	29.7	0.054	HOMO-5(β)→LUMO(β) (79%)
S_{14}	331.6	30.2	0.000	HOMO-3(β)→LUMO(β) (79%) HOMO-1(β)→LUMO(β) (10%)
S_{15}	326.7	30.6	0.000	HOMO-4(β)→LUMO(β) (27%) HOMO-2(β)→LUMO(β) (61%)
S_{16}	323.6	30.9	0.000	HOMO-5(α)→LUMO(α) (13%) HOMO(α)→LUMO+3(α) (22%) HOMO-3(β)→LUMO+1(β) (11%) HOMO(β)→LUMO+4(β) (25%)
S_{17}	319.6	31.3	0.000	HOMO-4(β)→LUMO(β) (69%)
S_{18}	314.8	31.8	0.000	HOMO-5(α)→LUMO(α) (12%) HOMO(α)→LUMO+3(α) (10%) HOMO-3(β)→LUMO+1(β) (11%) HOMO(β)→LUMO+3(β) (12%) HOMO(β)→LUMO+4(β) (11%)
S_{19}	310.0	32.3	0.189	HOMO-2(α)→LUMO(α) (42%) HOMO-1(β)→LUMO+1(β) (42%)
S_{20}	304.0	32.9	0.000	HOMO-4(α)→LUMO+1(α) (38%)

				HOMO-4(β)→LUMO+2(β) (37%) HOMO(β)→LUMO+2(β) (13%)
S_{21}	301.9	33.1	0.066	HOMO(α)→LUMO+2(α) (38%) HOMO(β)→LUMO+3(β) (35%)
S_{22}	295.0	33.9	0.036	HOMO(β)→LUMO+2(β) (72%)
S_{23}	291.9	34.3	0.016	HOMO(α)→LUMO+1(α) (82%)
S_{24}	285.1	35.1	0.000	HOMO-5(α)→LUMO+2(α) (12%) HOMO-2(α)→LUMO+2(α) (11%) HOMO-3(β)→LUMO+3(β) (12%)
S_{25}	276.5	36.2	0.000	HOMO-5(β)→LUMO+1(β) (91%)

3.6.4 Optimized structure of 7-9

Geometry optimization of binuclear complexes has been performed using the Gaussian 09 with the level of B3LYP basis set [49]. The optimized structures of complexes **7-9** are shown in Fig. 79-81. There are slight differences in bond parameters, owing to the theoretical calculations were carried out on an isolated molecule in the gas phase [111-1114]. Distortion index τ_5 was also estimated [84, 115]. Based on the distortion index, the geometry around the copper centre is distorted square pyramidal. These observations are in the same line of single-crystal X-ray analysis. The computed structural parameters of these complexes **7-9** agree with those single-crystal X-ray analysis parameters.

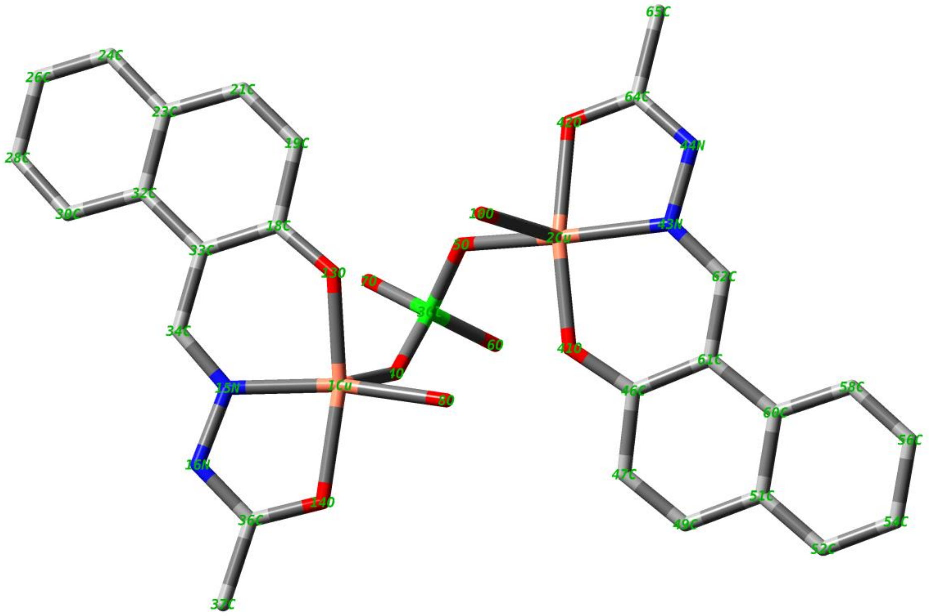

Fig. 79. Optimized structure of complex **7**.

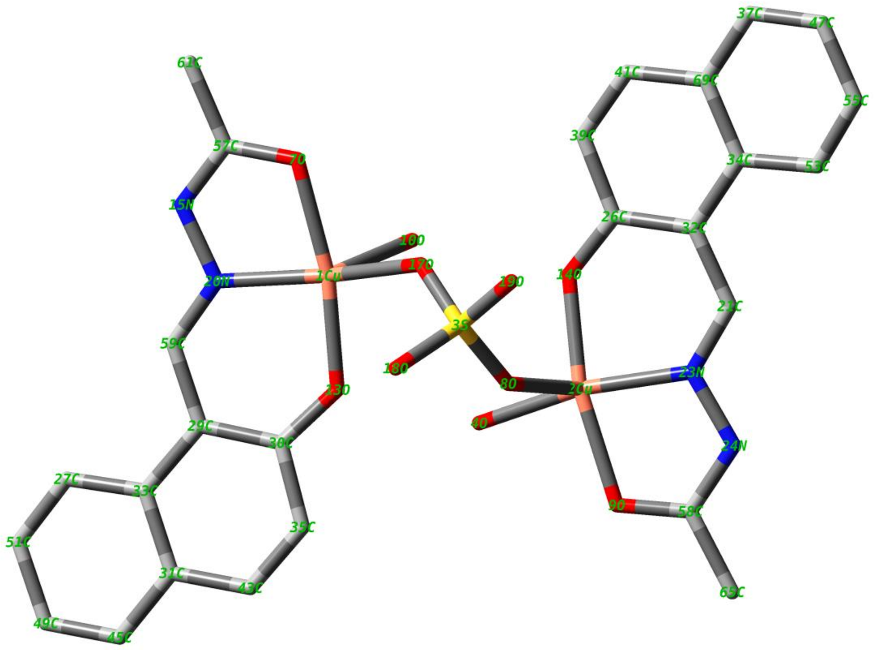

Fig. 80. Optimized structure of complex **8**.

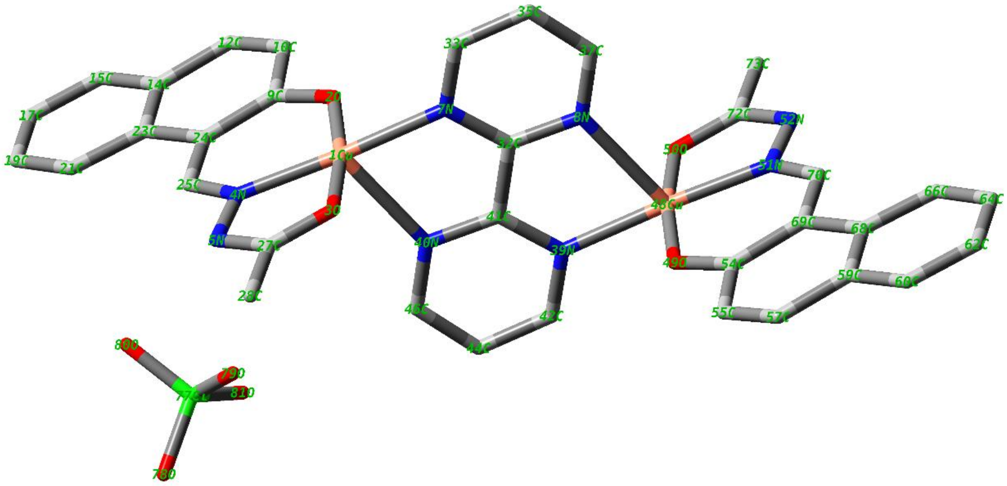

Fig. 81. Optimized structure of complex **9**.

3.6.5 HOMO-LUMO analysis and electronic properties of 7-9

The geometrical parameters *viz*., optimized energies, frontier molecular orbitals and HOMO and LUMO energy gap have been computed (Table 14) at the B3LYP6-31G(d)/LANL2DZ levels using the Gaussian 09 computer program. The plots of HOMO and LUMO are shown in Fig. 82-84. In complex **7** and **8** LUMO is predominantly localized on copper centers and frontier molecular orbitals on tridentate hydrazone ligand (Fig. 83 and 84). In complex **9**, HOMO and LUMO are localized on tridentate hydrazone and bridging ligand (Fig. 84). The FMO (HOMO and LUMO) are used to describe electron donors and acceptors descriptors. These descriptors decide the biological activity of molecules [130].

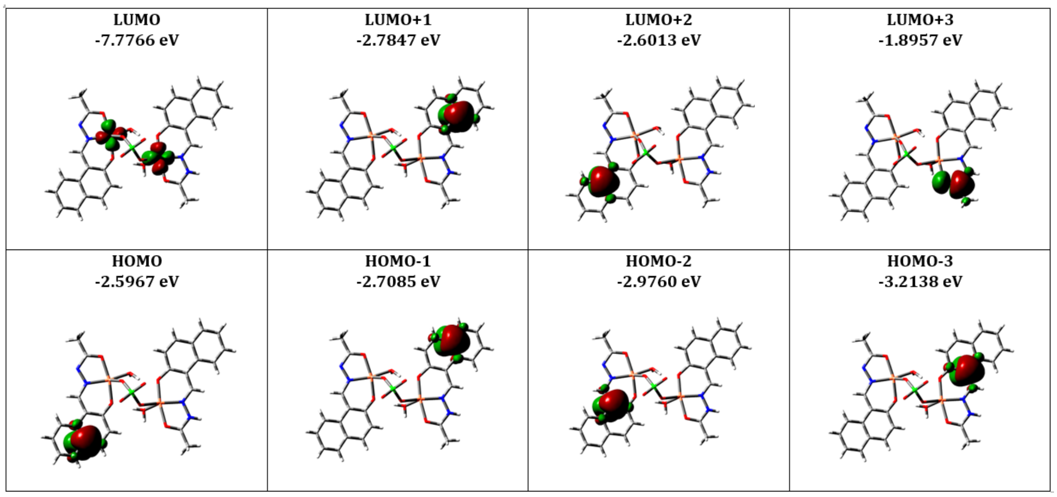

Fig. 82. HOMO-LUMO energy level diagram of complex **7**.

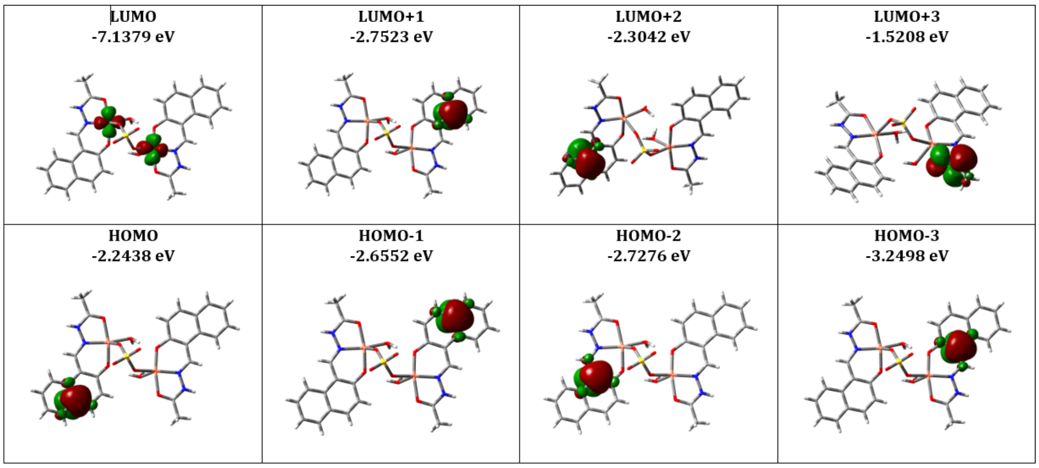

Fig. 83. HOMO-LUMO energy level diagram of complex **8**.

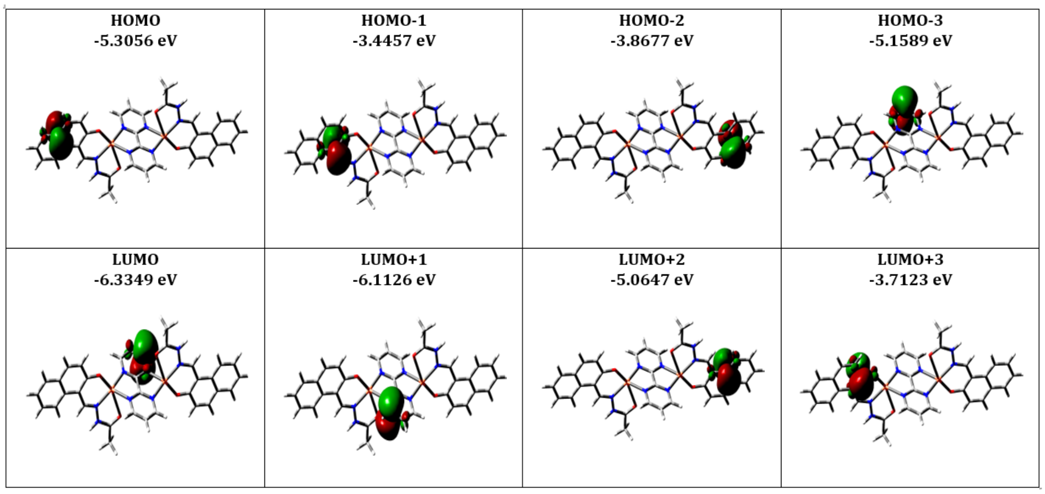

Fig. 84. HOMO-LUMO energy level diagram of complex **9**.

The spin density plots of binuclear complexes **7-9** are shown in Fig. 85-87. On perusal of the plots, it is clear that there is a considerable amount of distribution of spin into the donor atom of tridentate hydrazone ligand, bridging ligand and also on copper centres. It is obvious from the spin density plots that the overlap between the $d_{x^2-y^2}$ of copper atom and the hybrid orbital of the bridging oxygen atoms. Therefore, spin delocalization of the bridging group contributes the antiferromagnetic interactions.

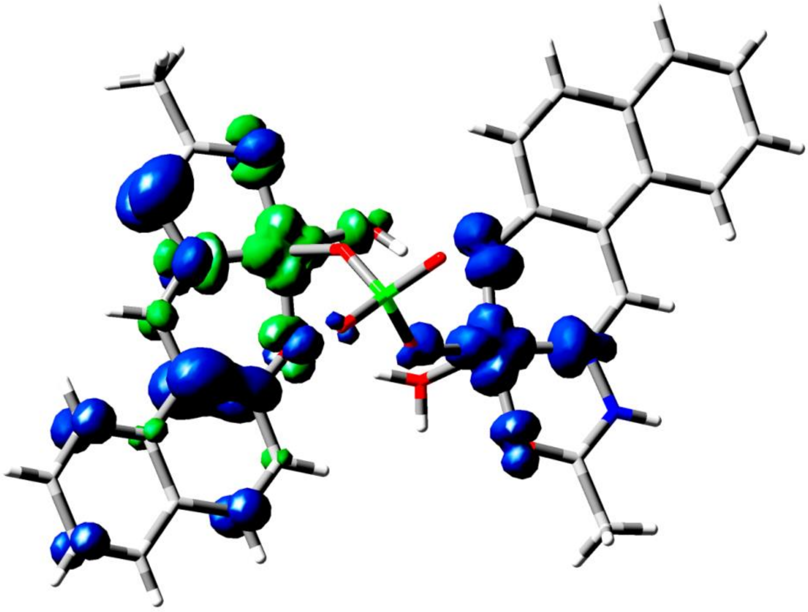

Fig. 85. The spin density of complex **7** with 0.0004 iso value.

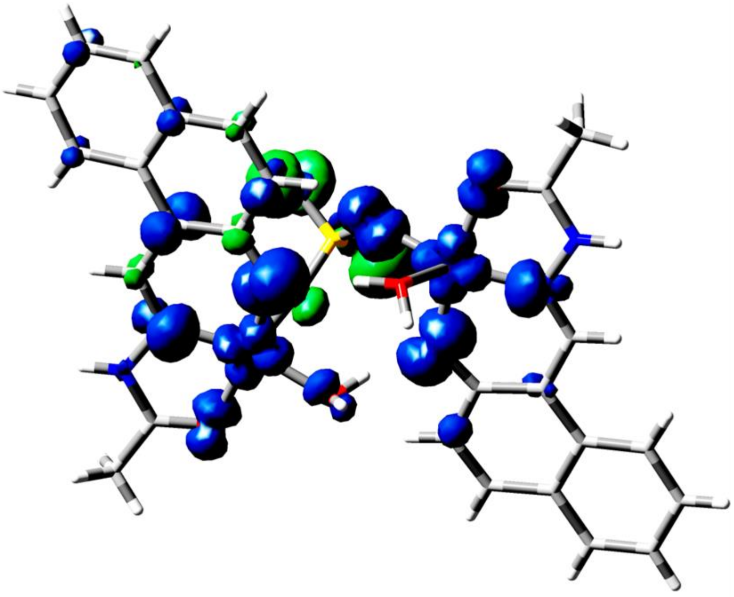

Fig. 86. The spin density of complex **8** with 0.0004 iso value.

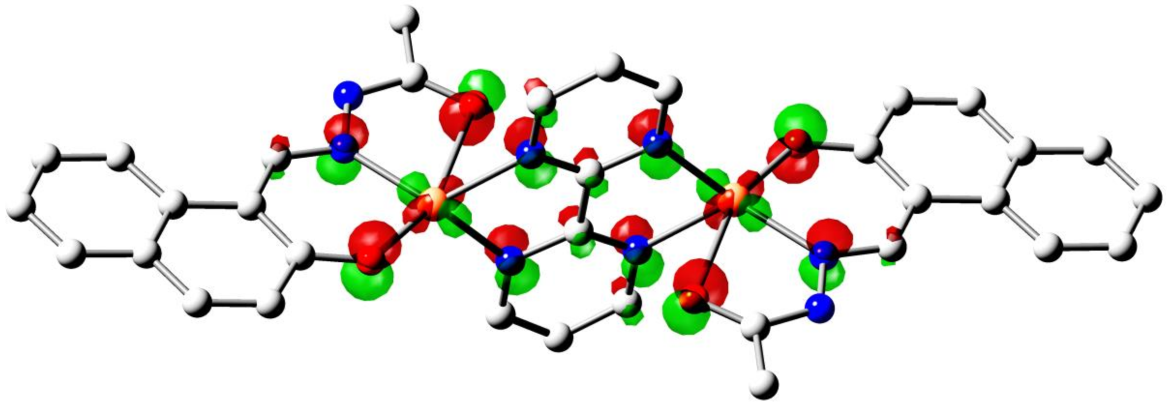

Fig. 87. The spin density of complex **9** with 0.0004 iso value.

The electronic structures of the complexes **7-9** by characterized by analyzing the highest occupied molecular orbital (HOMO) and lowest unoccupied molecular orbitals (LUMO). The HOMO-LUMO energy gaps (ΔE) furnish information about the reactivity and nature (soft or hard) of a given molecule. These HOMO and LUMO energies are negative for all complexes, indicating that the complexes are stable [116]. The ΔE also predicts the various reactivity parameters, which additionally reveal the internal charge transfer, susceptibility and stability of molecules [118-120, 131]. These reactivity parameters are collected with their mathematical definition in Table 14. The variations in parameters are due to the structural variation of the complexes.

Table 14 The crucial electronic parameters for complexes **7-9**.

Molecular Descriptors	Mathematical descriptors	7	8	9
E_{HOMO} (eV)	Energy of HOMO	-7.7766	-2.2438	-6.3349
E_{LUMO} (eV)	Energy of LUMO	-2.5967	-7.1379	-5.3056
Energy gap (eV)	$\Delta E = E_{HOMO} - E_{LUMO}$	5.1799	4.8941	1.0293
Ionization potential (eV)	$I = -E_{HOMO}$	7.7766	2.2438	6.3349
Electron affinity (eV)	$EA = -E_{LUMO}$	2.5967	7.1379	5.3056
Electronegativity (eV)	$\chi = (I+EA)/2$	5.1866	4.6908	5.8202
Chemical potential (eV)	$\mu = -\chi$	-5.7866	-4.6908	-5.8202
Global hardness (eV)	$\eta = (I-EA)/2$	2.5899	-2.4470	0.5146
Softness (eV)$^{-1}$	$S = 1/2\eta$	0.1990	-0.2043	0.9715
Electrophilicity index	$\omega = \mu^2/2\eta$	6.4643	-4.4960	32.9104
Electron donating capacity	$\omega- = (3E_{HOMO} + E_{LUMO})^2 / 16(E_{HOMO} - E_{LUMO})$	8.1104	2.4565	35.8855
Electro accepting capacity	$\omega+ = (E_{HOMO} + 3E_{LUMO})^2 / 16(E_{HOMO} - E_{LUMO})$	2.9238	7.1473	30.065

3.7 Magnetic moment

Room temperature magnetic moments of all complexes **1-9** were measured on a Gouy Balance. The magnetic moments of are 1.79, 1.78, 1.80 and 1.76 B.M. for **1**, **2**, **3** and **4**, respectively. The magnetic moment value of **4** is slightly less than the spin-only value due to intermolecular spin-spin interaction in the solid-state. Although the molecular structures of **4** reveals the presence of copper(II) monomers, a close survey shows that such monomers have a close symmetry-related, neighbour that presents a close π···π (aryl-metal chelate ring) interactions (Fig 23). The magnetic moment values are similar to other mononuclear complexes [132-134].

The magnetic moments of **5** are 1.76 BM and 1.79 for **6**. The magnetic moment value of **5** is slightly less than the spin-only value due to intermolecular spin-spin interaction in the solid-state as such observations in X-band epr spectral studies due to antiferromagnetic nature in solid-state. The magnetic moment values are similar to other mononuclear complexes [132-134].

Magnetic moment values of binuclear complexes **7-9** have also been collected at room temperature. The observed magnetic moment values are 1.67, 1.69, 1.65 B.M. for **7**, **8** and **9** respectively. Such low values of this magnetic moment of these binuclear complexes are due to intramolecular interactions [135].

3.8 Electronic spectral study

The electronic spectra of mononuclear complexes **1-4** have been measured in DMSO solution (3.0×10^{-3}M). The electronic band positions are given in Table 15 and shown in Fig. 88. In each spectrum of these mononuclear complexes lower energy absorption in the visible region (λ_{max} = 503-506 nm) and higher energy absorption in the UV-region (λ_{max} = 337-341 nm) are to be expected due to ligand centre transitions [131]. The higher energy band can be attributed due to the $\pi \rightarrow \pi^*$ transition of the aromatic rings and azomethine group. The absorption bands in the visible region (503-506 nm) are attributed to a ligand-metal charge transfer (LMCT) associated with the nitrogen and oxygen donor atoms of phenoxy oxygen and azo nitrogen of ligand [136,137]. Electronic spectra of all complexes exhibit a *d-d* transition in the region 617-623 nm. The essential feature of this band suggests that it is the combination of three transitions (${}^2B_g \rightarrow {}^2A_{1g}$, ${}^2B_{1g} \rightarrow {}^2B_{2g}$ and ${}^2B_{1g} \rightarrow {}^2E_g$). Thus, it may be concluded that the copper(II) complexes have square-planar geometry.

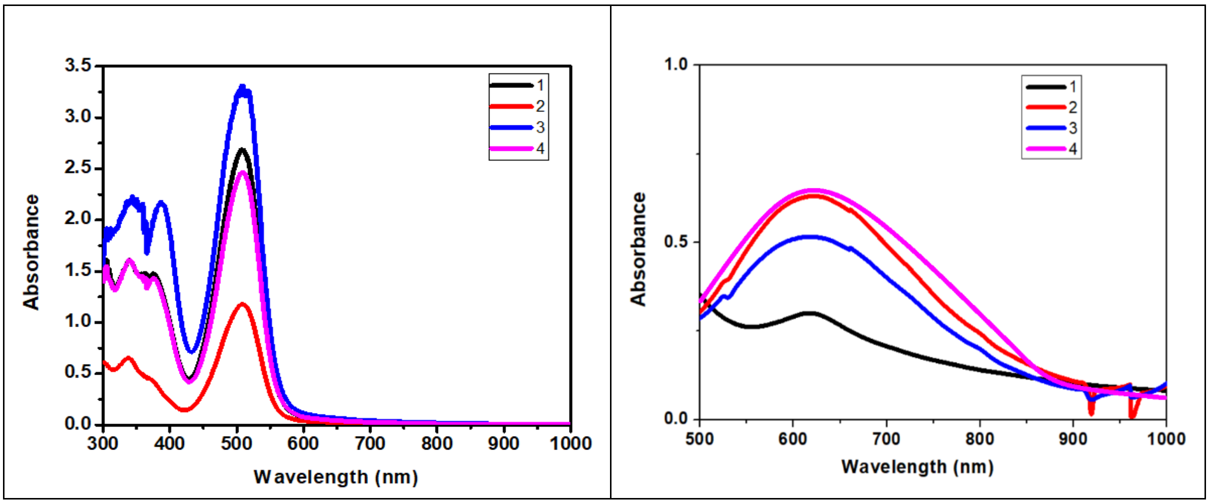

Fig. 88. Electronic spectra of complexes **1-4**.

Table 15 Electronic spectral transition (λ_{max}) for complexes **1-8**.

	λ_{max}(nm)		λ_{max}(nm)
Complexes	**π→π***	**LMCT**	***d-d* band**
1	338	503	617
2	340	504	621
3	341	505	623
4	337	506	620

The electronic spectra of both mixed ligand complexes **5** and **6** have been measured in the DMSO solution (3.0 × 10^{-3} M). The electronic band positions are given in Table 16 and the spectra are shown in Fig. 89 are shown. In each spectrum of these complexes lower energy absorption in the visible region λ_{max} = 325 for **5** and 339 nm for **6** and higher energy absorption in the UV-region (λ_{max} = 302-340 nm) is to be expected due to ligand center transitions [131]. The higher energy band can be attributed due to the π→π* transition of the aromatic rings and azomethine group. The absorption bands in the visible region (424-441nm) are attributed to a ligand-metal charge transfer (LMCT) associated with the nitrogen and oxygen donor atoms [131, 136-138]. Electronic spectra of both complexes exhibit a *d-d* transition in the region 765 and 640 nm for **5** and **6**, respectively [69]. For an octahedral copper(II) complex (d^9 system), the expected d-d band ($^2E_g \rightarrow ^2T_{2g}$) transition occurs at ~800 nm. A blue-shift of this band occurs when an octahedral geometry undergoes Jahn-Teller distortion to a distorted octahedral, square pyramidal, trigonal pyramidal, or square planar molecular structure. The *d-d* absorption band positions of both complexes are in good conformity of the solid-state molecular structures confirmed by single-crystal X-ray analysis.

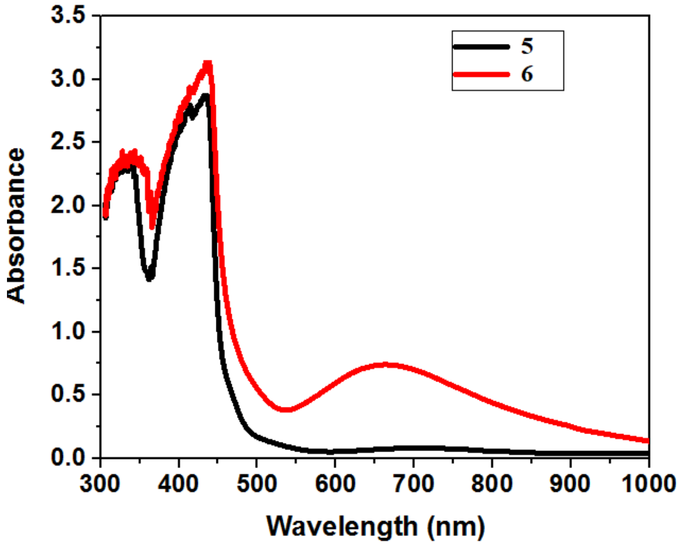

Fig. 89. Electronic spectra of complex **5** and **6**.

Table 16 Electronic spectral transition (λ_{max}) for complexes **5** and **6**.

Complex	λ_{max}(nm)		λ_{max}(nm)
	$\pi \rightarrow \pi^*$	LMCT	*d-d* band
5	325	424	764
6	339	441, 418	640

The electronic spectra of binuclear complexes **7-9** have been measured in DMSO solution (3.0 × 10^{-3}M). The electronic band positions are given in Table 17 and Fig. 90 are shown. In each spectrum of these binuclear complexes lower energy absorption in the visible region (λ_{max} = 403-419nm) and higher energy absorption in the UV-region (λ_{max} = 291-339 nm) are to be expected due to ligand centre transitions [131]. The higher energy band can be attributed due to the $\pi \rightarrow \pi^*$ transition of the aromatic rings and azomethine group. The absorption bands in the visible region (403-419 nm) are attributed to a ligand-metal charge transfer (MLCT) associated with the nitrogen and oxygen donor atoms [69,136-138]. Electronic spectra of all complexes exhibit a d-d transition in the region 660-709 nm [69].

Table 17 Electronic spectral transition (λ_{max}) for complexes **7-9**.

Complex	λ_{max}(nm)		λ_{max}(nm)
	$\pi \rightarrow \pi^*$	LMCT	*d-d* band
7	325	410	670
8	332	403	660
9	291, 339	419, 339	709

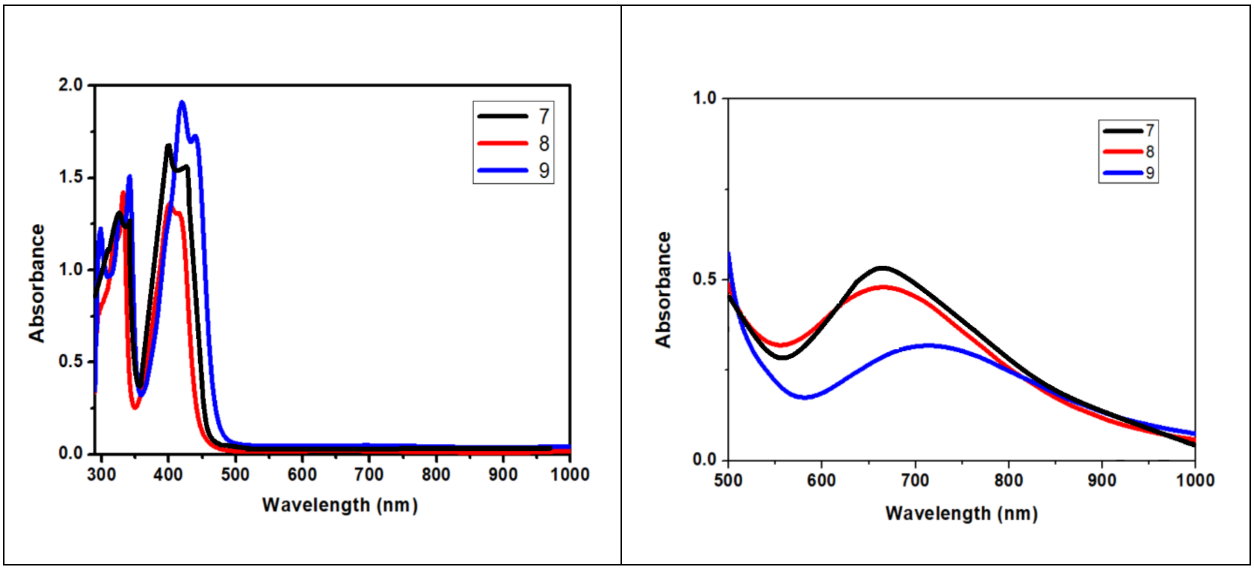

Fig. 90. Electronic spectra of complex 7-**9.**

3.9 Electrochemistry

The electrochemical properties of mononuclear complexes **1-4** have been explored using cyclic voltammetry (CV) and differential pulse voltammetry (DPV) at 100 mVs^{-1} scan rates in DMSO solution in presence of 0.1 M TBAP. The cyclic voltammograms and differential pulse voltammograms are shown in Fig. 91 and derived electrochemical parameters are summarized in Table 18.

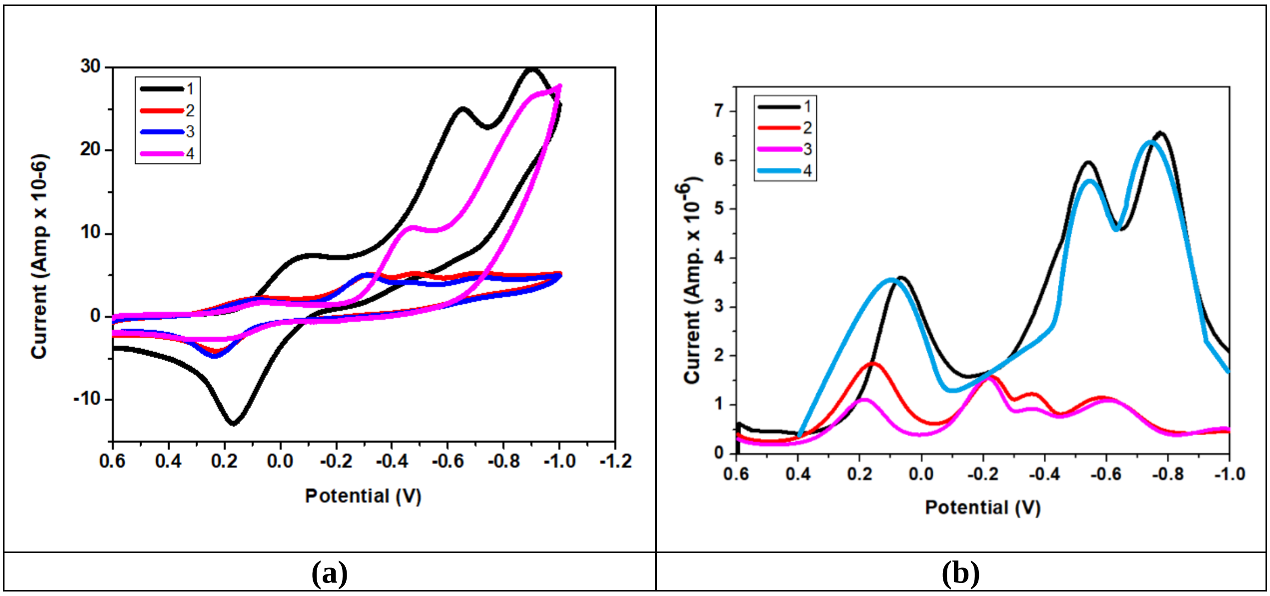

(a) **(b)**

Fig. 91. CV **(a)** and DPV **(b)** of complexes **1-4**.

Table 18 Electrochemical parameters of complexes **1-4**.

Complex	E_{pc1}	E_{pa1}	E_{pc2}	ΔEp	$E_{1/2}^{1}$	D_{pc1}	D_{pc2}	ΔD_{pc}
1	0.065	0.164	-0.652	0.099	0.114	0.065	-0.541	0.606
2	0.080	0.217	-0.321	0.137	0.148	0.162	-0.219	0.381
3	0.089	0.228	-0.304	0.139	0.158	0.185	-0.210	0.395
4	0.090	0.230	-0.331	0.140	0.160	0.187	-0.213	0.400

All of the complexes exhibit two reduction waves and one oxidation wave. The electrode reactions for mononuclear complexes **1-4** can be associated with the stepwise reduction of the Cu(II) centre.

$$Cu^{II} \overset{+1e^{-}}{\rightleftharpoons} Cu^{I} \overset{+1e^{-}}{\rightleftharpoons} Cu^{0}$$

All reduction waves are quasi reversible in nature (Table 18). The larger ΔE_p values also reveal that the reduction process is related ECE mechanism [139]. This could be a different coordination sphere of copper centre and flexibility of ligands. On increasing the scan rate, the peak heights increase linearly, approving the diffusion effect of the electrochemical mechanism [140]. The extra reduction peaks in cyclic voltammograms are due to the reduction of the Schiff base [141]. The DPV is the most appropriate technique used to resolve the reduction peaks with very small differences in peak positions [140]. This electrochemical technique supports the result of CV and is in agreement with the establishment of findings [141, 142].

An electrochemical property of mixed ligand complexes **5** and **6** have been explored using cyclic voltammetry (CV) and Differential pulse voltammetry (DPV). The cyclic voltammograms and differential pulse voltammograms are shown in Fig. 92 and derived electrochemical parameters are summarized in Table 19.

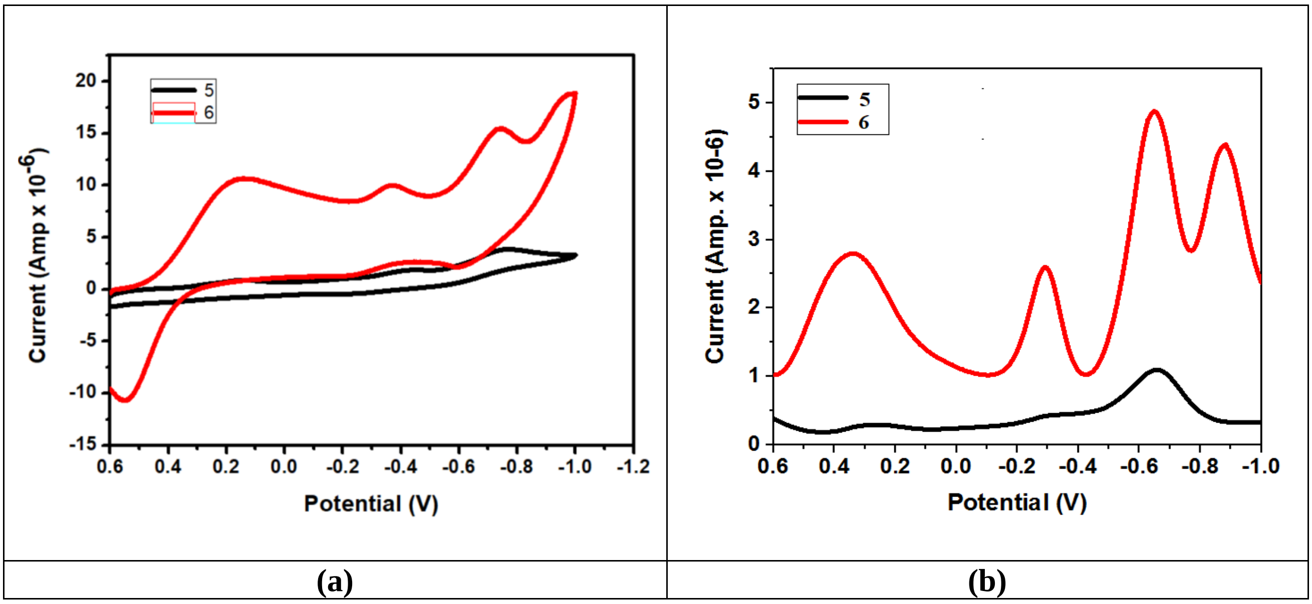

(a) **(b)**

Fig. 92. CV**(a)** and DPV**(b)** of complexes **5** and **6**.

Table 19 Electrochemical parameters of complexes **5** and **6**.

Complex	E_{pc1}	E_{pa1}	E_{pc2}	ΔEp	$E^{1}_{1/2}$	D_{pc1}	D_{pc2}	ΔD_{pc}
5	0.151	0.541	-0.363	0.390	0.346	-0.297	-0.639	0.352
6	0.084	+0.217	-0.468	0.133	0.150	-0.287	-0.654	0.367

Both of the complexes exhibit two reduction waves and one oxidation wave. The electrode reactions for both complexes can be associated with the stepwise reduction of the Cu(II) center.

$$Cu^{II} \overset{+1e^{-}}{\rightleftharpoons} Cu^{I} \overset{+1e^{-}}{\rightleftharpoons} Cu^{0}$$

All reduction waves are quasireversible irreversible in nature (Table 19). The larger ΔE_p values also reveal that the reduction process is related ECE mechanism [139]. In complexes **5** and **6** the value of ΔE is larger compared in complex **5** to other complexes. This could be a different coordination sphere of copper center and flexibility of ligands. On increasing the scan rate, the peak heights increase linearly, approving the diffusion effect of the electrochemical mechanism [140]. The extra reduction peaks in cyclic voltammograms are due to the reduction of the Schiff base [141]. The DPV is the most appropriate technique used to identify the reduction peaks with very small differences in peak positions [142]. These electrochemical techniques support the result of CV and is in agreement with the findings of CV [131, 141, 143]

Similarly, the electrochemical property of binuclear complexes **7-9** have been explored using cyclic volatammetery (CV) and differential pulse voltammetery (DPV). The cyclic voltammograms and differential pulse voltammograms are shown in Fig. 93 and derived electrochemical parameters are summarized in Table 20.

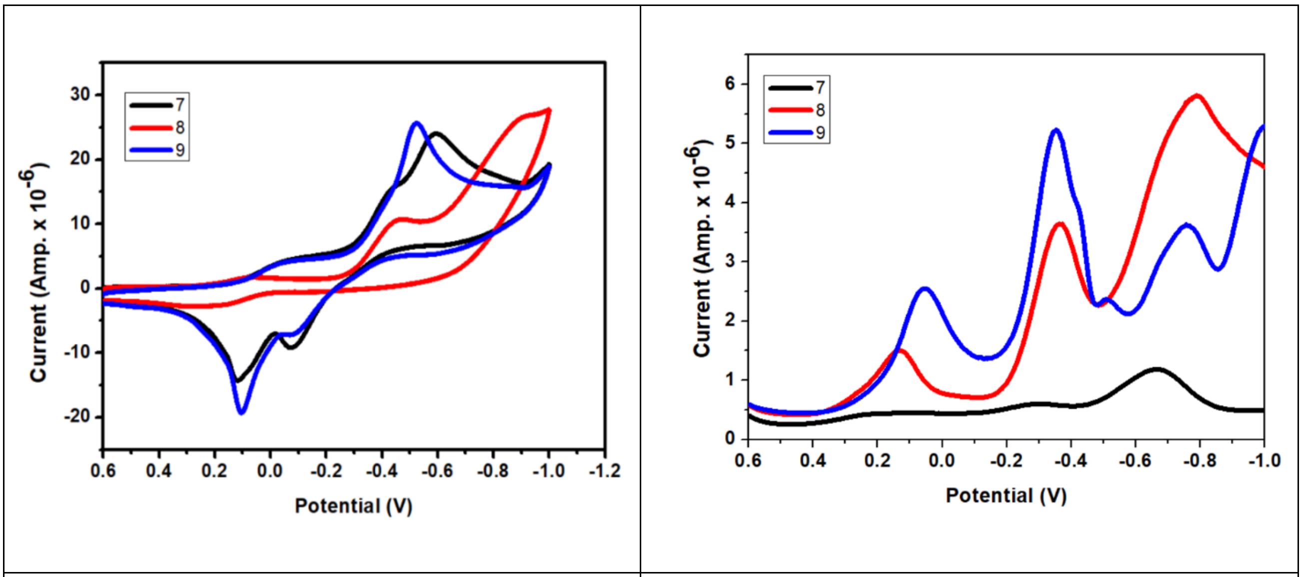

(a) **(b)**

Fig. 93. CV **(a)** and DPV **(b)** of complexes **7-9**.

Table 20 Electrochemical parameters of complexes **7-9**.

Complex	E_{pc1}	E_{pa1}	E_{pc2}	E_{pa2}	ΔEp	$E^{1}_{1/2}$	$E^{1}_{1/2}$	D_{pc1}	D_{pc2}	ΔD_{pc}	k_{con}
7	0.179	0.410	-0.443	-	0.231	0.294	-	-0.370	-0.785	0.415	-
8	0.084	0.218	-0.468	-	0.134	0.151	-	-0.369	-0.785	0.416	-
9	-0.436	0.112	-0.598	-0.074	0.548	-0.274	-0.336	-0.354	-0.754	0.400	11.163

All of the complexes exhibit two reduction waves and one oxidation wave except **9**. This shows two redox waves which are associated with the stepwise reduction of the Cu(II) centre

$$\mathrm{Cu^{II}Cu^{II}} \xrightleftharpoons{+1e^-} \mathrm{Cu^{I}Cu^{II}} \xrightleftharpoons{+1e^-} \mathrm{Cu^{I}Cu^{I}}$$

Whereas binuclear complexes **7** and **8** are related to the one-step reduction of Cu(II) centers.

$$\mathrm{Cu^{II}Cu^{II}} \overset{+2e^{-}}{\rightleftharpoons} \mathrm{Cu^{I}Cu^{I}}$$

The conproportionation constant for the electrode reaction is given as:

$$\mathrm{Cu^{II}Cu^{II}} + \mathrm{Cu^{I}Cu^{I}} \overset{k_{con}}{\rightleftharpoons} 2\,\mathrm{Cu^{II}Cu^{I}}$$

$k_{con}$was also evaluated using the relationship log $k_{con} = 16.9\ (\Delta E_{1/2})$.

All reduction waves are quasi reversible in nature. The larger ΔE_p values also reveal that the reduction process is related ECE mechanism [139]. In complex **9** the value of ΔE is larger compared to **7** and **8** complexes. This could be a different coordination sphere of copper centre and flexibility of ligands. On increasing the scan rate, the peak heights increase linearly, approving the diffusion effect of the electrochemical mechanism [140]. The extra reduction peaks in cyclic voltammograms are due to the reduction of Schiff base [78]. The DPV is the most appropriate technique used to resolve the reduction peaks with very small differences in peak positions [142]. The electrochemical technique supports the result of CV and agrees with the formation of findings [78, 131].

3.10 EPR spectra

To confirm the paramagnetic nature of these complexes (**1-9**), X-band electron paramagnetic measurements were performed at room temperature (RT) of polycrystalline samples and liquid nitrogen temperature (LNT) of liquid solutions. Epr techniques are a sensitive spectroscopic technique for the investigation of the coordination sphere of paramagnetic metal centers such as Cu^{2+}, Fe^{3+}, $V(O)^{2+}$, Mn^{2+} in metal complexes. The Cu^{2+} ion has an effective spin S = ½ and nuclear spin I = 3/2 and allows the detection of hyperfine lines. The techniques are also used to get information about the nature of the ground state of Cu^{2+} ions, covalency of the bonding between the copper 3d orbital and ligand orbitals along with information about tetrahedral distortion in paramagnetic complexes [144].

The Epr spectra of all mononuclear (**1-4**) complexes were recorded in polycrystalline samples at RT and in DMSO solution (3.0×10^{-3} M) at LNT (Fig. 94-97). The room temperature (RT) spectra of polycrystalline samples (**1-4**) show typical axial type epr spectra. The polycrystalline spectra showed, two bands are observed corresponding to the transition $\Delta M_s = \pm 2$ with defined $g_{\parallel}$ and $g_{\perp}$ values (Table 21). The exchange parameter (G), which is a measure of the exchange interaction between the two copper centres in these polycrystalline samples, is evaluated using the equation $G = \frac{g_{\parallel}-2.0023}{g_{\perp}-2.0023}$ for axial spectra [135, 145]. If the value of G is less than **4** (G < 4.0) substantial exchange interaction is shown in the polycrystalline complex [146-149]. The estimated G value of **1-4** was 3.922, 3.825, 3.980 and 3.738 respectively. These values indicate that there is an exchange interaction (pseudo-dipole-dipole interaction) between the copper centres. The polycrystalline spectra of complexes have the characteristics display of a triplet state (*S* = 1) spectrum, indicating spin-spin interactions (pseudo-dipole-dipole interactions). A weak $\Delta M_S = \pm 2$ transition has appeared at ~1580 G. The presence of a half-field signal is characteristic of the interaction of two paramagnetic centres. In **2** and **4** $\Delta M_s = \pm 2$ signals is strong compared to **1** and **3**. The analysis of the spectrum yields $g_{\parallel} = 2.217$, $g_{\perp} = 2.059$ and D = 0.022 cm^{-1} for **2** and $g_{\parallel} = 2.218$, $g_{\perp} = 2.060$ and D = 0.021 cm^{-1} for **4**. The frozen solution (77K) epr spectra of **1** and **3** complexes exhibit the common pattern for mononuclear copper(II) complexes whereas complex **2** shows two signals due to the presence of two monomeric (pseudo-intermolecular dimer units) of this complex[150-152]. These dimer units are closely associated due to pseudo intermolecular dimers association. The dimeric arrangement of this complex is slightly due to a monomeric constituent and the resultant epr spectrum is due to mixed species, judging from the broad feature after $g_{\perp}$ region. Therefore, in the $g_{\parallel}$the region, two types of components are observed. The obtained epr parameters ($g_{\parallel}$, $A_{\parallel}$and$g_{\perp}$) are collected in Table 21. Similar observations have already been reported in copper(II) binary complexes [152, 153].

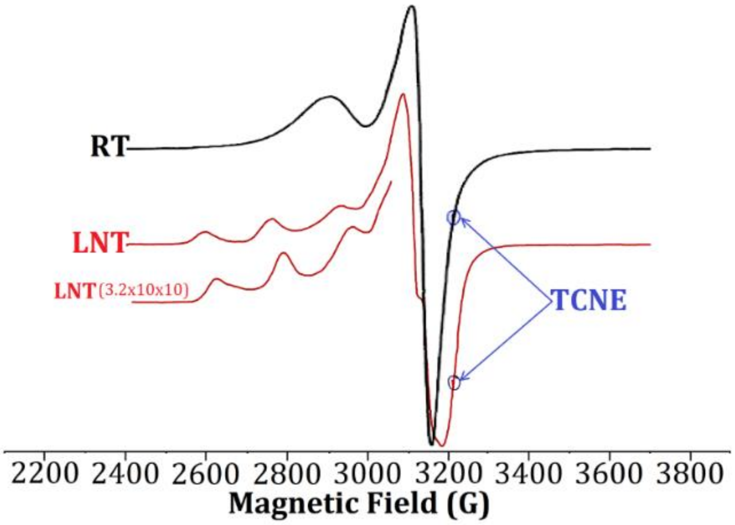

Fig. 94. EPR spectra of complex **1.**

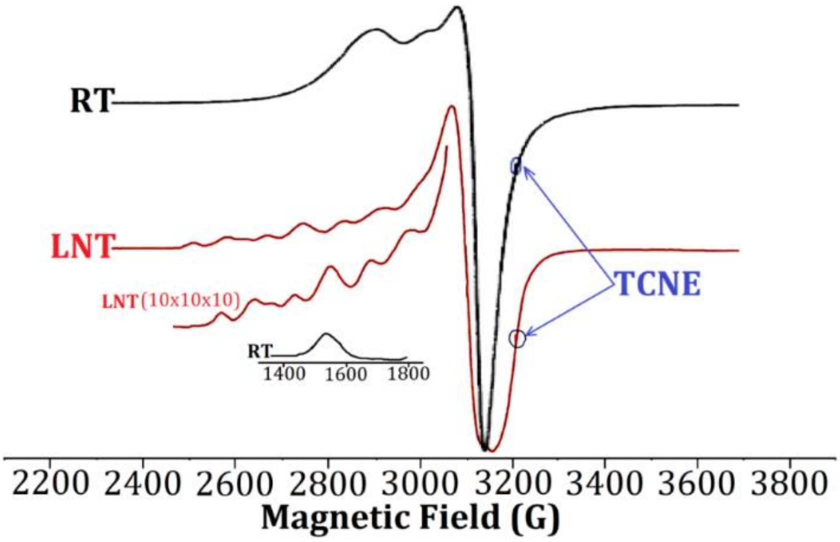

Fig. 95. EPR spectra of complex **2.**

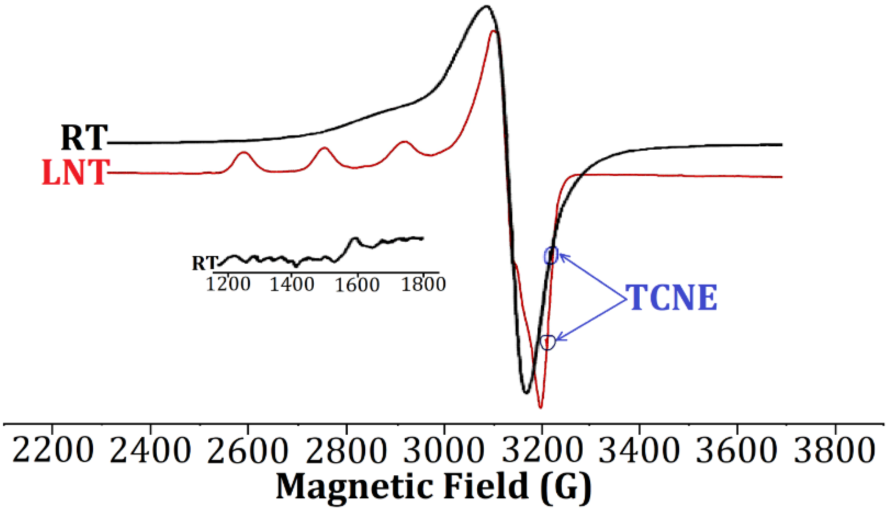

Fig. 96. EPR spectra of complex **3.**

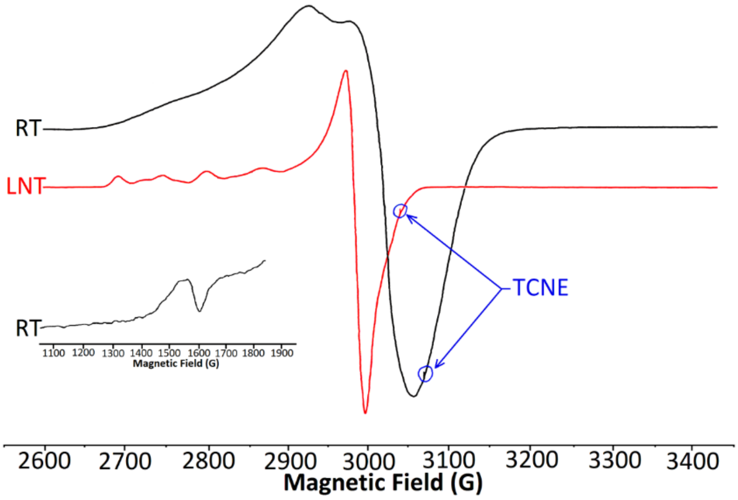

Fig. 97. EPR spectra of complex **4**.

The spin-Hamiltonian parameters evaluated from the epr spectra and the energies of *d-d* transitions from electronic spectra were used to calculate the bonding parameters α^2, β^2 and γ^2. The coefficient which represents the in-plane σ-bond strength (α^2), in-plane π-bonds (β^2) and out of plane π-bond (γ^2) are regarded as measures of covalency [154]. The value of in-plane σ-bonding parameter α^2 was calculated from the following equation [155].

$$\alpha^2 = A_{\parallel} / 0.036 + (g_{\parallel} - 2.00277) + 3 / 7\ (g_{\perp} - 2.00277) + 0.04$$

Similarly, orbital reduction factors ($K_{\parallel}$ and $K_{\perp}$) and in-plane π bonding and out of plane π bonding parameters were estimated using the following simplified equations [156]:

$$K_{\parallel}{}^2 = (g_{\parallel} - 2.00277) / E_{d\text{-}d} / 8\ \lambda_0$$

$$K_{\parallel} = \alpha^2\beta^2$$

$$K_{\perp}{}^2 = (g_{\perp} - 2.00277) / E_{d\text{-}d} / 2\ \lambda_0$$

$$K_{\perp}{}^2 = \alpha^2\gamma^2$$

where λ_0 = electron spin-orbital coupling constant

For pure σ bonding, $K_{\parallel} \sim K_{\perp} \sim 0.77$, for in-plane π bonding, $K_{\parallel} < K_{\perp}$; while for out-of-plane π bonding $K_{\parallel} > K_{\perp}$ [157]. In complexes **1** and **2** it is found that $K_{\parallel} < K_{\perp}$ which reveals the presence of significant in-plane π bonding. Additionally, the values of bonding parameters α^2, β^2 and γ^2 < 1.0 (value of 1.0 for 100% ionic nature) reveal the covalent nature of bonding between copper and ligand orbitals. Our data also indicate that the in-plane σ-bonding slightly decreases for species that are formed on the dissociation of complexes. The empirical factor $f = g_{\parallel} / A_{\parallel}$ (cm^{-1}) is an indicator of tetrahedral distortion. The values of *f* of remains in the range 144-177 cm analogous to a copper center with significant distortion [158, 159].

Table 21 EPR parameters of copper(II) complexes **1-4**.

EPR Parameters	**1**	**2**	**3**	**4**
Polycrystalline State (298 K)				
$\mathbf{g}_{\parallel}$	2.209	2.217	2.224	2.218
$\mathbf{g}_{\perp}$	2.055	2.059	2.058	2.060
G	4.055	3.825	3.980	3.738
D(cm^{-1})	3.922	0.022	0.027	0.021
Frozen Solution in DMSO (77K)				
$\mathbf{g}_{\parallel}$(**1**)	2.231	2.277	2.224	2.275

$\mathbf{g}_{\parallel}(\mathbf{2})$	-	2.240	-	2.238
$\mathbf{g}_{\perp}$	2.063	2.073	2.054	2.074
$\mathbf{A}_{\parallel}$(G) (1)	165	165	165	163
$\mathbf{A}_{\parallel}$(G) (2)	-	160	-	158
$\gamma^2(\mathbf{1})$	1.088	0.962	0.902	0.893
$\gamma^2(\mathbf{2})$	-	1.025	-	0.950
$\beta^2(\mathbf{1})$	1.037	0.937	0.918	1.059
$\beta^2(2)$	-	0.930	-	1.050
$\alpha^2(\mathbf{1})$	0.721	0.818	0.746	0.761
$\alpha^2(\mathbf{2})$		0.768		0.716
$\mathbf{K}_{\parallel}(\mathbf{1})$	0.748	0.767	0.685	0.806
$\mathbf{K}_{\parallel}(\mathbf{2})$	-	0.714	-	0.762
$\mathbf{K}_{\perp}$	0.785	0.787	0.673	0.824
f (cm)	145	148, 145	144	148, 152

The X-band electron paramagnetic resonance (epr) spectra of mixed complexes **5** and **6** in the microcrystalline powder sample at room temperature (RT) and frozen solution (77K) have been recorded shown in Fig. 98-99 and the derived experimental epr parameters are presented in Table 22.

The spectra of complexes **5** and **6** show a typical axial one with well defined $g_{\parallel}$ and $g_{\perp}$ values at 2.219 and 2.063 for **5** and 2.68 and 2.050 for **6**, respectively. The geometrical exchange parameter G, is 3.10 for **5** and 3.495 for **6**, indicates that the local tetragonal axis is misaligned [111, 112]. A strong half-field ($\Delta M_s = \pm 2$) is seen at 1568 G in epr spectrum **5** whereas it is weak in **6**. The presence of a half-field signal indicating the interaction of two copper(II) centers through anti-ferromagnetic coupling (S = 2) and shows a non-negligible value for zero-field splitting(D) [113]. The analysis of the epr spectrum of **5**complex gives $g_{\parallel}$= 2.219, $g_{\perp}$= 2.063 and D = 0.017 cm^{-1} and for **6** $g_{\parallel}$= 2.168, $g_{\perp}$= 2.050 and D = 0.024 cm^{-1}.

The frozen solution spectra of complex **5** showed two types of $g_{\parallel}$ features (2.261$g_{\parallel}$(1)& 2.31$g_{\parallel}$(2)). These features are the usual pattern for mononuclear copper(II) complexes due to the close association of two monomeric (pseudo-intermolecular dimers) units [149, 150]. Such epr features are not observed in the frozen solution spectra of complex **5**. The spectrum of complex **6** is well resolved with $g_{\parallel}$, $g_{\perp}$and $A_{\parallel}$. Moreover, the spectral observation that $g_{\parallel}$> $g_{\perp}$> 2.0023, reveals that the unpaired electron is in the $d_{x^2-y^2}$orbital of copper(II) ion and spectral behavior are characteristic of axial symmetry [151, 152].

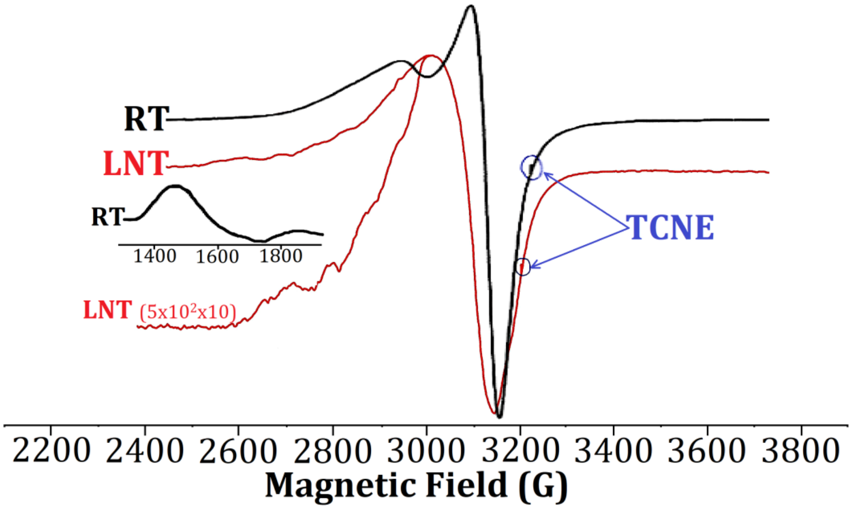

Fig. 98. EPR spectra of complex **5.**

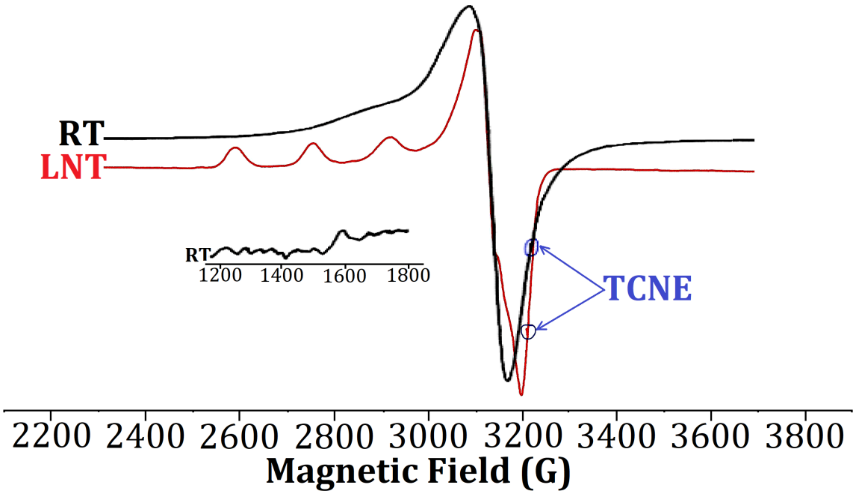

Fig. 99. EPR spectra of complex **6**.

The bonding parameters of both complexes are estimated and given in Table 22. Other related bonding parameters were also calculated and shown in Table 22. These are similar to reported copper(II) complexes [152, 153]. The value of α^2, β^2 and γ^2 show a significant in-plane π-bonding and in-plane σ-bonding. The empirical factor *f* (= $g_{\parallel}/A_{\parallel}(cm^{-1})$) can be taken as a diagnostic parameter of the stereochemistry of the paramagnetic complexes. The range of *f* value for distorted tetrahedral is 105-135 cm [154].

Table 22 EPR parameters of copper(II) complexes **5** and **6**.

EPR Parameters	5	6
Polycrystalline State (298 K)		
$g_{\parallel}$	2.219	2.168
$g_{\perp}$	2.063	2.050
G	3.100	3.495
D(cm^{-1})	0.017	0.24
Frozen Solution in DMSO (77K)		
$g_{\parallel}$(1)	2.261	2.214
$g_{\parallel}$(2)	2.231	-
$g_{\perp}$	2.074	2.055
$A_{\parallel}$(G) (1)	145	168
$A_{\parallel}$(G) (2)	135	
γ^2(1)	1.057	0.905
γ^2(2)	1.142	
β^2(1)	0.992	0.893
β^2(2)	1.009	
α^2(1)	0.751	0.745
α^2(2)	0.695	
$K_{\parallel}$(1)	0.745	0.665
$K_{\parallel}$(2)	0.701	
$K_{\perp}$	0.794	0.674
***f* (cm)**	174, 177	141
λ_{max}(nm)	765	640

The X- band epr spectra at RT of binuclear copper(II) complexes **7**, **8** and **9** in the polycrystalline state and frozen DMSO solution are shown in Fig. 100-102. The experimentally derived epr parameters are given in Table 23. The polycrystalline spectra of **7** is broad and show evidence of strong half-field ($\Delta M_s = \pm 2$) with two broad epr hyperfine lines in $g_{\parallel}$ region. No hyperfine features can be resolved on the zero-field forbidden ($\Delta M_s = \pm 2$) signal. Although the typical half-field signal at g ~ 4 is detected (Fig. 100) as expected for the forbidden transition ($\Delta M_s = \pm 2$) of a dimer, the more intense signal at g~2.20 is not typical for a triplet state [160] looking like the usual signals of exchanged-coupled extended compounds. The broad hyperfine lines are not well resolved, due to dipolar broadening with neighbouring spins. The g values ($g_{\parallel} = 2.284$, $g_{\perp} = 2.073$) and zero-field splitting parameter D (0.029 cm^{-1}) are consistent with other binuclear complexes [78, 161, 162]. Such g values appear plausible for a complex with square pyramidal coordination sphere and are similar to that deduced for similar copper(II) complexes [78, 161, 162]. The splitting in the “perpendicular” region is not seen in this complex which shows its origin as g-value anisotropy rather than half-field splitting. Such features in the polycrystalline state of **4** are familiar for magnetically coupled binuclear complexes. The presence of half-field forbidden $\Delta M_s = \pm 2$ signal in this complex is attributed to the presence of a binuclear structure with an antiferromagnetically coupling of two $S = ½$ paramagnetic copper(II) centre [149, 150].

Frozen solution spectrum of this complex is shown in Fig. 100. In this spectrum, two types of $g_{||}$ appeared. The experimentally derived epr parameters are presented in Table 23. Similar spectral behaviour, the presence of more than two species in organic or aqueous solution, one originating from their salvation and another from the dissolution of a dinuclear core, has already been reported in binuclear copper(II) complexes [163]. The obtained g values ($g_{||} > g_{\perp} > 2.0023$) are consistent with the $d_{x^2-y^2}$ ground state for copper(II) ions typically for square pyramidal coordination geometry [164].

The polycrystalline spectrum of complex **8** has the characteristic epr spectral appearance of a triplet state ($S = 1$) spectrum, suggesting spin-spin interactions Fig. 101. The X-band signals for this complex are somewhat broader than they are for the complex **7**. Also, $\Delta M_s = \pm 2$ forbidden zero field signal ($\Delta M_s = \pm 2$) could be appeared around ~1568 G. Although the $\Delta M_s = \pm 2$ signal is very weak. The $\Delta M_s = 1$ region begins at a field setting just slightly higher than the highest field $\Delta M_s = \pm 2$ forbidden transition.

Frozen solution epr spectrum of this complex is almost similar to that of complex **7**. No $\Delta M_s = \pm 2$ signal could be found around 1600 G for this complex. In the frozen solution, the binuclear arrangement of **8** is partially due to a monomeric component and the resultant epr spectrum is somewhat due to two mixed species, dividing from the sharp line at 3150 G. Accordingly, in the $g_{||}$ region, two types of $g_{||}$ spectral features are noticed. The experimental derived epr parameters $g_{||}$ (1 and 2) and A (1and 2) along with $g_{\perp}$ are presented in Table 23. This is suggestive of $S = ½$ systems with an axial symmetry and $d_{x^2-y^2}$ ground state [149, 164, 165].

The polycrystalline epr spectrum of complex **9**, is representative of magnetically coupled binuclear complexes [34] due to presence of a single isotropic signal at $g_{iso} = 2.055$. It is striking that no half field forbidden signal $\Delta M_s = \pm 2$ could be resulted around 1600 G. It is fascinating that such complexes do not show zero field forbidden signals. Reasonably very weak magnetic exchange interactions propagated by the bridging bpm ligand are present.

Frozen solution spectrum of this complex is shown in Fig. 102. In this spectrum no half-field signal could be observed at around 1600 G. The frozen solution epr spectrum of **9** reveals the usual pattern for mononuclear copper(II) complexes and exhibits two types of signals in $g_{\|}$ region due to presence of two different copper(II) coordination spheres, with parallel magnetic parameters of $g_{\|}(1) = 2.219$, $A_{\|}(1) = 163$ G and $g_{\|}(2) = 2.180$, $A_{\|}(2) = 160$ G, respectively. A similar observation, the presence of more than one species in organic solutions arising from the dissolution of a binuclear core, has already been detected in copper complexes [163]. Also the acquired g-value ($g_{\|} > g_{\perp} > 2.0023$) are expected with the $d_{x^2-y^2}$ ground state for copper(II) ions common for square pyramidal and square planar coordination geometry [164].

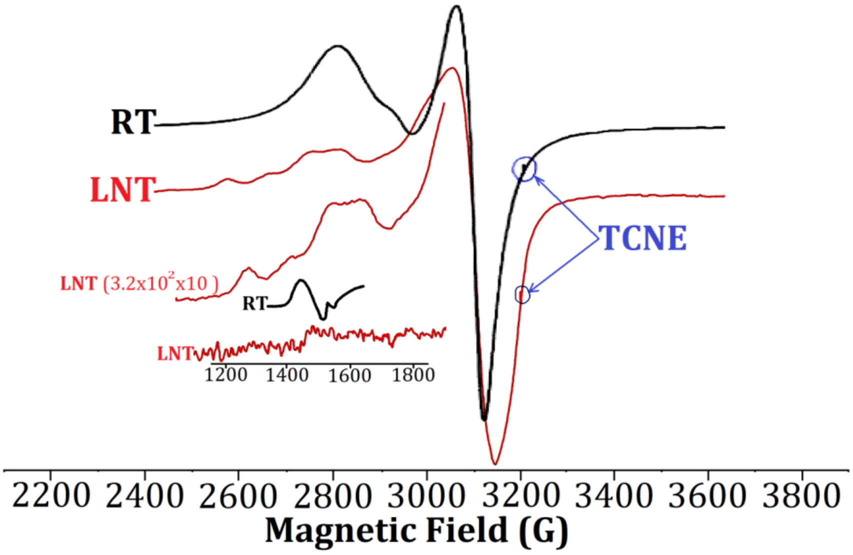

Fig. 100. EPR spectra of complex **7**.

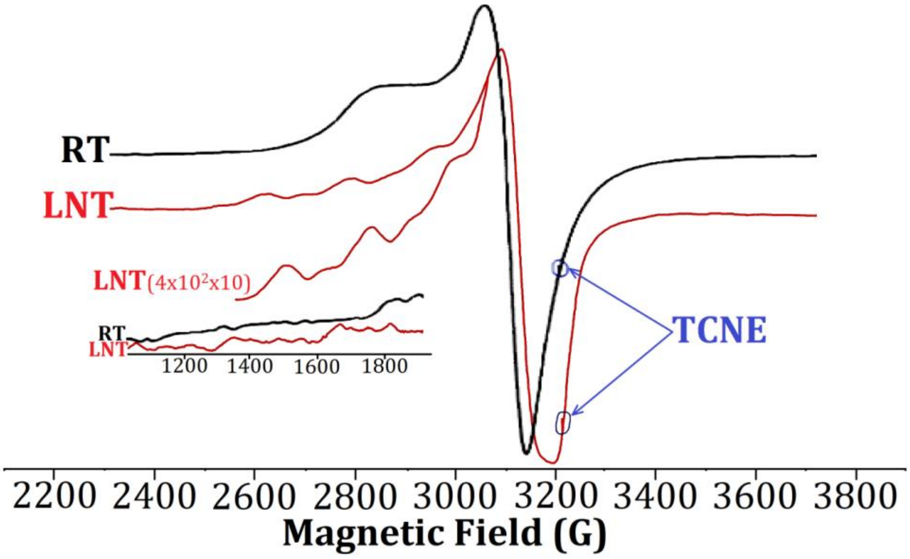

Fig. 101. EPR spectra of complex **8**.

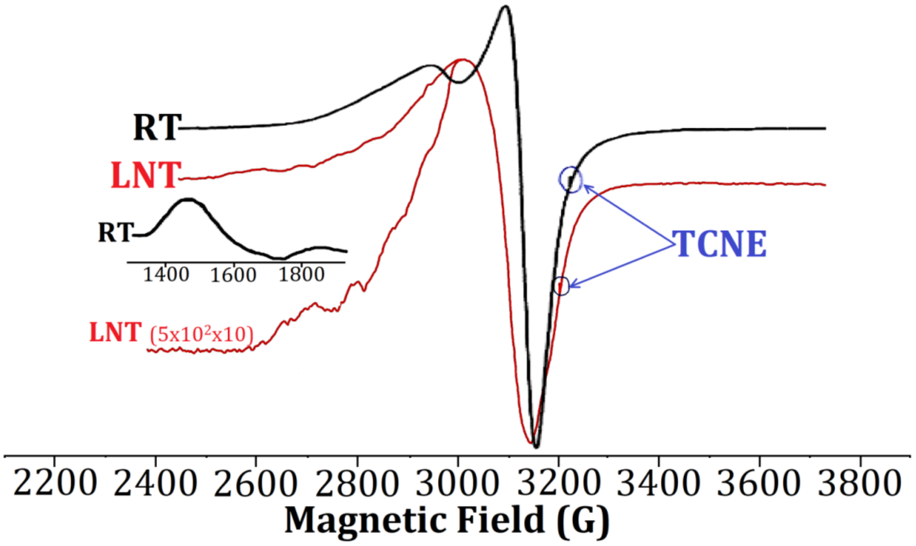

Fig. 102. EPR spectra of complex **9**.

Table 23 EPR parameters of binuclear copper(II) complexes **7-9.**

EPR Parameters	7	8	9
Polycrystalline State (298 K)			
$\mathbf{g}_{\parallel}$	2.284	2.258	
$\mathbf{g}_{\perp}$	2.073	2.069	
G	3.00	3.833	
D(cm^{-1})	0.029	0.027	0.028
Frozen Solution in DMSO (77K)			
$\mathbf{g}_{\parallel}$(**1**)	2.251	2.206	2.219
$\mathbf{g}_{\parallel}$(**2**)	2.213	2.179	2.180
$\mathbf{g}_{\perp}$	2.067	2.058	2.055
$\mathbf{A}_{\parallel}$(G) (1)	170	165	163
$\mathbf{A}_{\parallel}$(G) (2)	158	145	160
γ^2(**1**)	0.968	0.919	0.621
γ^2(**2**)	1.060	1.115	0.664
β^2(**1**)	0.941	0.866	0.925
β^2(2)	0.949	0.980	0.897
α^2(**1**)	0.799	0.732	0.737
α^2(**2**)	0.730	0.653	0.690
$\mathbf{K}_{\parallel}$(**1**)	0.752	0.686	0.682
$\mathbf{K}_{\parallel}$(**2**)	0.693	0.640	0.619
$\mathbf{K}_{\perp}$	0.774	0.728	0.458
f (cm)	142	143, 164	146,146

3.11 Thermal gravimetric analysis

The thermal behaviours of all complexes **1-9** were studied by thermal gravimetric analysis under the nitrogen atmosphere and the weight loss was measured from ambient temperature to 600 ˚C. The thermograms of mononuclear complexes **1-4** are shown in Fig. 103. The thermal decomposition process of all complexes occurs in three steps. In the thermalgravimetric graph of complex **1**, the weight loss at ~100 ˚C is associated with the mass loss of the ionic perchlorate molecule. Similarly, weight losses at ~ 150 ˚C and ~270 ˚C are associated with the loss of co-ligand that is coordinated water molecule and pro ligand (HL) molecules, respectively. Similarly, a decomposition pattern is observed in complex **2**. In complex **2**, the decomposition observed at ~80 ˚C due to perchlorate molecule and other two decomposition patterns observed at temperature 250 ˚C and 350 ˚C is due to coordinated water and ligand molecules, respectively. In complex **3**, at temperatures, 200 ˚C, 250 ˚C, and 400 ˚C are due to nitrate, water and ligand molecules, respectively. Similarly, three decomposition patterns for complex **4** are observed at temperatures 90 ˚C, 250 ˚C and 400˚C. The difference in decomposition patterns of all four complexes is due to different coordinated molecules and counter ions. The final product of all complexes is CuO which was determined experimentally. Similar TGA patterns of copper(II) complexes were earlier reported [131].

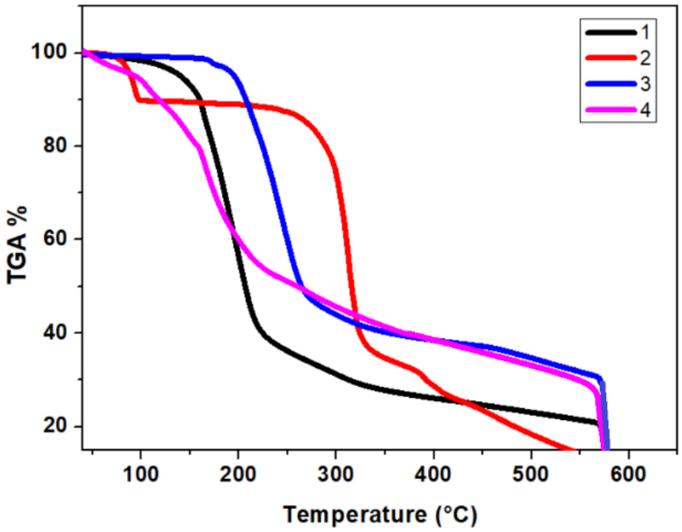

Fig. 103. TGA graph of complexes **1-4**.

The thermal behavior of both mixed ligand complexes **5** and **6** were studied by thermal gravimetric analysis under the nitrogen atmosphere and the weight loss was measured from ambient temperature to 550 ˚C. The thermograms of both complexes are shown in Fig. 104. The thermal decomposition process occurs in three steps for both complexes**.**

In the TG graph of complex **5**, the weight loss at ~100 ˚C is associated with the separation of the ionic perchlorate molecule. Similarly, weight losses at ~ 230 ˚C and 400 ˚C are associated with the loss of co-ligand (2, 9-dimethyl-1, 10-phenanthroline) and pro ligand (HL) molecules, respectively. In complex **6**, crystal lattice methanol molecule volatilized within the temperature range ~ 90 ˚C. In the second step benzimidazole separation occurs at ~ 300 ˚C and in the third step separation of pro ligand (HL) occurs at ~380˚C. The final product of both complexes CuO was determined experimentally. Similar TGA patterns of copper(II) complexes were earlier reported [131].

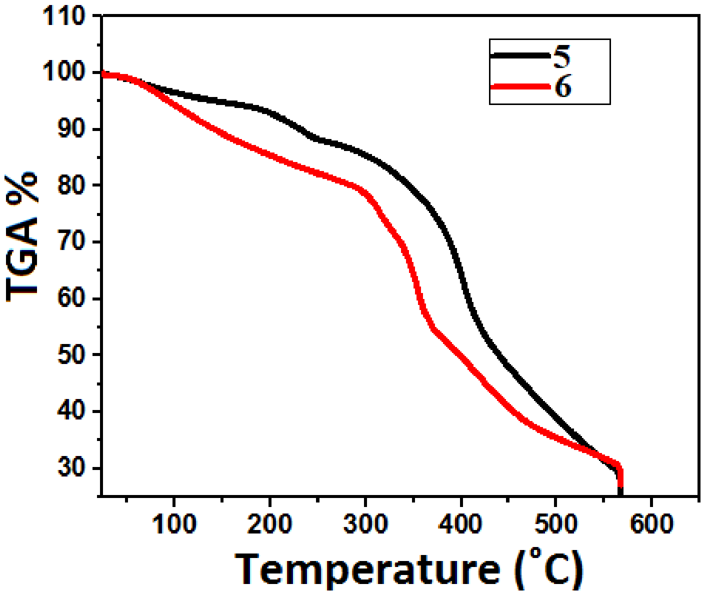

Fig. 104. TGA graph of complexes **5** and **6**.

The thermal behaviour of binuclear complexes **7-9** were measured in the temperature range of 25 ˚C to 550 ˚C (Fig. 105). The TGA pattern of these complexes is a little bit different to those all mononuclear and mixed ligand complexes. All these complexes show three-step decomposition patterns. This is due to the structural variation of the complexes as these complexes are binuclear in nature. In the TGA graph of complex **7** and **8**, the first decomposition is observed at 130 ˚C –180 ˚Crange which is due to the removal of coordinated water molecules. The number of water molecules determined from the thermograms confirms the data obtained by elemental analysis. Similarly, the first decomposition pattern for complex **9** is observed around ~150 ˚C which is due to the removal of uncoordinated perchlorate molecule. The second decomposition pattern in all complexes is observed at the temperature range of 230 ˚C-270 ˚C is due to the removal of bridged molecules such as perchlorate, sulphate and 2,2-bipyrimidine molecules. The last decomposition is observed at 350 ˚C to 400 ˚C is due to the removal of ligand moiety leaving behind the final product CuO.

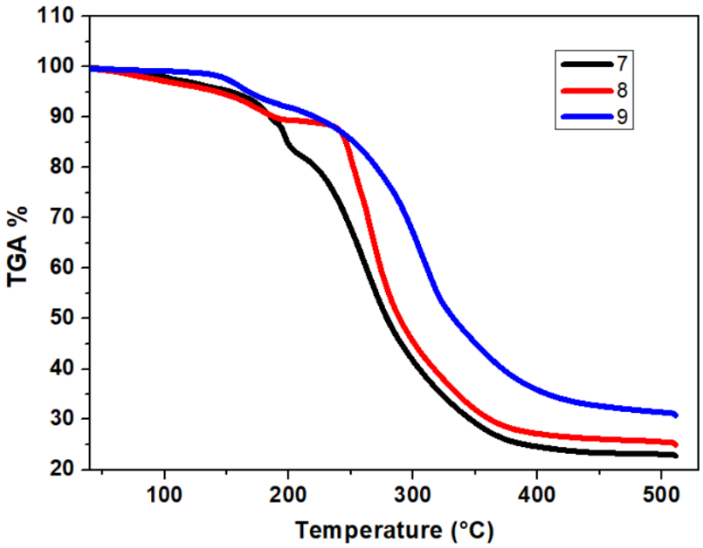

Fig. 105. TGA graph of complexes **7-9**.

3.12 Superoxide scavenging activity

The superoxide scavenging activity (SOD-mimetic activity) was examined for all complexes (**1-4**) using the nitro blue tetrazolium (NBT) method. [58, 59] SOD activity was spectrophotometrically monitored by reduction of NBT with superoxide ($O_2^{\cdot -}$) generated by alkaline DMSO. As the reduction begins the light pink color of farmazan developed and changes from pink to light blue. The colour change was spectrophotometrically monitored at 550 nm. When a chemical inhibitor (complex) is added, the reduction reaction proceeds and the rate of increase were reduced with increasing concentration. The rate of absorption changes is evaluated and the concentration required to yield 50% inhibition (IC_{50}) be procured by making a plot in between percentage inhibition (% I) versus concentration of inhibitors (Fig. 106). The IC_{50} (µM) values of all complexes collected in Table 24 remain in the range of 10.13-12.85 µM. The SOD activity of complexes **1-4** is shown to be in the order of **2** > **1** > **3** > **4**. It is observed that the SOD activity of **2** was comparable to that of **1**as detected from the IC_{50} values of 11.21 and 10.31µM, respectively. In the same Table, SOD activity and catalytic rate constant (k_{McCF}) were also given along with scavenging data of similar complexes. Data of Vc were considered as standard. The difference in IC_{50} and SOD activity could be ascribed due to structural variation in these complexes [166]. The geometry of mononuclear complexes (**1-3**) is distorted square planar. Although the square-planar copper(II) centre is usually considered unfavorable in the context of SOD scavenging activity [167]. But our square planar mononuclear complexes (**1-4**) showed considerably higher scavenging activity. In these complexes (**1-4**) fourth coordination sites are occupied by water molecule except in **4** in which the fourth position is occupied by Cl atom which is easily replaced by($O_2^{\cdot-}$) during scavenging tenure, being an electroneutral (labile molecules) solvent. Complex **4** showed slightly higher IC_{50} due to the presence of the Cl atom in the fourth equatorial position. Due to the presence of solvent (water) molecules in complexes, **1-3** showed various H-bondings. Therefore H-bonding may accelerate the SOD scavenging activity [167]. H-bonding interaction site may assist the induction of $O_2^{\cdot-}$ to Cu(II) ion. Similar behavior in four coordinate copper(II) complexes has been reported [166,168-170]. It is observed that distorted structure around the copper(II) ion is quite important for SOD scavenging activity.The results of scavenging activity in graphical form are shown in Fig. 106. The scavenging activities of complexes (**1-4**) are similar to the value reported in other similar complexes.

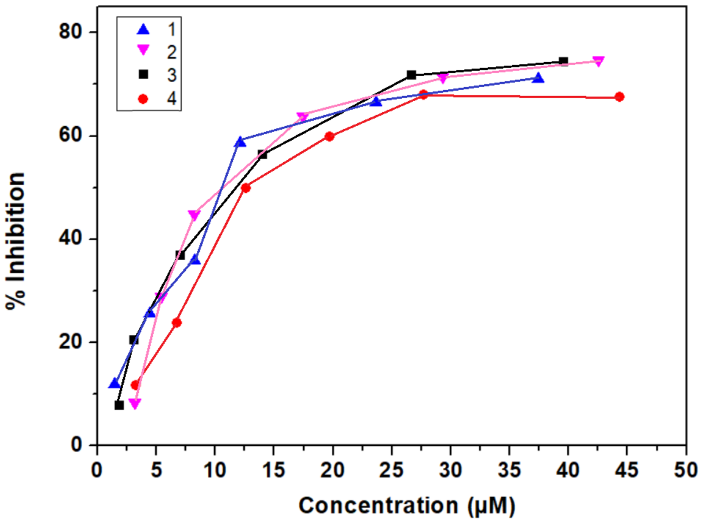

Fig. 106. SOD graph of complex **1-4**.

The catalytic rate constant (k_{McCF}) of these complexes was evaluated using the equation:

$$k_{McCF} = k_{NBT} \times [NBT]/IC_{50}$$

where $k_{NBT} = 5.94 \times 10^4$ (mol $L^{-1})^{-1}s^{-1}$; [NBT] = 56 μM. The k_{McCF} is the second-order rate constant for NBT [171-173]. The values of catalytic rate constants for all complexes are given in Table 24. On perusal of rate constant data for the superoxide disproportionation constant (k_{McCF}) reveal that these complexes could be considered as SOD mimics, with **2** being the best suited to react with $O_2^{\cdot-}$ and are more efficient SOD mimics than vitamin C, which is the standard antioxidant (SOD mimic) [174]. The proposed catalytic mechanism could be in two steps (Scheme 6). In step (i) is an attack of $O_2^{\cdot-}$ on SOD mimics and inner-sphere electron transfer takes place with the release of O_2 molecule. Step (ii) The reduced copper (Cu^+) reoxidized by the second $O_2^{\cdot-}$ a molecule with the transfer of a proton to the peroxide ion [165].

Table 24 Superoxide scavenging activity parameters and catalytic rate constant for **1-4**.

Compound	IC_{50}(μM)	SOD activity (μM^{-1})	k_{McCF} $(ML)^{-1}s^{-1} \times 10^4$	Reference
VC	852	1.17	0.39	174
$[Cu(Phimp)(H_2O)]_2(ClO_4)_2$	11.20	89.28	29.70	166
$[Cu(Phimp)(CH_3COO)]$	8.31	120.34	40.03	166
$[Cu(tnpa)OH]ClO_4$	11.03	90.66	30.16	167
$[Cu(tapa)OH]ClO_4$	7.46	134.05	44.59	167
$[Cu(tpa)(H_2O)](ClO_4)_2$	12.50	80.00	26.61	167
$[(L)Cu(\mu\text{-}CH_3COO)_2Cu(L)]$	35.00	28.57	9.50	132
$[(L)Cu(\mu\text{-}NO_3)_2Cu(L)]$	26.00	38.46	12.79	132
1	11.21	89.21	29.67	This work
2	10.13	98.71	32.84	This work
3	12.50	80.00	26.61	This work
4	12.85	78.23	25.76	This work

(where, (E)-2-((2-phenyl-2-(pyridin-2-yl)hydrazono)methyl)phenol (Phimp), tris(6- peopentylamino-2-pyridylmethy)amine (tnpa), tris(6- amino-2-pyridylmethy)amine (tapa), tris(2-pyridylmethyl)amine (tpa) and N'- [phenyl(pyridin-2-yl)methylidene]benzohydrazone) (L)).

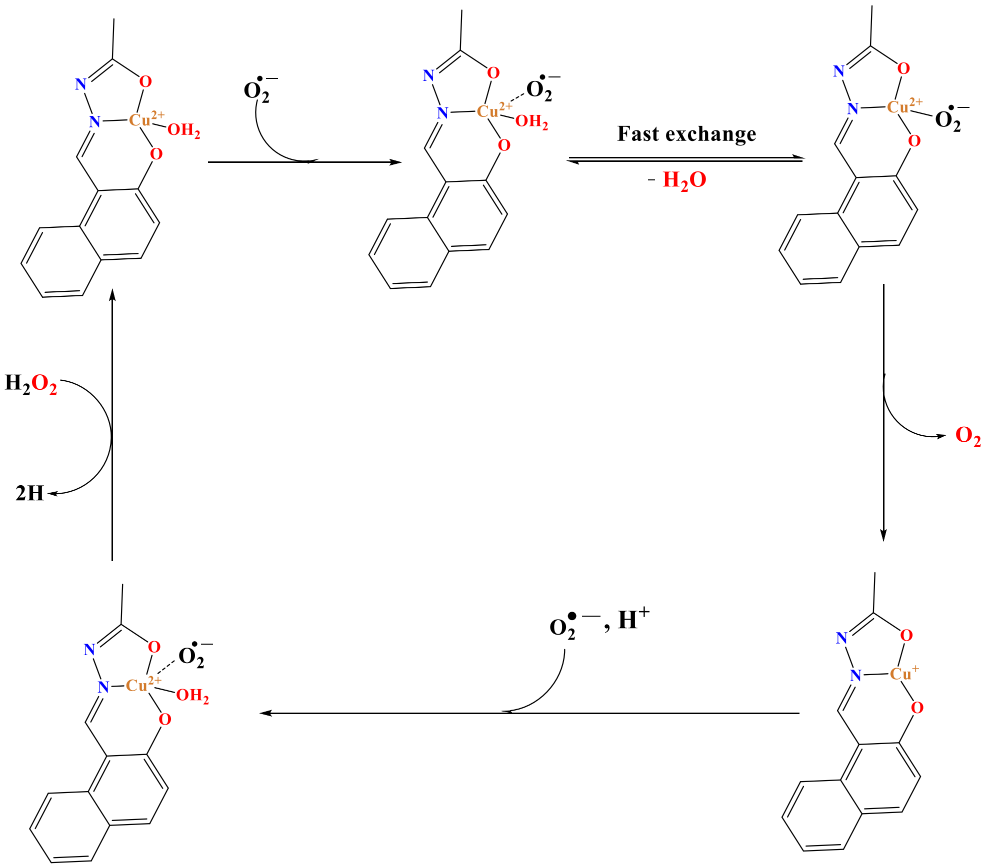

Scheme 6 The proposed mechanism of $O_2^{\cdot -}$ dismutation reaction catalyzed by SOD mimic (complex **1**).

The superoxide scavenging activity (SOD-mimetic activity) of mixed ligand complexes was also tested (**5** and **6**) using the nitro blue tetrazolium (NBT) method [58, 59] (Fig. 107). The IC_{50} (μM) values of both complexes are collected in Table 25. In the same table SOD activity and catalytic rate constant (k_{McCF}) were also given along with scavenging data of similar complexes. Data of vitamin C (Vc) were considered standard [174, 175]. Both complexes showed good scavenging activity (Table 25). The difference in IC_{50} and SOD activity of present complexes could be ascribed due to structural variation in both complexes [166]. The geometry of mononuclear complexes **5** is distorted square pyramidal whereas the geometry of complex **6** is distorted square planar as confirmed from single-crystal X-ray analysis. Although the square-planar copper(II) center is usually considered unfavorable in the context of SOD scavenging activity [167]. But square planar mononuclear complexes (**6**) showed considerably higher scavenging activity. Both complexes showed various H-bondings. Therefore H-bonding may accelerate the SOD scavenging activity [125]. H-bonding interaction site may assist the induction of $O_2^{\cdot -}$ to Cu(II) ion. Similar behavior in four or five-coordinate copper(II) complexes has been reported [166, 168-170]. It is observed that distorted structure around the copper(II) ion is quite important for SOD scavenging activity. The synthetic, SOD mimetic low molecular weight complexes with low molecular weight can compensate for the limitation of the pure enzyme because of such features as the lack of antigenicity, higher stability in solution (longer half-life) and low production cost [176, 177].

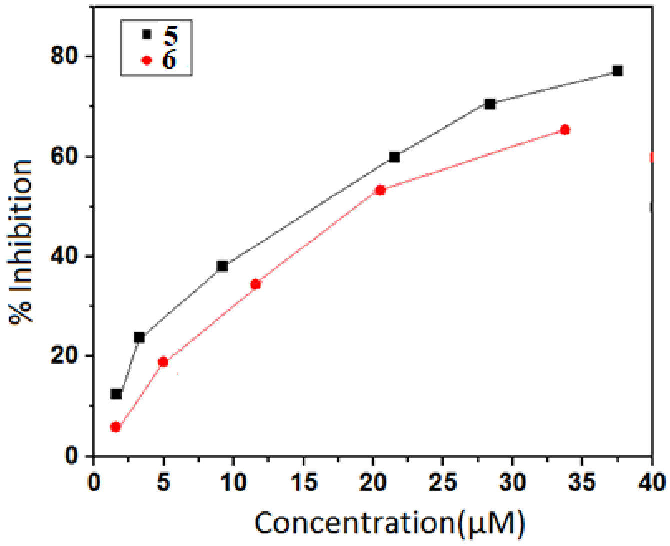

Fig. 107. SOD graph of complexes **5** and **6**.

Table 25 Superoxide scavenging activity parameters and catalytic rate constant for **5** and **6**.

Compound	IC$_{50}$(μM)	SOD activity (μM^{-1})	k_{McCF} (ML)$^{-1}$s^{-1} × 10^4	Reference
VC	852	1.17	0.39	174, 175
[Cu(Phimp)(H$_2$O)]$_2$(ClO$_4$)$_2$	11.20	89.28	29.70	166
[Cu(Phimp)(CH$_3$COO)]	8.31	120.34	40.03	166
[Cu(tnpa)OH]ClO$_4$	11.03	90.66	30.16	167
[Cu(tapa)OH]ClO$_4$	7.46	134.05	44.59	167
[Cu(tpa)(H$_2$O)](ClO$_4$)$_2$	12.50	80.00	26.61	167
5	18.27	54.73	18.21	This work
6	16.72	59.81	19.89	This work

Phimp= (2-((2-phenyl-2-(pyridin-2-yl)hydazono)methyl)phenol),tnpa = tris(6-peopentylamino-2-pyridylmethy)amine, tapa = tris(6- amino-2-pyridylmethy)amine and tpa = tris(2-pyridylmethyl)amine.

The catalytic rate constant (k_{McCF}) of these complexes was also evaluated. The values of catalytic rate constants for both complexes are given in Table 25. On perusal of rate constant data for the superoxide disproportionation constant (k_{McCF}) clearly reveal that these complexes could be considered as SOD mimics, with **6** being the best suited to react with $O_2^{\cdot-}$ and are more efficient SOD mimics than vitamin C, which is the standard antioxidant (SOD mimic) [174].

The proposed catalytic mechanism could be in two steps (Scheme 7). In step (i) is the attack of $O_2^{\cdot-}$ on SOD mimics and inner-sphere electron transfer takes place with the release of the O_2 molecule. Step (ii) The reduced copper (Cu^+) reoxidized by the second $O_2^{\cdot-}$a molecule with a transfer of a proton to the peroxide ion [173].

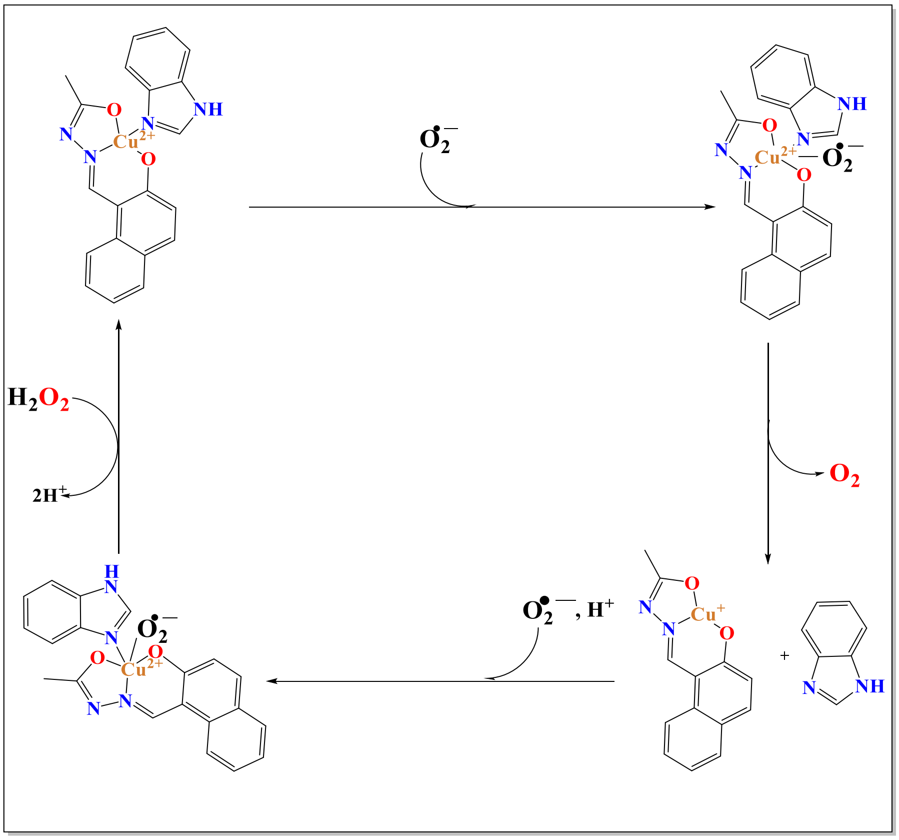

Scheme 7 The proposed mechanism of $O_2^{\cdot-}$ dismutation reaction catalyzed by SOD mimic (complex **5**).

The superoxide scavenging activity (SOD-mimetic activity) of binuclear complexes **7**, **8** and **9** were also evaluated and the concentration required to yield 50% inhibition (IC_{50}) be procured by making a plot in between percentage inhibition (% I) versus concentration of inhibitors [57, 178] (Fig. 108). The IC_{50} (μM) values of all complexes are collected in Table 26. In the same table SOD activity and catalytic rate constant (k_{McCF}) were also given along with scavenging data of similar complexes. Data of Vc were considered as standard. Complexes **7**, **8** and **9** showed high IC_{50} compared to other mononuclear complexes **1-4** and mixed ligand complexes **5** and **6**. These complexes (**7**, **8** & **9**) showed was scavenging activity (Table 26). Homo binuclear complexes **7** and **8** showed the highest SOD activity (for **7**). Although in these complexes both copper(II) centres posses square pyramidal geometry. In these binuclear complexes, one of the coordination sites is occupied by an electroneutral water molecule, which is easily replaced by $O_2^{\cdot -}$ [142]. The presence of solvent (water) molecules in complexes **7** and **8** showed various H-bondings. Therefore H-bonding may accelerate the SOD scavenging activity [167]. H-bonding interaction site may assist the induction of $O_2^{\cdot -}$ to Cu(II) ion. Similar behaviour in four coordinate copper(II) complexes has been reported [168-171]. It is observed that distorted structure around the copper(II) ion is quite important for SOD scavenging activity.

The results of scavenging activity in graphical form are shown in Fig. 108. The scavenging activities of complexes (**7-9**) are to the value reported by other similar complexes. Scavenging activity values indicate that complexes **7** and **8** are potent superoxide dismutase mimics. The SOD scavenging activities of mononuclear complexes are less than those of homobinuclear complexes. Such behaviour is in agreement with the results of previously reported IC_{50} values of homo or hetero binuclear complexes [179-182]. Although the copper-copper interaction is not observed in solution epr studies. Therefore, the flexibility of tridentate Schiff base, presence of labile water molecule as in one coordination site and binuclear centres could accelerate the catalytic cycle and tridentate ligand can function both of the dioxygen binding and electron transfer sites in the catalytic cycle (Fig. 64).

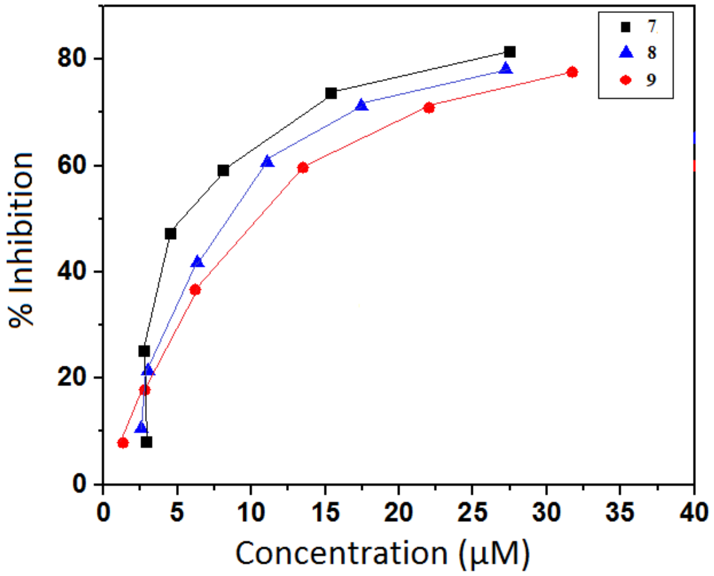

Fig. 108. SOD graph of complex **7-9**.

Table 26 Superoxide scavenging activity parameters and catalytic rate constant for **7-9**.

Compounds	**IC_{50} (μM)**	**SOD activity (μM^{-1})**	**k_{McCF} $(ML)^{-1}s^{-1} \times 10^4$**	**Reference**
VC	852	1.17	0.39	174, 175
$[Cu(Phimp)(H_2O)]_2(ClO_4)_2$	11.20	89.28	29.70	166
$[Cu(Phimp)(CH_3COO)]$	8.31	120.34	40.03	166
$[Cu(tnpa)OH]ClO_4$	11.03	90.66	30.16	167
$[Cu(tapa)OH]ClO_4$	7.46	134.05	44.59	167
$[Cu(tpa)(H_2O)](ClO_4)_2$	12.50	80.00	26.61	167
$[(L)Cu(\mu\text{-}CH_3COO)_2Cu(L)]$	35.00	28.57	9.50	132
$[(L)Cu(\mu\text{-}NO_3)_2Cu(L)]$	26.00	38.46	12.79	132
7	6.23	160.51	53.39	This work
8	7.35	136.05	45.26	This work
9	11.45	87.34	29.05	This work

(where, (E)-2-((2-phenyl-2-(pyridin-2-yl)hydrazono)methyl)phenol (Phimp), tris(6- peopentylamino-2-pyridylmethy)amine (tnpa), tris(6- amino-2-pyridylmethy)amine (tapa), tris(2-pyridylmethyl)amine (tpa) and N'- [phenyl(pyridin-2-yl)methylidene]benzohydrazone) (L)).

The values of catalytic rate constants for **7-9** complexes are given in Table 26. On perusal of rate constant data for the superoxide disproportionation constant (k_{McCF}) reveal that these complexes could be considered as SOD mimics, with **7** being the best suited to react with $O_2^{\cdot -}$ and are more efficient SOD mimics than vitamin C, which is the standard antioxidant (SOD mimic) [183]. The proposed catalytic mechanism could be in two steps (Scheme 8). In step (i) is an attack of $O_2^{\cdot -}$ on SOD mimics and inner-sphere electron transfer takes place with the release of O_2 molecule. Step (ii) The reduced copper (Cu^+) reoxidized by the second $O_2^{\cdot -}$ the molecule with the transfer of a proton to the peroxide ion [184].

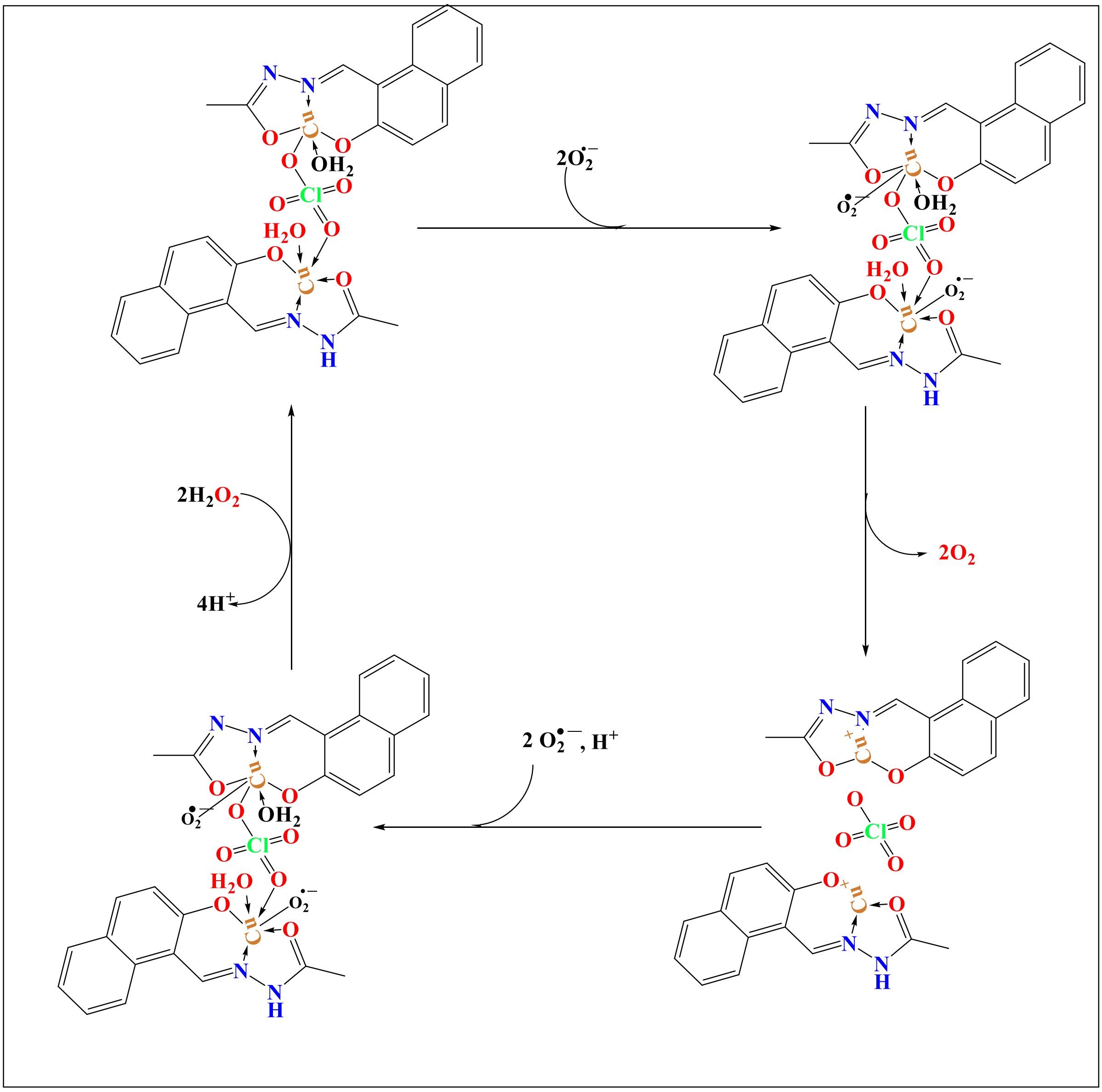

Scheme 8 The proposed mechanism of $O_2^{\cdot -}$ dismutation reaction catalyzed by SOD mimic (complex **7**).

4 Conclusions

In summary, we have synthesized and characterized nine copper(II) complexes with tridentate hydrazone (HL) ligand. Molecular structures of all complexes have been determined using single-crystal X-ray diffraction techniques. The Hirshfeld analysis and the fingerprint plots revealed how much the weak CH···π and π ···π non-covalent interactions lead both complexes to build supramolecular architectures. The paramagnetic behaviour of all complexes has been explored using magnetic and X-band epr spectral study. The electrochemical stability of the metal center was investigated using cyclic and differential pulse voltammetry. Time-Dependent Density functional theory (TD-DFT) calculations throw light on electronic transitions. Finally, SOD activity data of all complexes collected at pH 7.4 using the NBT assay method. SOD activity measurements manifest that these complexes are good models with outstanding catalytic activity towards the dismutation of $O_2^{\cdot -}$.

References

1 J. Pisk, B. Prugovecki, D.M. Calogovic, T. Jednacak, P. Novak, D. Agustin, V. Vrdoljak, RSC Adv. 4 (2014) 39000-39010.
2 O. Pouralimardan, A.C. Chamayou, C. Janiak, H.H. Monfared, Inorg. Chim. Acta 360 (2007) 1599-1608.
3 M. Bakir, O. Green, W.H. Mulder, J. Mol. Struct. 873 (2008) 17-28.
4 C. Basu, S. Chowdhury, R. Banerjee, H.S. Evans, S. Mukherjee, Polyhedron 26 (2007) 3617-3624.
5 M. Alagesan, N.S.P. Bhuvanesh, N. Dharamraj, Dalton Trans. 42 (2013) 7210-7223.
6 S.K. Sridhar, M. Saravanan, A. Ramesh, Eur. J. Med. Chem. 36 (2001) 615-625.
7 B. Bottoari, R. Maccari, F. Monforte, R. Ottana, E. Rotondo, M.G. Vigorita, Biorg. Med. Chem. Lett. 10 (2000) 657-660.
8 E.W. Ainscough, A.M. Brodie, A.J. Dobbs, J.D. Ranford, J.M. Waters, Inorg. Chim. Acta. 267 (1998) 27-38.
9 J. Easmon, G. Puerstinger, T. Roth, H.H. Fiebig, M. Jenny, W. Jaeger, G. Heinisch, J. Hofmann, Int. J. Cancer 94 (1999) 89-96.
10 S.G. Kucukguzel, S. Rollas, I. Kucukguzel, M. Kiraz, Eur. J. Med. Chem. 34 (1999) 1093-1100.
11 V. Vrdoljak, B. Prugovecki, D.M. Calogovic, R. Dreos, P. Siega, C. Tavagnacco, Cryst. Growth Des. 10 (2010) 1373-1382.
12 V. Vrdoljak, B. Prugovecki, D.M. Calogovic, J. Pisk, R. Dreos, P. Siega, Cryst. Growth Des. 11 (2011) 1244-1252.
13 V. Vrdoljak, B. Prugovecki, D.M. Calogovic, T. Hrenor, R. Dreos, P. Siega, Cryst. Growth Des.13 (2013) 3773-3784.
14 S. H. Li, S. K Gao, S. X. Liu, Y. N. Guo, Cryst. Growth Des. 10 (2010) 495-503.
15 Shakdofa, M.E. Mohamad, M.H. Shtaiwi, N. Morsy, A. Rassel, M.A. Tayseer, Main Group Chemistry 13 (2014) 187-218.
16 L.M. Wu, H.B. Teng, X.B. Ke, W.J. Xu, J.T. Su, S.C. Liang, X.M. Hu, Chem. Biodiversity 4 (2007) 2198-2209.
17 S. Gupta, S. Pal, A.K. Barik, A. Hazra, S. Roy, T. N. Mandal, S.M. Peng, G. H. Lee, M. Salah, El. Fallah, J. Tercero, S.K. Kar, Polyhedron 27 (2008) 2519-2528.
18 N.M.H. Salem, L.E. Sayed, M. F. Iskander, Polyhedron 27 (2008) 3215-3226.

19 G.C. Xu, L. Zhang, L. Liu, G. F. Liu, D. Z. Jia, Polyhedron 27 (2008) 12-24.

20 P. Talukder, A. Datta, S. Mitra, G. Rosair, M.S.EI. Fallah, J. Ribas, Dalton Trans. (2004) 4161-4167.

21 S.K. Patel, R.N. Patel, Y. Singh, Y.P. Singh, D. Kumhar, R.N. Jadeja, H. Roy, A.K. Patel, N. Patel, A. Banerjee, D. Choquesillo-Lazarte, A. Gutierrez, Polyhedron 161 (2019) 198-212.

22 Y. Singh, R.N. Patel, R.N. Jadeja, A.K. Patel, N. Patel, H. Roy, P. Bhagriya, R. Singh, R.J. Butcher, J.P. Jasinski, S. Herrero, M. Cortijo, Inorg. Chim. Acta 503 (2020) 119371.

23 R.N. Patel, Y. Singh, Y.P. Singh, A.K. Patel, N. Patel, R. Singh, R.J. Butcher, J.P. Jasinski, E.Colacia, M. A. Palacios, New. J. Chem. 42 (2018) 3112-3136.

24 Y. Singh, R.N. Patel, R.N. Jadeja, A.K. Patel, N. Patel, H. Roy, P. Bhagriya, R. Singh, R.J. Butcher, J.P. Jasinski, S. Herrero, M. Cortijo, Inorg. Chim. Acta 503 (2020) 119371.

25 J.M. Lehn, Angew. Chem. Int. Engl. 29 (1990) 1304-1319.

26 M. Emami, N. Noshiranzadeh, R. Bikas, A. Gutierrez, A. Kozakiewicz, Polyhedron 122 (2017) 137-146.

27 G.R. Desiraju, Angew. Chem. Int. Ed. Engl. 34 (1995) 2311-2327.

28 F.H. Allen, W.D.S. Motherwell, P.R. Raithby, G.P. Shields, R. Taylor, New J. Chem. 23 (1999) 25-34.

29 L. Addadi, M. Geva, Cryst. Eng. Commn. 5 (2003) 140-146.

30 C.W. Bielawski, R.H. Grubbs, Angew. Chem. Int. Ed. 39 (2000) 2903-2906.

31 S.G. Fleischman, S.S. Kuduva, J.A. Machahon, B. Moulton, R.D.B. Walsh, N.R.G. Hornedo, M.J. Zaworotko, Cryst. Growth Des. 3 (2003) 909-919.

32 R.D.B. Walsh, M.W. Bradner, S. Fleischman, L.A. Morales, B. Moulton, N.R.G. Hornedo, M. J. Zaworotko, Chem. Commun. 2 (2003) 186-187.

33 O. Almarsson, M. J. Zaworotko, Chem. Commun. 17 (2004) 1889-1896.

34 R. Bruce King, Encl. Inorg. Chem. John Wiley and Sons, Ltd. 10 (2006).

35 G.M. Sheldrick, SADABS (Version 2.03), University of Gottingen, Germany, 2002.

36 SMART (V 5.628), SAINT (V6.45a), XPREP, SHELXTL, Bruker AXS Inc., Madison, WI, 2004.

37 G.M. Sheldrick, Acta Crystallogr. Sec. A 64 (2008) 112-122.

38 A.L. Spek, Acta Cryst. 65 (2009)148-155.

39 L.J. Farrugia, J. Appl. Cryst. 30 (1997) 565-566.

40 L.J. Farrugia, J. Appl. Cryst. 32 (1999) 837-838.

41 M.A. Spackman, J.J. McKinnon, Cryst. Eng. Comm. 4 (2002) 378-392.

42 M.A. Spackman, P.G. Byrom, Chem. Phy. Lett. 267 (1997) 215-220.

43 J.J. McKinnon, A.S. Mitchell, M.A. Spackman, J. Eur. Chem. 4 (1998) 2136-2141.

44 J.J. McKinnon, M.A. Spackman, A.S. Mitchell, Acta Crystallogr. Sec. B 60 (2004) 627-668.

45 A.L. Rohl, M. Moret, W. Kaminsky, K. Claborn, J.J. McKinnon, B. Kahr, Cryst. Growth Des. 8 (2008) 4517-4525.

46 A. Parkin, G. Barr, W. Dong, C.J. Gilmore, D. Jayatilaka, J.J. McKinnon, M.A. Spackman, C.C. Wilson, Cryst. Eng. Comm. 9 (2007) 648-652.

47 S.K. Wolff, D.J. Greenwood, J.J. McKinnon, D. Jayatilaka, M.A. Spackman, Crystal Explorer 2.0; University of Western Australia: Perth, Australia, 2007.

48 J.J. Koenderink, A.J. van Doorn, Image Vision Comput. 10 (1992) 557-564.

49 G.A. Petersson, M.A. Al-Laham, J. Chem. Phys. 94 (1991) 6081–6090.

50 P.J. Hay, W.R. Wadt, J. Chem. Phys. 82 (1985) 270–283.

51 M.J. Frisch, G.W. Trucks, H.B. Schlegel, G.E. Scuseria, M.A. Robb, J.R. Cheeseman, G. Scalmani, V. Barone, B. Mennucci, G.A. Petersson, H. Nakatsuji, M. Caricato, X. Li, H.P. Hratchian, A.F. Izmaylov, J. Bloino, G. Zheng, J. L. Sonnenberg, M. Hada, M. Ehara, K. Toyota, R. Fukuda, J. Hasegawa, M. Ishida, T. Nakajima, Y. Honda, O. Kitao, H. Nakai, T. Vreven, J.A. Montgomery Jr., J.E. Peralta, F. Ogliaro, M. Bearpark, J.J. Heyd, E. Brothers, K.N. Kudin, V.N. Staroverov, R. Kobayashi, J. Normand, K. Raghavachari, A. Rendell, J.C. Burant, S.S. Iyengar, J. Tomasi, M. Cossi, N. Rega, J.M. Millam, M. Klene, J.E. Knox, J.B. Cross, V. Bakken, C. Adamo, J. Jaramillo, R. Gomperts, R.E. Stratmann, O. Yazyev, A.J. Austin, R. Cammi, C. Pomelli, J.W. Ochterski, R.L. Martin, K. Morokuma, V.G. Zakrzewski, G.A. Voth, P. Salvador, J.J. Dannenberg, S. Dapprich, A.D. Daniels, O. Farkas, J.B. Foresman, J.V. Ortiz, J. Cioslowski, D.J. Fox, Gaussian 09, Revision D.01, Gaussian Inc., Wallingford CT, (2009).

52 R. Bauernschmitt, R. Ahlrichs, Chem. Phys. Lett. 256 (1996) 454–464.

53 M. Cossi, N. Rega, G. Scalmani, V. Barone, J. Comput. Chem. 224 (2003) 669–681.

54 T. Mossman, J. Immunol. 65 (1993) 55-63.

55 A.K. Patel, R.N. Jadeja, R.J. Butcher, M.K. Kesharwani, J. Kastner, M. Muddassir, Polyhedron 195 (2021) 114969.

56 R. Konecny, J. Li, C.L. Fisher, V. Dillet, D. Bashford, L. Noodleman, Inorg. Chem. 38 (1999) 940-950.

57 R.G. Bhirud, T.S. Srivastava, Inorg. Chim. Acta 173 (1990) 121-125.

58 Z.R. Liao, X.F. Zheng, B.S. Luo, L.R. Shen, D.F. Li, H.L. Liu, W. Zhao, Polyhedron 20 (2001) 2813-2821.

59 R.N. Patel, Y.P. Singh, Y. Singh, R.J. Butcher, J.P. Jasinski, Polyhedron 133 (2017) 102-109.

60 B. Shaabani, A.A. Khandar, H. Mobaiyen, N. Ramazani, S.S. Balula, L.C-. Silva, Polyhedron 80 (2014) 166-172.

61 S. Naiya, C. Biswas, M.G.B. Drew, C.J.G-. Garcia, J.M.C-. Juan, A. Ghosh, Inorg. Chem. 49 (2010) 6616–6627.

62 S. Banerjee, A. Ray, S. Sen, S. Mitra, D.L. Hughes, R.J. Butcher, S.R. Batten, D.R. Turner, Inorg. Chim. Acta 361 (2008) 2692-2700.

63 S. Banerjee, S. Sen, S. Basak, S. Mitra, D.L. Hughes, C. Desplanches, Inorg. Chim. Acta 361 (2008) 2707-2714.

64 A. Ray, S. Banerjee, R.J. Butcher, C. Desplanches, S. Mitra, Polyhedron 27 (2008) 2409-2415.

65 S. Banerjee, S. Mondal, W. Chakraborty, S. Sen, R. Gachhui, R.J. Butcher, A.M.Z. Slawin, C. Mandal, S. Mitra, Polyhedron 28 (2009) 2785-2793.

66 R. Bikas, H.H. Monfared, T. Lis, M. Siczek, Inorg. Chem. Commun. 15 (2012) 151-155.

67 S. Dasgupta, P. Chakraborty, P. Kundu, H. Kara, G. Aullón, E. Zangrando, D. Das, Cryst. Eng. Comm. 21 (2019) 7094–7107.

68 B.J. Hathaway, A.E. Underhill, J. Chem. Soc. (1961) 3091-3096.

69 R.N. Patel, Y.P. Singh, Y. Singh, R.J. Butcher, M. Zeller, R.K.B. Singh, O.U-wang, J. Mol. Struct. 1136 (2017) 157-172.

70 R.N. Patel, S.K. Patel, D. Kumhar, N. Patel, A.K. Patel, R.N. Jadeja, N. Patel, R.J. Butcher, M. Cortijo, S. Herrero, Polyhedron 188 (2020) 114687.

71 R.N. Patel, Y.P. Singh, Y. Singh, R.J. Butcher, Polyhedron 104 (2016) 116-126.

72 K. Nakamoto, Infrared Spectra of Inorganic and Coordination Compounds, second ed., Wiley-Interscience, New York, N.Y., 1970.

73 P. Braunstein, F. Naud, Angew. Chem. Int. Ed. 40 (2001) 680-699.

74 R. Mukherjee, Coord. Chem. Rev. 203 (2000) 151-218.

75 R. Dorta, E.D. Stevens, N.M. Scott, C. Costabile, L. Cavallo, C.D. Hoff, S.P. Nolan, J. Am. Chem. Soc. 127 (2005) 2485-2495.

76 K. Nakamoto: Infrared and Raman Spectra of Inorganic and Coordination Compounds, 4. Auflage, John Wiley & Sons, New York, Chichester, Brisbane, Toronto, Singapore 1986.

77 R.N. Patel, Y. Singh, Y.P. Singh, R.J. Butcher, A. Kamal, I.P. Tripathi, Polyhedron 117 (2016) 20-34.

78 R.N. Patel, S.K. Patel, D. Kumhar, N. Patel, A.K. Patel, R.N. Jadeja, N. Patel, R.J. Butcher, M. Cortijo, S. Herrero, Polyhedron 188 (2020) 114687.

79 J.L. Pascal, J. Potier, D.J. Jones, J. Roziere, A. Michalowicz, Inorg. Chem. 23 (1984) 2068-2073.

80 C. Basu, S. Biswas, A.P. Chattopadhyay, H.S.-Evans, S. Mukherjee, Eur. J. Inorg. Chem. (2008) 4927–4935

81 M. Julve, G.D. Munno, G. Bruno, M. Verdaguer, Inorg. Chem. 27 (1988) 3160-3165

82 A.Z. El-Sonbati, Transit. Met. Chem. 16 (1991) 45–47.

83 S. Naiya, C. Biswas, M.G.B. Drew, C.J. Gomez-Garcia, J.M. Clemente-Juan, A. Ghosh, Inorg. Chem. 49 (2010) 6616-6629.

84 L. Yang, D.R. Powell, R.B. Houser, Dalton Trans. 6 (2007) 955-964.

85 A. Okuniewski, D. Rosiak, J. Chojnacki, B. Becker, Polyhedron 90 (2015) 47-57.

86 I. Shimizu, Y. Morimoto, D. Faltermeier, M. Kerscher, S. Paria, T. Abe, H. Sugimoto, N. Fujieda, K. Asano, T. Suzuki, P. Comba, S. Itoh, Inorg. Chem. 56 (2017) 9634−9645.

87 S. Scheiner, T. Kar, J. Pattanayak, J. Am. Chem. Soc. 124 (2007) 13257-13264.

88 M. Egli, S. Sarkhel, Acc. Chem. Res. 40 (2007) 197-205.

89 A. Nangia, G.R. Desiraju, Top. Curr. Chem. 198 (1998) 57-95.

90 V.R. Pedireddi, N. Seetha Lekshmi, Tetrahedron Lett. 45 (2004) 1903-1906.

91 J. Patole, U. Sandbhor, S. Padhye, D.N. Deobagkar, C.E. Anson, A. Powell, Bioorg. Med. Chem. Lett. 13 (2003) 51-55.

92 M.B. Ferrari, G.G. Fava, E. Leporati, G. Pelosi, R. Rossi, P. Tarasconi, R. Albertini, A. Bonati, P. Lunghi, S. Pinelli, J. Inorg. Biochem. 70 (1998) 145-154.

93 M. Alagesan, N.S.P. Bhuvanesh, N. Dharmaraj, Dalton Trans. 42 (2013) 7210-7223.

94 A. Dutta, M. Trivedi, A. Alarifi, A. Kumar, M. Muddassir, J. Mol. Struct. 1207 (2020) 127801.

95 H. Endres, D. Noethe, E. Rossato, W.E. Hatfield, Inorg. Chem. 23 (1984) 3467-3473.

96 D. Sredojevie, Z.D. Tomic, S.D. Zaric, Cryst. Growth Des. 10 (2010) 3901-3908.

97 T. Korenaga, H. Tanaka, T. Ema, T. Sakai, J. Fluorine Chem. 122 (2003) 201-205.

98 A. Castiniras, A.G. Sicilia-Zafra, J.M.Gonzalez- Pérez, D. Choquesillo-Lazarte, J. Niclós-Gutiérrez, Inorg. Chem. 41 (2012) 6956-6958.

99 H. Kitamura, T. Oshima, Org. Lett. 10 (2010) 293-296

100 G. Mahmoudi, A. Bauza, A. Frontera, Dalton Trans. 45 (2016) 4965-4969.

101 S. Zahn, R. Frank, E.H-. Hawkins, B. Kirchner, Chem. Eur. J. 17 (2011) 6034-6038.

102 A. Bauza, A. Frontera, Phys. Chem. Chem. Phys. 17 (2015) 24748-24753.

103 J. Wang, Y. Pan, L. Lu, Y.F. Xiong, L. Fang, W. Luo, X. Wu, A. Kumar, J. Mol. Struct. 1196 (2019) 194-200.

104 A. Ilie, C.I. Rat, S. Scheutzow, C. Kiske, K. Lux, T.M. Klapotke, C. Silvestru, K. Karaghiosoff, Inorg. Chem. 50 (2011) 2675-2684.

105 G. Mahmoudi, A. Bauza, M. Amini, E. Molins, J. T. Magued, A. Frontera, Dalton Trans. 45 (2016) 10708-10716.

106 F.P.A. Fabbiani, L.T. Byrne, J.J. McKinnon, M.A. Spackman, Cryst. Eng. Comm. 9 (2007) 728-731.

107 J.J. Mc Kinnon, D. Jayatilaka, M.A. Spackman, Chem. Commun. (2007) 3814-3816.

108 K. Ghosh, K. Harms, S. Chattopadhyay, Polyhedron 123 (2017) 162-175.

109 J. He, J. Wang, Q. Xu, X. Wu, A. Dutta, A. Kumar, M. Muddassir, A. Alowaisd, N.A.Y. Abduh, New J. Chem. 43 (2019) 13499-13508.

110 A.D. Backe, J. Chem. Phys. 98 (1992) 5648-5692.

111 L. Zhou, Q. Hu, L.Q. Chai, K.-H. Mao, H.S. Zhang, Polyhedron 158 (2019) 102-116.

112 L. Q. Chai, L. J. Tang, L.C. Chen, J.J. Haung, Polyhedron 122 (2017) 228 -240.

113 L.Q. Chai, Y.X. Li, L.C. Chem, J.Y. Zhang, J.J. Hauang, Inorg. Chim. Acta. 444 (2016) 193-204.

114 L.Q. Chai, Q. Hu, K.Y. Zhang, L. Jhou, J.J. Haung, J. Lumin. 203 (2018) 234-246.

115 A.W. Addison, T.N. Rao, J. Reedijk, J. van Rijn, G.C. Verschoor, J. Chem. Soc. Dalton Trans. 7 (1984) 1349-1356.

116 R. Jawaria, M. Hussain, M. Khalid, M.U. Khan, M.N. Tahir, M.M. Nasser, A.A.C. Braga, Z. Shafiq, Inorg. Chim. Acta. 486 (2019) 162-171.

117 A. Kokalj, Chem. Phys. 393 (2012) 1-12.

118 R.G. Parr, L. Szentpaly, S. Liu, J. Am. Chem. Soc. 121 (1999) 1922-1924.

119 R.G. Parr, R.A. Donnelly, M. Levy, W.E. Palke, J. Chem. Phys. 68 (1978) 3801-3807.

120 P.K. Chattaraj, U. Sarkar, D.R. Roy, Chem. Rev. 106 (2006) 2065-2091.

121 C. Adamo, V. Barone, J. Chem. Phys. 110 (1999) 6158-6170.

122 F. Weigend, R. Ahlrichs, Phys. Chem. Chem. Phys. 7 (2005) 3297-3305.

123 S. Grimme, J. Antony, S. Ehrlich, H. Krieg, J. Chem. Phys. 132 (2010) 154104.

124 S. Grimme, S. Ehrlich, L. Goerigk, J. Comput. Chem. 32 (2011) 1456–1465.

125 D. Andrae, U. Häußermann, M. Dolg, H. Stoll, H. Preuß, Theor. Chim. Acta 77 (1990) 123–141.

126 R. Bauernschmitt, R. Ahlrichs, Chem. Phys. Lett. 256 (1996) 454–464.

127 Y. Zhao, D.G. Truhlar, Theor. Chem. Acc. 120 (2008) 215–241.

128 G. Sciortino, J.-D. Marechal, I. Fabian, N. Lihi, E. Garribba, J. Inorg. Biochem. 204 (2020) 110953.

129 M. Cossi, N. Rega, G. Scalmani, V. Barone, J. Comput. Chem. 24 (2003) 669–681.

130 J. Li, H. Liu, Z. Guo, M. Yang, J. Song, H. Ma, RSC Adv. 8 (2018) 2933–2940.

131 A.K. Patel, R.N. Jadeja, H. Roy, R.N. Patel, S.K. Patel, R.J. Butcher, M. Cortijo, S. Herrero, Polyhedron 186 (2020) 114624.

132 R.N. Patel, D.K. Patel, V.P. Sondhiya, K.K. Shukla, Y. Singh, A. Kumar, Inorg. Chim. Acta 405 (2013) 209-217.

133 M. Nonoyamo, K. Yamasaki, Inorg. Chim. Acta 5 (1971) 124-128.

134 J. Peisach, W.E. Blumberg, Arch. Biochem. Biophys. 165 (1974) 691-708.

135 S. Naiya, C. Biswas, M.G.B. Drew, C.J. Gomez-Garcıa, J.M. Clemente-Juan, A. Ghosh, Inorg. Chem. 49 (2010) 6616-6627.

136 L.K. Thompson, S.K. Mandal, S.S. Tandon, J.N. Bridson, M.K. Park, Inorg. Chem.35 (1996) 3117-3125.

137 R. Cao, Q. Shi, D. Sun, M. Hong, W. Bi, Y. Zhao, Inorg. Chem.41 (2002) 6161−6168.

138 T.M. Donlevy, L.R. Gahan, T.W. Hambley, G.R. Hanson, K.L. Mc Mahon, R. Stranger, Inorg. Chem. 33 (1994) 5131 -5137.

139 M. Thirumavalavan, P. Akilan, M. Kandaswamy, Inorg. Chem. Commun. 5 (2002) 422–426.

140 M. Iqbal, I. Ahmad, S. Ali, N. Muhammad, S. Ahmed, M. Sohail, Polyhedron 50 (2013) 524–531.

141 Y.P. Singh, R.N. Patel, Y. Singh, R.J. Butcher, P.K. Vishwakarma, R.B. Bhubon Singh, Polyhedron 122 (2017) 1-15.

142 Y. Singh, R.N. Patel, S.K. Patel, A.K. Patel, N. Patel, R. Singh, R.J. Butcher, J.P. Jasinski, A. Gutierrez, Polyhedron 171 (2019) 155-171.

143 Y.P. Singh, R.N. Patel, Y. Singh, D. Choquesillo-Lazarte, R.J. Butcher, Dalton Trans. 46 (2017) 2803-2820.

144 R.K. Ray, G.B. Kauffman, Inorg. Chim. Acta 173 (1990) 207-214.

145 E.B. Seena, M.R.P. Kurup, Polyhedron 26 (2007) 829-836.

146 M. Joseph, M. Kuriakose, M.R.P. Kurup, E. Suresh, A. Kishore, S.G. Bhat, Polyhedron 25 (2006) 61-70.

147 I.M. Procter, B.J. Hathaway, P. Nicholls, J. Chem. Soc. A (1968) 1678-1684.

148 J.R. Wasson, C. Trapp, J. Phy. Chem. 73 (1969) 3763-3772.

149 B.J. Hathaway, D.E. Billing, Coord. Chem. Rev. 5 (1970) 143-207.

150 R.L. Belford, N.D. Chasteen, H. So, R.E. Tapscott, J. Am. Chem. Soc. 91 (1969) 4675-4680.

151 B.A. Goodwin, J.B. Raynor, Adv. Inorg. Chem. Radiochem. 13 (1970) 135-362.

152 N.D. Chasteen, R.L. Belford, Inorg. Chem. 9 (1970) 169-175.

153 K.K. Narang, V.P. Singh, Trans. Met. Chem. 21 (1996) 507-511.

154 H. Yokoi, A.W. Addison, Inorg. Chem. 16 (1977) 1341-1349.

155 A. H. Maki, B.R. McGarvey, J. Chem. Phys. 29 (1958) 31-34.

156 B. Ni. Figgis, Introduction to ligand-ligand fields, Inter-Science, New York, p. 295 (1966).

157 B.J. Hathaway, in: G. Wilkinson, R.G. Gillard, J.A. MeCleverty (Eds.), Comprehensive Coordination Chemistry, Vol. 5 Pergamon, Oxford, 1987, p. 533.

158 V. Philip, V. Suni, M.R.P. Kurup, M. Nethaji, Polyhedron 24 (2005) 1133-1142.

159 R. P. John, A. Sreekanth, V. Rajakannan, T.A. Ajith, M.R.P. Kurup, Polyhedron 23 (2004) 2549-2559

160 J.A. Weil, J.R. Bolton, Electron Paramagnetic Resonance, 2nd Edition; John Wiley and Sons, Hoboken, NJ, 2007.

161 M. Julve, M. Verdaguer, G. De Munno, J.A. Real, G. Bruno, Inorg. Chem. 32 (1993) 795-802.

162 S. Pal, A.K. Barik, S. Gupta, A. Hazra, S.K. Kar, S.M. Peng, G.H. Lee, R.J. Butcher, M.S.El Fallah, J. Ribas, Inorg. Chem. 44 (2005) 3880-3889**.**

163 M. Padmanabhan, S.M. Kumar, X. Huang, J. Li, Inorg. Chim. Acta. 358 (2005) 3537-3544.

164 E. Garriba, J. Micera, J. Chem. Educ. 83 (2006) 1229-1232.

165 B. J. Hathaway, Struct. Bonding 57 (1984) 55-118.

166 K. Ghosh, P. Kumar, N. Tyagi, U.P. Singh, V. Aggarwal, M.C. Baratto, Eur. J. Med. Chem. 45 (2010) 3770-3779.

167 K. Jitsukawa, M. Harata, H. Arii, H. Sakurai, H. Masuda, Inorg. Chim. Acta 324 (2001) 108-116.

168 E. Kimura, A. Sakonaka, M. Nakamoto, Biochim. Biophys. Acta 678 (1981) 172-179.

169 E. Kimura, A. Yatsunami, A. Watanabe, R. Machida, T. Koike, H. Fujioka, Y. Kuramoto, M. Sumomogi, K. Kunimitsu, A. Yamashita, Biochim. Biophys. Acta 745 (1983) 37-43.

170 E. Kimura, T. Koike, Y. Shimizu, M. Kodama, Inorg. Chem. 25 (1986) 2242-2246.

171 R.F. Pasternock, B. Helliwell, J. Am. Chem. Soc. 101 (1979) 1026-1031.

172 L.M. Ellery, D.E. Cabelli, J.A. Garden, J.S. Valentine, J. Am. Chem. Soc. 118 (1996) 6556-6561.

173 Y. Singh, R.N. Patel, Y.P. Singh, A.K. Patel, N. Patel, R. Singh, R.J. Butcher, J.P. Jasinski, E. Colacio, M.A. Palacios, Dalton Trans. 46 (2017) 11860-11874.

174 Y. Li, Z.Y. Yang, J.C. Wu, Eur. J. Med. Chem. 45 (2010) 5692-5701.

175 R. Xing, H. Yu, S. Liu, W. Zhang, Q. Zhang, Z. Li, P. Li, Biorg. Med. Chem. 13 (2005) 1387-1392.

176 R.S. Nicholson, I. Shain, Anal. Chem. 37 (1965) 178–190.

177 S. W. Feldberg, L. Jeftic, J. Phys. Chem. 76 (1972) 2439–2446.

178 R.N. Patel, N. Singh, K.K Shukla, U.K Chauhan, S. Chakraborty, J.N Gutierrez, A Castiñeiras, J. Inorg. Biochem, 98 (2004) 231-237.

179 J.L. Pierre, P. Chautemps, S. Refaif, C. Beguin, A.El. Marzouki, G. Serratrice, E. Saint-Aman, P. Rey, J. Am. Chem. Soc. 117 (1995) 1965–1973.

180 Z.W. Mao, M.Q. Chen, X.S. Tan, J. Liu, W.X. Tang, Inorg. Chem. 34 (1995) 2889-2893.

181 H. Ohtsu, Y. Shimazaki, A. Odani, O. Yamauchi, W. Mori, S. Itoh, S. Fukuzumi, J. Am. Chem. Soc. 122 (2000) 5733-5741.

182 G. Tabbi, W.L. Driessen, J. Reedijk, R.P. Bonomo, N. Veldman, A.L. Spek, Inorg. Chem. 36 (1997) 1168–1175.

183 S. Durot, C. Policar, F. Cisnetti, F. Lambert, J.P. Renault, G. Pelosi, G. Blain, H. Korri-Youssoufi, J.P. Mahy, Eur. J. Inorg. Chem. (2005) 3513–3523.

184 P. Starha, Z. Travnicek, R. Herchel, I. Popa, P. Suchy, J. Vanco, Inorg. Biochem. 103 (2009) 432-440.

Published Paper from this Chapter

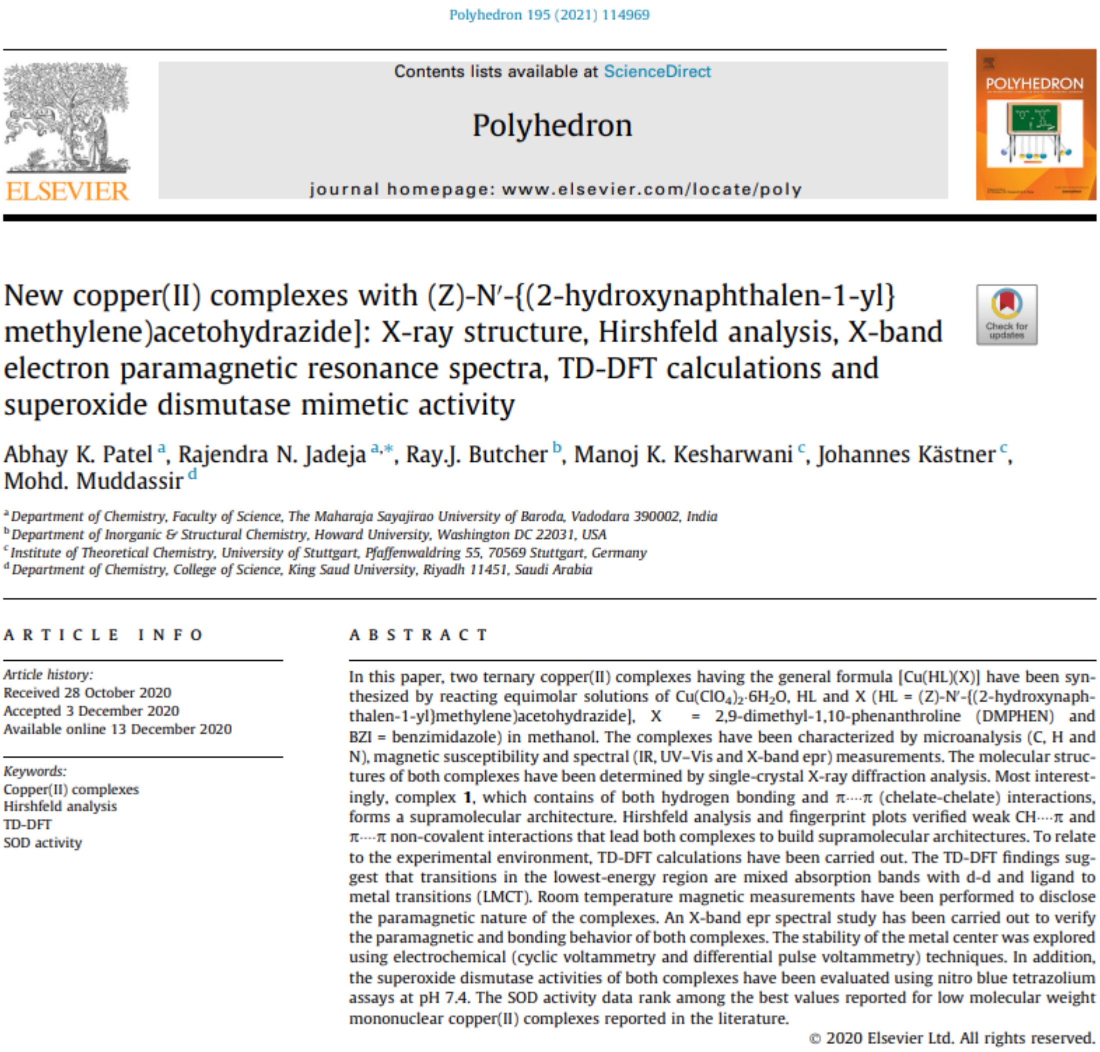

Polyhedron 195 (2021) 114969

Contents lists available at ScienceDirect

Polyhedron

journal homepage: www.elsevier.com/locate/poly

New copper(II) complexes with (Z)-N′-{(2-hydroxynaphthalen-1-yl}methylene)acetohydrazide]: X-ray structure, Hirshfeld analysis, X-band electron paramagnetic resonance spectra, TD-DFT calculations and superoxide dismutase mimetic activity

Abhay K. Patel [a], Rajendra N. Jadeja [a,*], Ray.J. Butcher [b], Manoj K. Kesharwani [c], Johannes Kästner [c], Mohd. Muddassir [d]

[a] *Department of Chemistry, Faculty of Science, The Maharaja Sayajirao University of Baroda, Vadodara 390002, India*
[b] *Department of Inorganic & Structural Chemistry, Howard University, Washington DC 22031, USA*
[c] *Institute of Theoretical Chemistry, University of Stuttgart, Pfaffenwaldring 55, 70569 Stuttgart, Germany*
[d] *Department of Chemistry, College of Science, King Saud University, Riyadh 11451, Saudi Arabia*

ARTICLE INFO

Article history:
Received 28 October 2020
Accepted 3 December 2020
Available online 13 December 2020

Keywords:
Copper(II) complexes
Hirshfeld analysis
TD-DFT
SOD activity

ABSTRACT

In this paper, two ternary copper(II) complexes having the general formula [Cu(HL)(X)] have been synthesized by reacting equimolar solutions of $Cu(ClO_4)_2{\cdot}6H_2O$, HL and X (HL = (Z)-N′-{(2-hydroxynaphthalen-1-yl}methylene)acetohydrazide], X = 2,9-dimethyl-1,10-phenanthroline (DMPHEN) and BZI = benzimidazole) in methanol. The complexes have been characterized by microanalysis (C, H and N), magnetic susceptibility and spectral (IR, UV–Vis and X-band epr) measurements. The molecular structures of both complexes have been determined by single-crystal X-ray diffraction analysis. Most interestingly, complex **1**, which contains of both hydrogen bonding and π····π (chelate-chelate) interactions, forms a supramolecular architecture. Hirshfeld analysis and fingerprint plots verified weak CH····π and π····π non-covalent interactions that lead both complexes to build supramolecular architectures. To relate to the experimental environment, TD-DFT calculations have been carried out. The TD-DFT findings suggest that transitions in the lowest-energy region are mixed absorption bands with d-d and ligand to metal transitions (LMCT). Room temperature magnetic measurements have been performed to disclose the paramagnetic nature of the complexes. An X-band epr spectral study has been carried out to verify the paramagnetic and bonding behavior of both complexes. The stability of the metal center was explored using electrochemical (cyclic voltammetry and differential pulse voltammetry) techniques. In addition, the superoxide dismutase activities of both complexes have been evaluated using nitro blue tetrazolium assays at pH 7.4. The SOD activity data rank among the best values reported for low molecular weight mononuclear copper(II) complexes reported in the literature.